COMPACT MICROSCOPY SYSTEMS WITH NON-CONVENTIONAL OPTICAL TECHNIQUES

Tahseen Kamal

A thesis submitted for the degree of
Doctor of Philosophy of
The Australian National University

March 2018

DECLARATION

This thesis is an original work conducted by me during the period of April 2014 and March 2018 at the Research School of Engineering, Australian National University, Canberra, Australia.

This PhD work has been supervised by Dr. Woei Ming Lee throughout. Certain experimental parts of the works were conducted as group projects with honours students and each of their contribution(s) have been mentioned in detail in the relevant chapters (Chapters 3, 4 and 5) accordingly.

Tahseen Kamal

March 2018

This thesis has been dedicated to my parents and my son, Abyan Eiad.

ACKNOWLEDGMENTS

I am grateful to my primary supervisor, Dr. Woei Ming Lee, for his constant guidance throughout my PhD which was a roller-coaster journey at times. We worked throughout all the difficulties and were able to accomplish quality research. I would also like to thank the members of the Applied Optics group for their support. Without the group's support, it would not be possible to stay persistent. I would also like to mention the role Dr. Chuong Nguyen played as associate supervisor. He was there when I needed the most and was always motivating and encouraging when I felt dejected. My other associate supervisor Dr. Thushara Abhayapala is well-known as a mentor and he has proven himself again when I needed his support during my PhD. I also want to thank the Australian Government for PhD scholarship.

During the course of this journey, I received tremendous support from different levels of ANU. Firstly, and most importantly, I want to acknowledge College of Engineering and Computer Science (CECS) Associate Dean (HDR), Dr. Daniel Macdonald, for the financial support I received to continue research. At the same time, he was a good listener to my concerns, who also provided appropriate suggestions. Dr. Henry Gardener, previous CECS Associate Dean (HDR) supported my travel to San Francisco, USA to attend a congress organized by Optical Society of America (OSA), by offering "Carer Career Development Fund" which at the stage PhD students are not eligible to avail from central ANU.

It is worthwhile mentioning Dr. David Nisbet, Associate Professor, CECS for his continuing support during my PhD journey. I acknowledge his support as an academic, professional contact and a referee.

I also want to thank the Computational Imaging group in UC Berkeley, USA for their support during the computational part of my work. Regina Eckert, Zachary Phillips, provided me support whenever we needed. Especially, Dr. Laura Waller, the PI always responded to emails, which was very helpful during the initial days of the work. I want to thank colleagues from different research groups like solar thermal group, nanomaterials, and biomaterials. It is hard to actually mention some names as most of them travelled alongside me. Because of their encouragement I had a successful PhD seminar at the presence of a large audience. There are more people across ANU in other colleges who have been with me if I needed. The PhD journey would not be possible for me without the support of different parents. I am a single mother. Doing a full-time PhD in Engineering was extremely challenging where I needed two pieces of me to support my lab-work and parenting. The parents of the friends of my son, looked out for me constantly.

I want to thank my parents Dr. A. K. M. Kamal Uddin and Mrs. Rehena Begum for believing in me, for allowing me to grow into an independent strong human being, for nurturing me in an educational environment. Without their upbringing I wouldn’t be who I am today. I would also like to mention my brothers Zunaeed and Mr. Muhammad Nasif for being cooperative.

Last but the most important, I want to mention my son. Abyan Eiad is currently 7 and a half. When I started PhD, he was 3 and a half. In a new country, in a new lifestyle, we adjusted accordingly with lots of struggles during the journey. But I can never thank him enough for being a very strong support, for being a caring child, for being extremely understanding for his age, and for being my son. I could keep my focus on the track because of his presence.

ABSTRACT

This work has been motivated by global efforts to decentralize high performance imaging systems through frugal engineering and expansion of 3D fabrication technologies. Typically, high resolution imaging systems are confined in clinical or laboratory environment due to the limited means of producing optical lenses on the demand.

The use of lenses is an essential mean to achieve high resolution imaging, but conventional optical lenses are made using either polished glass or molded plastics. Both are suited for highly skilled craftsmen or factory level production. In the first part of this work, alternative low-cost lens-making process for generating high quality optical lenses with minimal operator training have been discussed. We evoked the use of liquid droplets to make lenses. This unconventional method relies on interfacial forces to generate curved droplets that if solidified can become convex-shaped lenses. To achieve this, we studied the droplet behaviour (Rayleigh-Plateau phenomenon) before creating a set of 3D printed tools to generate droplets. We measured and characterized the fabrication techniques to ensure reliability in lens fabrication on-demand at high throughput. Compact imaging requires a compact optical system and computing unit. So, in the next part of this work, we engineered a deconstructed microscope system for field-portable imaging.

Still a core limitation of all optical lenses is the physical size of lens aperture – which limits their resolution performance, and optical aberrations – that limit their imaging quality performance. In the next part of this work, we investigated use of computational optics-based optimization approaches to conduct in situ characterization of aberrations that can be digitally removed. The computational approach we have used in this work is known as Fourier Ptychography (FP). It is an emerging computational microscopic

technique that combines the use of synthetic aperture and iterative optimization algorithms, offering increased resolution, at full field-of-view (FOV) and aberration-removal. In using FP techniques, we have shown measurements of optical distortions from different lenses made from droplets only. We also, investigated the limitations of FP in aberration recovery on moldless lenses.

In conclusion, this work presents new opportunities to engineer high resolution imaging system using modern 3D printing approaches. Our successful demonstration of FP techniques on moldless lenses will usher new additional applications in digital pathology or low-cost mobile health.

PUBLICATIONS

Journals

1. **Tahseen Kamal**, Lu Yang, and Woei Ming Lee, “In situ retrieval and correction of aberrations in moldless lenses using Fourier ptychography,” Opt. Express 26, 2708-2719 (2018).

2. **Tahseen Kamal**, *et al.*, “Design and fabrication of a passive droplet dispenser for portable high resolution imaging system”, Scientific Reports 7, Article number: 41482 (2017).

Conference Proceedings:

1. **Tahseen Kamal**, Lu Yang, and Woei Ming Lee, "Application of computational optics in moldless lenses," in Imaging and Applied Optics 2017 (3D, AIO, COSI, IS, MATH, pcAOP), OSA Technical Digest (online) (Optical Society of America, 2017), paper JTu5A.14.

2. **Tahseen Kamal**, Jaden Rubinstein, Rachel Watkins, Zijian Cen, Gary Kong and Woei Ming Lee, “Thimble microscope system” SPIE BioPhotonics Australasia 10013, 1001322-1001322-5 (2016).

3. **Tahseen Kamal**, Rachel Watkins, Zijian Cen and Woei Ming Lee, “Direct fabrication of silicone lenses with 3D printed parts” SPIE BioPhotonics Australasia, 1001336-1001336-6 (2016).

Letter to the editor:

1. **Tahseen Kamal**, Xuefei He, Woei Ming Lee, “Reinventing Pocket Microscopy”, InFocus (Proceedings of the Royal Microscopical Society) 37, 41- 43 (2015).

News Article:

1. Woei Ming Lee, **Tahseen Kamal**, “A droplet approach to lens making”, The Australian Optical Society 28, 30-31 (2014).

TABLE OF CONTENTS

LIST OF FIGURES

LIST OF TABLES

NOMENCLATURE

Name	**Symbol**
Computer Aided Design	*CAD*
Density	ρ
Surface tension	γ
Viscosity	μ
Numerical Aperture	*NA*
Refractive Index	n
Space Bandwidth Product	*SBP*
Signal-to-Noise ratio	*SNR*
Charged Coupled Device (Sensor)	*CCD*
Complementary Metal Oxide Semiconductor (Sensor)	*CMOS*
Polydimethylsiloxane	*PDMS*
Fourier Ptychography	*FP*

CHAPTER 1

COMPACT HIGH RESOLUTION IMAGING SYSTEMS

In this chapter we will discuss the overarching problems and current approaches to achieve high quality scientific instruments at low-resource settings, especially, compact, high resolution, imaging systems. Typical optical microscopes are based on laboratories and possess certain limitations. We will discuss how these problems can be tackled using novel, non-conventional approaches. Our discussions will be restricted to non-ionising imaging systems, *i.e.* optics and Fourier optics approaches. The novel approaches we have proposed in this thesis involve use of moldless droplet lenses, 3D printed architecture to offer decoupled, decentralized imaging systems and use of computational Fourier optics to offer high resolution imaging using the proposed systems.

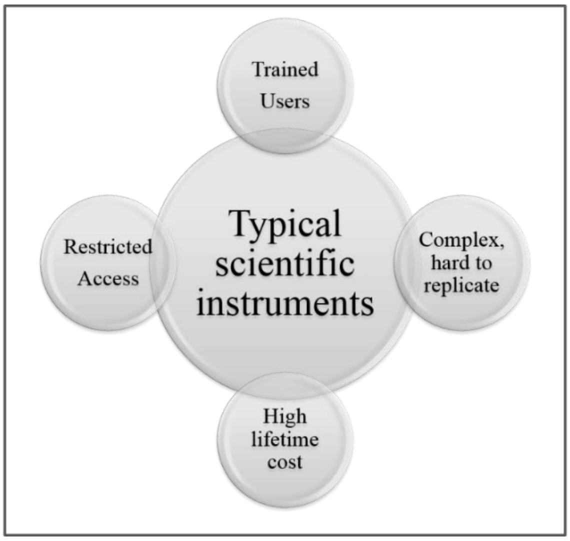

Figure 1:1: Schematic of typical scenario of the use of complex scientific instruments. These instruments are designed and developed in high resource settings, in a laboratory by trained users, which makes them costly, less-accessible and complex.

1.1. Challenges in scientific instrumentation

Customarily high performing scientific instruments are confined in the setting of a laboratory or research environment with trained, paid people having access, limiting their applications in environments with low-resource settings. If we consider health industry as an example, a patient needing healthcare needs to access a facility, such as a hospital or diagnostic centre, waiting for a physician to provide results is the existing picture of accessible care and service. Point of care, point of procedure healthcare is an ongoing research area that tends to offer real-time healthcare where needed, *e.g.* relocating medical imaging from hospital to bedside of the patients [1]. Alternatively, if we consider an optical laboratory providing microscope supports for high quality imaging or a biomedical engineering laboratory where researchers are involved to observe complex biological events, typically require centralized, laboratory-based instruments [2]. It is very common that the building blocks of these complex instruments are available from only a few vendors and the production process is hard to replicate due to the cost and complexity [3]. Moreover, factors like, maintenance [3], transportation of these complex instruments add to the overall lifetime cost. Figure 1.1 articulates the idea of traditional use of complex, high performing scientific instruments.

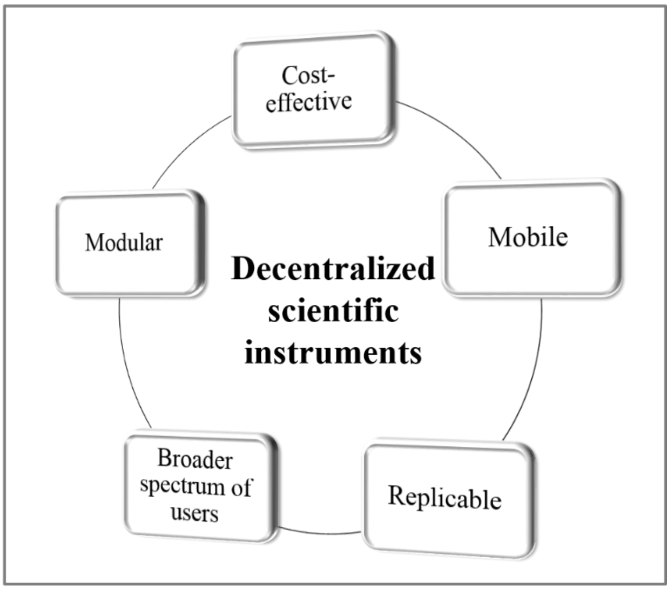

Figure 1:2: Decentralized scientific instrument can be easily transferrable, replicable, and can broaden research scopes at low-cost.

Decentralization of the scientific instruments is an attractive avenue for science to leave the laboratory – especially if high quality results are ensured. That can be achieved,

- by allowing the option to relocate them into different work environments (in laboratory or at a low-resource setting outside laboratory),
- by providing access to broader spectrum of users (specialists to non-specialists) with proper to minimal training,
- with promises to be cost-effective, and
- with provisions for replicability at minimal cost.

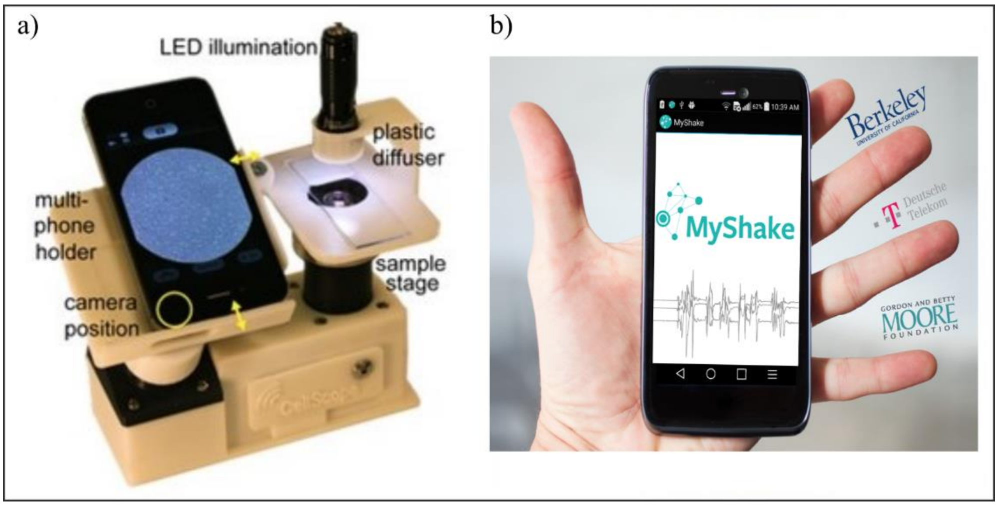

Figure 1:3: Decentralized scientific instruments. a) This portable smartphone-based imaging system has been designed to allow microscopic imaging of biological samples [4]. b) MyShake: a smartphone app available for both Apple and Android phones where earthquakes can be detected by using accelerometers of the smartphones. Till date more than 250,000 people have downloaded this app.

In this work, the motivation is to demonstrate ideas of decentralizing complex, high performing, scientific instruments - with simple components, yet providing high performance, at low-resource settings. There are different research environments, such as health [5, 6], geological research [7], where this decentralization approach would benefit. In Figure 1.2 a schematic of an ideal decentralized scientific instrument has been shown. The primary benefit that a decentralized approach offers is the ability for the design to be shared across the globe, using web or open-source designs like CAD. The use of the high performing scientific instruments by more users, does allow more research and promise scientific advancement.

However, in this work we confine our discussions into high quality imaging systems. As the imaging systems that we are offering have the capabilities to observe smaller samples, in the microscopic resolution, we will discuss about optical microscopes in the following sections. The use of simplistic optics [8], modular housing using 3D printed building blocks [9] and consumer driven electronics such as raspberry pi [10]– has made it possible for decentralization to provide high quality portable imaging systems – at low-cost, for broader spectrum of users. The use of computational reconstruction ensures improved signal – to – noise (SNR) ratio by deploying digital refocusing [11], background noise reduction [12], etc. - at no additional financial cost, but with sacrifice of computational cost.

1.2. Evolution of high resolution optical micro-imaging

Since early 19th century optical imaging through high grade optical lenses have emerged as a rapid resource to capture microscopic activities of different kinds of samples, such as, an animal cell (~10 -20 µm in diameter), that is about a fifth of details (naked eye can see ~0.1 mm without aid) observable by the naked eyes [13]. High resolution imaging has since evolved to image even smaller structures down to 500 nm, *e.g.* mitochondria with the use of different modalities of light microscopes that have been invented [14-19]. Figure 1.4 shows a range of resolutions that are observable using optical microscopes. The exposition of imaging techniques has continuously opened up new areas of research in microbiology. In Figure 1.4(a) we have articulated the range of resolutions that can be achieved using optical microscopes. Figure 1.4(b) shows anatomy of a human eye as an imaging system. A commercial brightfield microscope system has been shown in Figure 1.4(c). The idea of super-resolution has evolved recently where typical resolution limit of optical microscope can be overcome to achieve even ~10 nm resolution [20, 21]. One example of laser-scanning type super-resolution microscope is the Stimulated Transmission Emission Depletion (STED) fluorescence microscope that uses 2 sources of laser to generate a narrow, focused beam by selectively deactivating certain fluorophores that can achieve lower resolution than typical confocal microscopes. Schematic of a typical STED setup has been shown in Figure 1.4(d). There are other types of fluorescence-based super-resolution microscopes that can be found in literature [21].

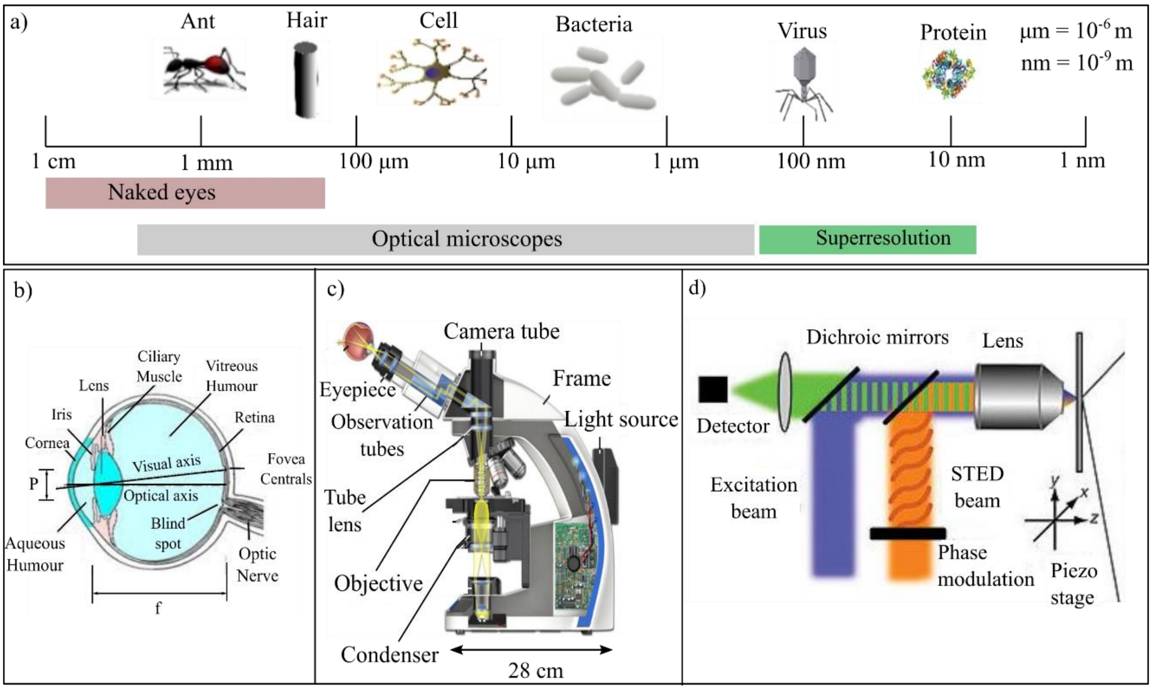

Figure 1:4: Performance of an eye vs optical microscopes to depict the capabilities of optical microscopes. a) Naked eye is capable of observing as small as 0.1 mm and optical microscopes can resolve as small as 500 nm. b) Structure and optics of an eye. c) A commercial microscope to demonstrate the fixed, rigid, complex structure [22]. d) Stimulated Transmission Emission Depletion (STED) Microscope one kind of super-resolution techniques, that uses a 2nd source of laser to restrict fluorescence emission within small area and can achieve up to 20 nm [21]. The optical setup has been redrawn from [20] which is fundamental for super-resolution technique.

However, all optical microscopes (including x-rays) have physical limitations in terms of the maximum imaging resolution achievable. The physical parameters that define the resolution has been discussed by Abbe in 1873 [23], which is defined by, the wavelength (λ) of the radiation, the diameter (d) of the aperture and the focal length (f) of the lens.

For example, for fixed optical lenses, the visible-broadband light sources (390 nm, violet – 680 nm, red) provide, achievable resolution from 200 nm to 400 nm. The physical attributes that limit the performances of optical microscopes have been elaborated in section 1.3. A major limitation in optical imaging is the size of the imaging aperture of the lenses used. Computational optical approaches have been emerged to overcome these limitations [11, 12, 24].

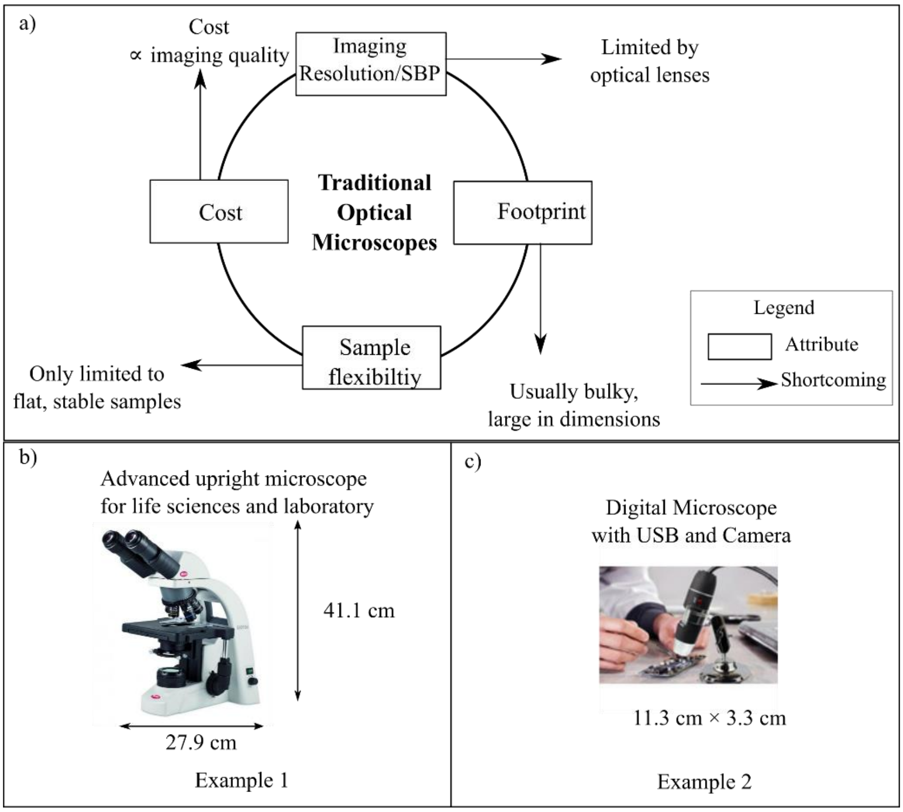

Figure 1:5: Different commercial optical microscopes with their a) attributes and b)-c) the range of options available for microscopic imaging. In b) A commercial microscope that offers both brightfield and phase-contrast imaging [25]. c) A handheld digital microscope which works with a laptop/computer [26].

Optical microscopes possess one of the largest dynamic range when it comes to imaging structures of varying size scales. Using conventional lenses, such as compound one can image Plasmodium falciparum–infected and sickled red blood cells (point of care diagnostics) [27]. With higher power lenses, it has become possible to track sub-cellular features (organelles), and for high energy photons, commonly used in semiconductor industry (wafer). Light is non-invasive in nature that is highly suitable for in-vivo events especially in biological systems. However, the footprint and the overall complexity of the optical microscopes for high power imaging grew exponentially. The upward drive in cost of the microscopes coupled with increasing educational and research institutions, has created a vibrant economic market for optical microscopes, where the global demand is expected to reach over $2.58 billion USD by 2022 [28].

Table 1-1: Attributes of the example microscopic units shown in Figure 1.5.

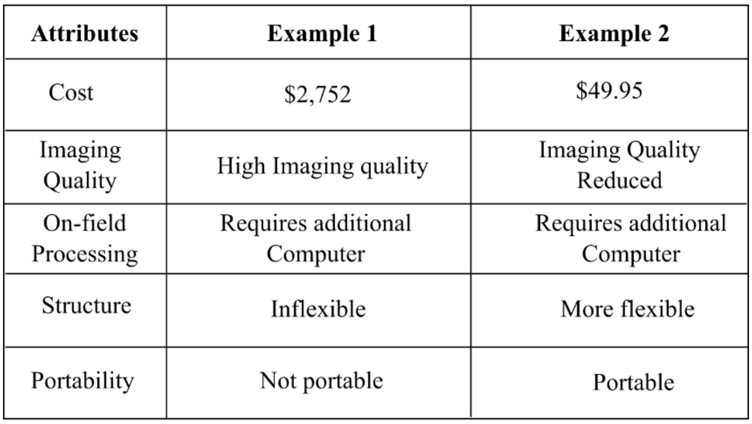

Attributes	**Example 1**	**Example 2**
Cost	$2,752	$49.95
Imaging Quality	High Imaging quality	Imaging Quality Reduced
On-field Processing	Requires additional Computer	Requires additional Computer
Structure	Inflexible	More flexible
Portability	Not portable	Portable

Another feature of the optical microscopes is the types of imaging geometry they cater to. They require flat samples rested on a horizontal plane, stained/labelled or sectioned thin on a microscope glass slide. For ophthalmology patients need to visit a facility where the imaging devices are used by specialized optometrists/ ophthalmologists. Due to many design and accessibility constraints, it is always presumed that the commercial microscopes are better suited for laboratories and trained operators. While the overall cost of a scientific imaging microscope unit remains out of reach for the masses, its inflexible design limits its widespread use.

There is much to learn from consumer imaging devices such as inspection imaging devices. For example, endoscopes [29] and inspection scopes have been robustly tailored to different live-imaging subjects or subjects located in the field, *i.e.*, insects, leaves, fungi etc. Pathological studies of living samples are very crucial for understanding disease progression (*e.g.* studying extra-cellular matrix mechanics has proven to be helpful for diagnosing diseases at early stage [30]). This is especially important for low-resource areas where clinical imaging has been hindered by medical costs of traditional microscopes due to their rigid design structure or portability. Figure 1.5 is a comprehensive summary of the existing optical microscopes, the attributes, and the limitations they possess. Cost usually is proportional to the imaging quality/resolution expected from an optical microscope. The footprint, size of these traditional microscopes is large which restricts these devices in a laboratory environment. Also, the microscopes can usually image samples on a stage, which is along the optical axis of the system.

Consumer electronics motivated by global communications networks has powered new innovative portable computing and imaging platforms [1]. While existing miniature optical components have shown to be compatible with the portable computing and imaging systems to create microscopes, the support network for microscopic imaging for broad research in education, academia and industry is lacking a decentralisation model to meet the global demand. The above discussion is to enlighten the fact that existing optical microscopes with fixed optical alignment are limited, i) by the way they are structured, ii) by the fixed, rigid size of the optical lenses, iii) by the footprint of the microscopes, and iv) for lots of scenarios, by the cost.

In this thesis, we explore new unconventional high-resolution imaging systems by engineering new lens fabrication methods that can be easily decentralized by taking advantage of new computational power from portable computing. Overall, while it is possible to use conventional manufacturing methods to fabricate standalone high performance imaging and computational units [31-33], they do not provide sufficient flexibility for the end users to change the overall design for their own uses. For example, an imaging system that can change from a high-end microscope imaging to dermatology requires different imaging and computational specifications. Here, we attempt to lay the foundation for decentralized models for high resolution imaging. To accomplish these ambitious goals, we would require non-conventional approaches in optical lenses fabrication and computational optics techniques. The different parameters that we have aimed to satisfy through this research are:

i) de-coupled imaging unit from computing unit,
ii) portable and reconfigurable,
iii) Overcoming limits of optical resolution and SBP,
iv) *In-situ* removal of optical aberrations of miniature lenses and
v) Affordable cost and sustainable fabrication approaches.

1.3. Characteristics of optical imaging systems

Optics has been a cornerstone in imaging wide range of samples. It was only until Abbe where the full formalisation of imaging resolution was established. A key notion from Abbe is that all optical systems (including microscopes) are bound by the wavelength and physical aperture of the lenses through the relationship known as numerical aperture (N.A.). Before discussing the limitations of any optical microscopes, it is important to discuss about certain attributes of microscopes.

Numerical aperture (NA): is a dimensionless quantity that describes the amount of light that can be collected by a lens/an optical system. The angle of cone of light entering a lens is the value of NA depending on the medium through which light is travelling, the medium being defined by the refractive index, where $NA = n\sin\theta$, as shown in Figure 1.6. Numerical aperture is then used to define the optical imaging resolution of the system.

Resolution: Lateral resolution, $r_{lateral}$, is defined by smallest distance between two elements that can be separated from the image, $\Delta r_{lateral} = \frac{\lambda}{2NA}$, where λ is the wavelength of the light and NA is the numerical aperture, as defined by Abbe [23]. The axial resolution is given by, $\Delta r_{axial} = \frac{2\lambda}{NA^2}$ which defines the depth of focus achievable from the imaging system. The different resolutions have also been shown in Figure 1.6.

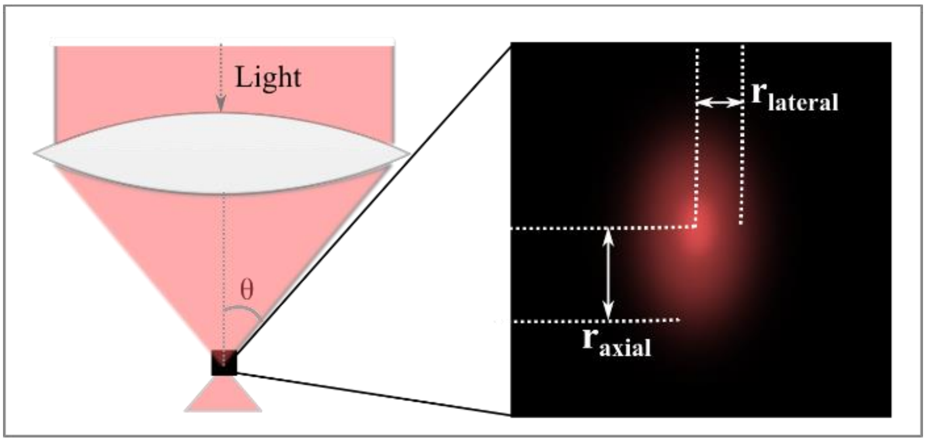

Figure 1:6: Numerical aperture (NA), dimensionless quantity that defines the maximum angle of light accumulation, is given by, $n\sin\theta$. The value of NA in combination with the wavelength of the light used for imaging, define the lateral ($r_{lateral}$) and axial (r_{axial}) resolutions.

Space bandwidth product (SBP): Another imaging parameter that is the amount of sampling points for the entire field of view of a lens. In digital optical imaging, an array of densely packed photodetector arranged in a grid format is used to sample a given imaging field. This can be quantified by the use of space-bandwidth product (SBP**)**, SBP is a scalable, dimensionless quantity that usually expresses the amount of information transmitted by the microscopic system that is the total number of resolvable points over a given FOV (often expressed in terms of number of pixels). And is given by the equation,

$SBP = \frac{FOV}{0.5 r_{lateral}{}^2}$, where $r_{lateral}$ is the lateral resolution.

In other words, SBP is the measure of maximum pixels required over a full FOV with maximum resolution. SBP quantifies the whole optical system in totality, the FOV, magnification and NA. In other words, SBP is the measure of maximum pixels required over a full FOV with maximum achievable resolution. A conceptual model of SBP has been shown in Figure 1.7, where 2 different achievable resolutions have been shown and that SBP is scalable with lateral resolution and/or FOV.

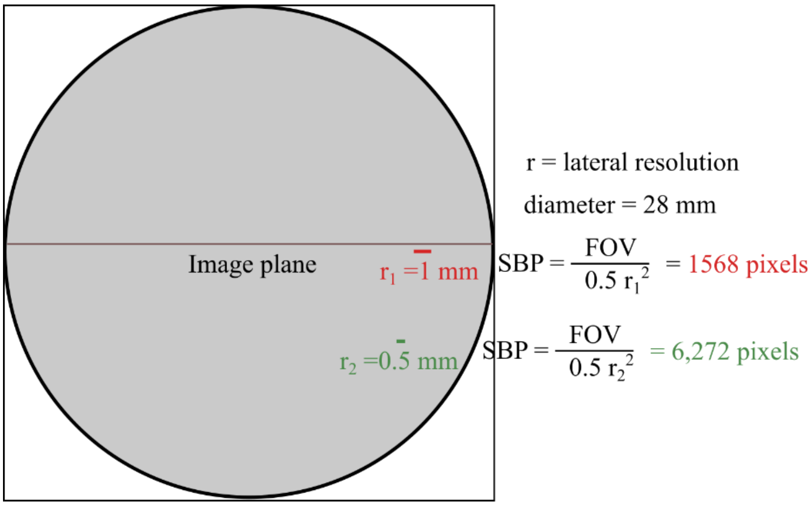

Figure 1:7: Space bandwidth products of an imaging system of FOV 784 mm^2 when different resolutions are achieved. If for the above imaging system, the resolution is a value of 1 mm then the achievable amount of information is 1568 pixels. If the resolution can be improved, keeping the same system to 0.5 mm, the achieved SBP would be 6272 pixels.

All the above parameters are crucial attributes to generate a high quality image from an imaging system especially in optical microscopy system. Another limitation of lenses is that light can be easily distorted due to refractive index inhomogeneity. Ideally a perfect lens would be able to focus all rays on a single spot, but all lenses are polished to a certain degree of accuracy and inherently possess some amount of optical aberrations. This is especially difficult in smaller lenses where the mechanical fabrication steps require even higher precision. To fully achieve the maximum imaging performance of an imaging system, it would require removal of all the distortions that is practically difficult to achieve for the masses [34].

High resolution optical imaging over a full FOV requires specialised lens fabrication steps that are scalable in volume or size. The concept of computational microscopes is an emerging method to overcome many of these physical limitations of existing optical systems [11, 35]. The idea of computational microscopes is rooted in Fourier optics, which allow light to be defined in terms of a complex quantity. It is with the computational optics that optical phase can be numerically retrieved through phase retrieval techniques (inverse problems). Both Fourier optics and phase retrieval will be elaborated in Chapter 5.

1.4. Decentralizing high resolution optical microscopes

Decentralizing complex scientific instruments using consumer driven devices like smart-devices, electronics have found applications in various research fields such as, point-of-care (POC) diagnostics [1, 36, 37], geophysics research [7, 38, 39], education [40] and so on. There have been a surge in compact imaging systems using consumer driven devices along with computational approaches and 3D printed support, for on-filed, high resolution imaging such as, digitizing large paintings in museums [41], on-filed multi-contrast microscope for thin, transparent, biological samples [42] or portable multispectral imaging [43]. The compact imaging systems usually focus on the delivery of high quality images using computational techniques, on-field in a low-resource setting. There are advantages of having a portable, cost-effective imaging system that can deliver good images of interest on-field, without requiring highly skilled trainers to operate them. In order to achieve the quality compact imaging systems, it is important to design the system so that the overall footprint of the setup remains small and portable. The system should contain capabilities to reach smaller resolution, that means, proper selection of optics, illumination and sensor and use of software or programs to be able to use computational processing of the image for better qualities. In the following section we will discuss the options of components that a compact imaging system should contain to deliver desired quality of imaging.

1.5. Components of a compact optical microscope system

The breakdown of the components that are usually required to acquire high quality optical microscopes using consumer electronics has been discussed in the following subsections.

1.5.1. Optics

Traditionally, all microscope systems require optical lenses for imaging. Hence, the choice of lenses is crucial. Optical lenses have evolved and improved over the last few centuries. In current world a lens can be a singlet lens or a compound microscope objective lens with minimum 20 singlet lenses placed deliberately in certain way to provide high quality imaging performance. However, objective lenses with higher NA and higher magnification capabilities are larger and heavier in physical dimensions, and also costlier.

These compound lenses are bulky which makes them unattractive for low-cost, high portable imaging systems. Lenses with larger numerical aperture will allow more light to be collected by the system and thus improve resolution. But that will increase the aberrations. Moreover, for smaller compact imaging systems increasing the physical dimension of the lenses is unintended. Additionally, decentralised manufacturing of lenses using existing approaches for use in low-resource setting does not yet exist. That gave rise to the idea that we have discussed in this thesis.

1.5.2. Instrumentation

To develop optical imaging systems, we need other supporting instruments to acquire high quality images. Depending on the imaging needs the requirement of the instrumentations could vary. The components to acquire compact high-quality microscope images are discussed in the following subsections.

Electronics: Electronics has become integrated part of our daily life. Imaging systems are no exception. For example, for optimization and instrumentation of optical coherence tomography imaging system, different electronics like logarithmic amplifier, field programmable gate arrays (FPGA) or RMS voltmeters could be used [44]. In modern microscopy, the purpose of electronics can be (and are not limited to), i) providing illumination with automatic control [45], ii) mechanical control actuation (*e.g.* sample stage) using a microcontroller [46], iii) in situ processing of the images to achieve information or improved imaging quality using an image processor [47, 48]. A simple and quality example could be the use of smartphone-based imaging systems as they are capable of providing on-spot processing with an imaging sensor available. Alternatively, another example of a processor can be raspberry pi, that is low-cost ($35 USD), that can be used for mechanical control of multiple devices such as, LED, motors, camera and also for *in-situ* image processing [48].

Opto-electronics (imaging sensor): Handheld microscopes developed in as early as 17th century are compound microscopes where the naked eyes are used to observe the sample of interest and recreated with hand drawn pictures. Modern imaging sensors supported by semiconductor technology have given birth to charge-coupled devices (CCDs) that earned a quarter of the Nobel prize in 2009 where a semiconductor photon detector is used to convert incident photons into electrons. Since then, CCD has been an integrated part of imaging systems and in the past few decades have been the building blocks of miniature imaging systems. A CCD sensor is an array of pixels where each pixel is capable of transforming electromagnetic radiation (*e.g.* light) into electronic signals which are then converted to digital signals. The pixel size of CCDs has been reduced by 98% during their lifetime [49]. This allows for images to be transferred into digital information which forms the foundation of image processing and computational manoeuvre of images. CMOS (complementary metal-oxide semiconductor) are another form of sensor that are less expensive to design compared to their counterpart CCDs.

CCDs are being replaced by CMOS because they provide high speed and high functionality but at the cost of noise and sensitivity. A raspberry pi camera is an example of miniaturization where a recorded image with 5 megapixels information in an area of 3.76 mm × 2.74 mm, with pixel resolution of 1.4 µm [8].

1.5.3. Computational approaches for compact microscope system

Modern optical instruments are increasingly becoming digitised through CMOS, spatial light modulator and sensors. This means that many concepts in Fourier optics can now be undertaken with relative ease. Computational imaging is a branch of optics that makes use of the information theory to acquire high dimensional information that has not been originally offered by the system [50] which in turn improves the quality of the resulting/reconstructed image through computational approaches [11]. A compact imaging system that leverages computational approaches will increase the imaging performance drastically. Using computational approaches, the NA and SBP of the imaging systems can be improved [11, 37].

1.6. State of the art of compact imaging systems

There are emerging technologies that focus on developing compact imaging systems to serve biometric security, mobile health [51, 52], or *in-situ* automatic cell identifier [53]. The different approaches for compact high resolution imaging systems can be broadly categorized in two categories, a) lensless and b) lens-based [37].

1.6.1. Lensless

Lensless imaging modality is holographic imaging system that works without the use of optical lenses and provides high quality images computationally [54]. One application of compact lensless imaging is optofluidic microscope (OFM) systems where small aperture-based imaging in combination with microfluidic [55]. Lensless imaging systems record the diffraction pattern emanating from a sample, in the form of scattering or fluorescence onto an imaging sensor and then reconstruct the "image" of the sample with the use of computational algorithms. There are different approaches to acquire on-chip lensless imaging, such as, shadow imaging [53], in which shadow of a biological sample is recorded using coherent illumination source onto a CMOS array. In Figure 1.8 an example lensless imaging system has been articulated from the work of Seo *et al* [56]. This work has demonstrated the use of varying diffraction patterns recorded onto a CCD or CMOS of a liquid containing yeast 10 µm microbeads and red blood cells. Through computational reconstruction and quantification to segregate cells, and identify various properties of the cells [56].

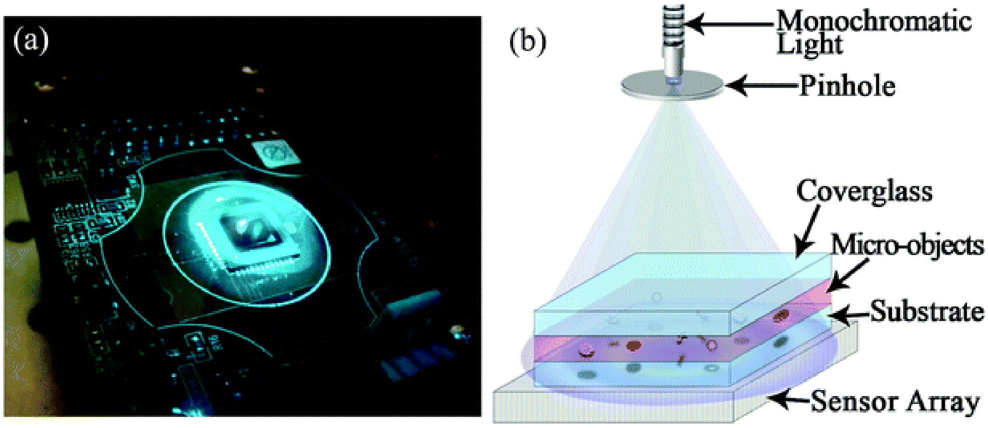

Figure 1:8: Lensless cytometry using lensless digital inline holography that can count and identify cells from a solution of >4 ml and with a FOV of >10 cm^2 [56].

The scattered light off the sample varies over the sample creating a grey profile that is used to observe resemblance using techniques like pattern-matching to identify biological samples. Fluorescent imaging using lensless computational techniques can be used to detect stained/labelled samples of submicron scale that can achieve a large FOV of 2.5 cm × 3.5 cm [57].

A compact Multi-Illumination Single-Holographic-Exposure Lensless Fresnel–MISHELF microscopy (MISHELF) imaging system of footprint 85 mm × 90 mm has been designed that uses single exposure RGB holographic technique for lensless imaging and uses computational techniques to achieve NA up to 0.24 [31].

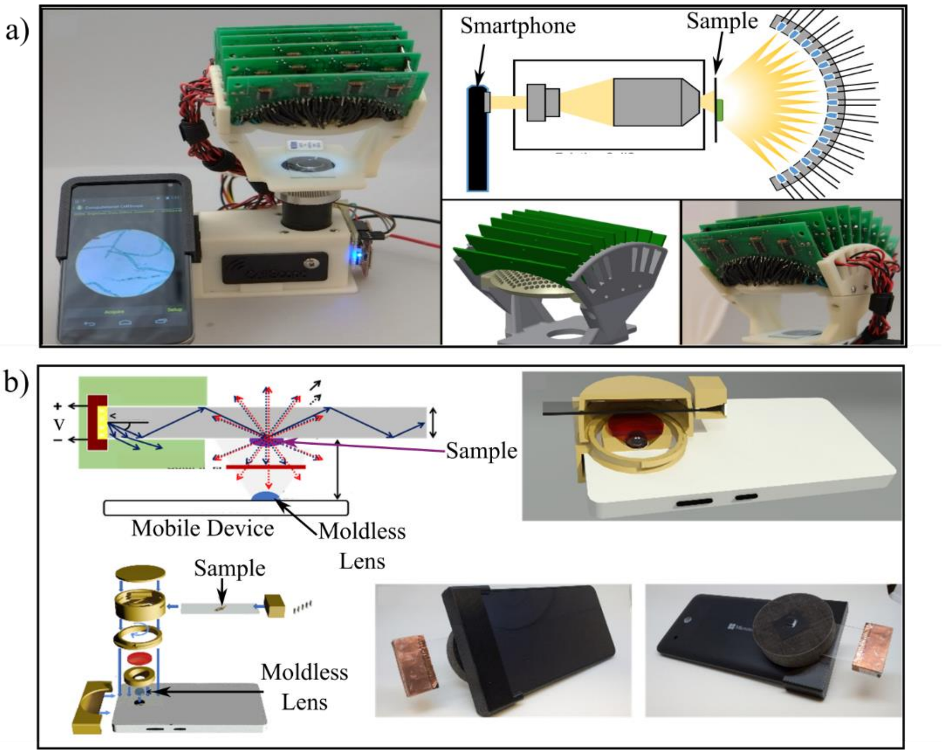

Figure 1:9: State of the art of compact imaging systems using lenses and smartphones. a) Using a cell phone and a hemispherical dome LED array to acquire multiple images of a sample. Also using openCV android based programming which can digitally refocus, acquire phase information [58]. b) A fluorescence microscope using smartphone and inkjet printed moldless lens that can offer autofluorescence, immunofluorescence and fluorescent stains for imaging biological samples in microscopic level [59].

A discussion by Ozcan and Mcleod demonstrates the various techniques used for lensless/lens-free computational improvement of optical microscopic imaging that can overcome the diffraction limit, can computationally achieve wide FOV of 18 cm^2 with a pixel pitch resolution of 2.19 µm, NA of up to 1.4 [54].

1.6.2. Lens-based

Optical microscopes have been used for high quality optical imaging and developed to be a complex instrument for observing various samples. But it has also been used as portable compact imaging system for health applications, digital information acquirement, geophysics and so on. Using microscope in a portable environment is not always an easy task to achieve as the lenses and electronics need to be positioned in an optical alignment that is very sensitive to mechanical movement, or contamination. Quite a few works have been found in literature where efforts have been given to achieve compact, portable high-resolution imaging systems. In [60] a fluorescence microscope have been designed to count somatic cells in milk that can aid in diagnosing mastitis to control milk quality. The features of this portable microscope include on-chip sample staining capabilities and precise cell-counting in a localized chamber at very low cost.

Alternatively, Philips *et al* developed CellScope and a quasi-dome shaped custom LED (imaging system has been shown in Figure 1.9(a)) that can be attached with a smartphone to acquire images of biological samples by illumination engineering [58]. In this work, on-field mobile *app* based on openCV library has been developed to digitally refocus the images to acquire different information from the images on the phone. An application of moldless lenses can be found in [59] where an epi-fluorescence smartphone microscope has been developed. This device offers a compact, (<27 g), low-cost (<$20 USD) fluorescence microscopy on-the-go that uses inkjet-printed moldless lenses (shown in Figure 1.9(b)). Both of these state-of-the-art compact imaging systems leverage the use of 3D printed materials (ABS and PLA respectively) to offer global accessibility of the devices.

Another interesting application of on-chip microscopes are the use of microfluidic chambers to observe that can be of interest for observing compartmentalized chemical reaction or dynamics of biological samples [61]. An automated cell counting compact microscope has been designed using digital holographic setup with the use of a laser diode [62]. The footprint of the system is 75 mm × 95 mm × 200 mm and weight is about 910 g (without a base support), or 1.365 kg (with the base support for stability). Using a cell phone camera or a CMOS sensor and holographic reconstruction approaches this compact microscope is capable of identifying cells using 3D reconstructions.

1.6.3. Lens vs lensless

Lensless imaging is a compact imaging solution approach which does not require use of optical lenses and thus is not NA or SBP limited. However, it is limited by the computational guess (*a prior* knowledge) and the quality of the diffraction signals [54]. Non-standardized computational algorithms also impose a limitation on the mass usage of the lensless modalities. Furthermore, it is less suited for fluorescence imaging as compared with lens-based imaging. This is because the fluorescence emission is not directional, which causing the signal-to-noise ratio deteriorating as a function of the vertical distance and the excitation signal is randomly scattered allowing lower achievable resolution [63].

A majority of the lensless imaging is based on transmission based imaging of thin samples and the performance for dense samples, or reflection mode imaging is limited [63]. Lensless imaging requires only transmission-based imaging whereas compact lens microscopes are capable of observing samples which are placed along the optical path of the design in reflection. Moreover, the lensless imaging systems typically require contact imaging [64] with a very small working distance to work with which can make the infrastructure of the systems rigid, restricting decoupling options.

1.6.4. Proposed integrated approach

In the previous sections, we articulated that there are compact microscope systems designed using different approaches [9, 27, 31, 32, 44, 53, 54, 56, 58, 62, 65]. Through literature review we have also discussed about smartphone-based microscope systems with on-field image processing capabilities that can offer on-field high performing imaging devices. Also, computational imaging techniques, in lensless and lens-based imaging systems broaden the scopes of high resolution imaging. High resolution imaging at low-cost, compact manner has wide range of applications, *e.g.* point-of-care medical devices for screening and diagnostics. In this work, we aim to propose that, a combination of lens-based microscope system with computational approach will expedite the decentralisation of compact microscopy systems.

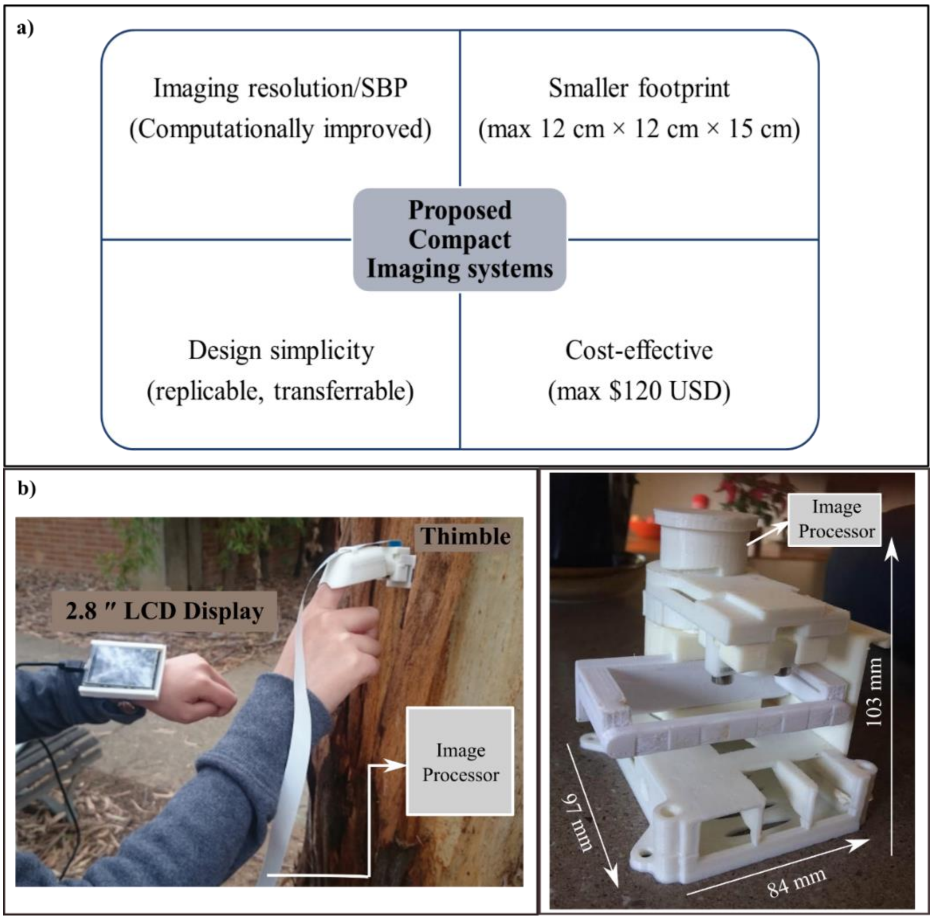

Figure 1:10: Proposed integrated high resolution, high SBP imaging system qualities. Design of the models, credits: Jaden Rubinstein and Michael Petkovic respectively.

This is because computational approaches (both lensless and lens-based) offer high resolution imaging that can be obtained outside of a laboratory environment, overcoming limitations of traditional optical microscopes. In this thesis, we shall explore the avenues where computational reconstruction on simple brightfield single lens microscope can bring about an increase in NA, resolution and improved SBP incorporating phase retrieval approach. The retrieved phase can be used to measure topography or thickness of the sample [50, 66] in label-free manner [67].

In Figure 1.10(a) we have shown a conceptual model of the proposed compact imaging systems that could cost a maximum of $120 USD if display is considered, with a weight of 300 g at maximum. In Figure 1.10(b) and Figure 1.10(c) we have also shown two proposed decentralized, decoupled, high quality, imaging systems that will be elaborated in Chapter 4 (credits to Jaden Rubinstein and Michael Petkovic).

1.7. Thesis organization

In the following chapters we will introduce possibilities of low-cost, portable, high resolution, compact imaging systems, through the development of in-house optics and imaging systems. Throughout this thesis 3 research questions have been aimed to be answered, i) engineering approach to offer low-cost, high quality lenses, ii) engineering approach to develop low-cost, high-quality optical imaging system and iii) imaging performance improvement using computational microscopy techniques. So, the thesis chapters have been organized in a way, where each research question has been introduced through literature review, followed by experiments and results. As such, the chapters 2, 4, and 5 contain literature reviews, whereas chapters 3, 4, 5 and 6 articulates experimentation and results. In Chapter 2 we present concepts of moldless droplet lenses through literature review to elucidate the motivations behind moldless approaches and using droplets for lenses. After that in Chapter 3 we will discuss about the approaches used during this research to develop various moldless droplet lenses. We also demonstrate the performances of the lenses through characterization and imaging. In Chapter 4, we present compact imaging systems developed using the moldless lenses. We also demonstrate the motivation behind the imaging systems we developed. Chapter 5 is about the fundamentals of Fourier optics and the computational approach used in this work. We have discussed the limitations of the proposed system in Chapter 6. In Chapter 6 we have also discussed about the computational improvement of the performance of our proposed imaging systems. Chapter 7 articulates the discussion about the overall research and scopes for future works stemming from the works presented in this research. Chapter 8 is about the conclusion of the thesis.

CHAPTER 2

DROPLETS FOR OPTICS

Light, has the capability to bend, as shown in Figure 2.1(a). Light refracts due to change in refractive index, known as, refraction. If there is a convex interface, incident parallel rays will bend and meet at a certain point, called focal point. Typically, this is the fundamental of converging optical lenses. Now this phenomenon (Mie scattering) can also be observed around us, when we have spherical water droplets in the atmosphere (per cc cloud contains ~100 droplets with each droplet being 1-100 μm in diameter) providing light with convex surfaces to bend, as shown in Figure 2.1(b). In this chapter we will discuss about droplet optics. Scattering of light by particles have been used in developing optical instruments, providing applications in various field of research, *e.g.* meteorology [68]. As water is not a robust optical material to serve as a lens in imaging system, we will discuss about the other liquid alternatives that can be used as droplet lenses. We will look at the physics of droplet formation, under different environmental conditions. This will bring us into the discussion of manufacturing processes as there are various ways optical lenses can be manufactured. We will further discuss about the various applications of droplet optics found in the literature.

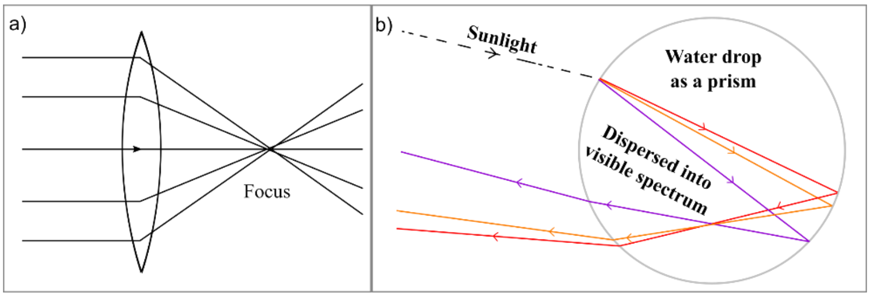

Figure 2:1: Fundamental properties of light. a) Refraction at a curved surface, e.g. a converging lens. b) Sunlight interacting with a water droplet in atmosphere, rainbow phenomenon, due to Mie scattering. Convexity of a surface is required to offer optical magnification. As, droplets naturally allow bending light at its surface, they offer platform for droplet based optics.

There is a demand for multiple droplets in applications; this brings us to another area of research, known as "on-demand droplet generation". Hence, we will also explore the literature to learn about droplets on-demand (DoD). Historically lens-making can be traced back to 17th century. In late 17th century, Antoni van Leeuwenhoek started to grind and polish glasses to achieve quality optical lenses (as shown in Figure 2.2, a lens and a handheld microscope constructed by Antoni). Hence, we will deliberate the motivation behind harvesting droplets to make optical lenses using moldless manufacturing approaches.

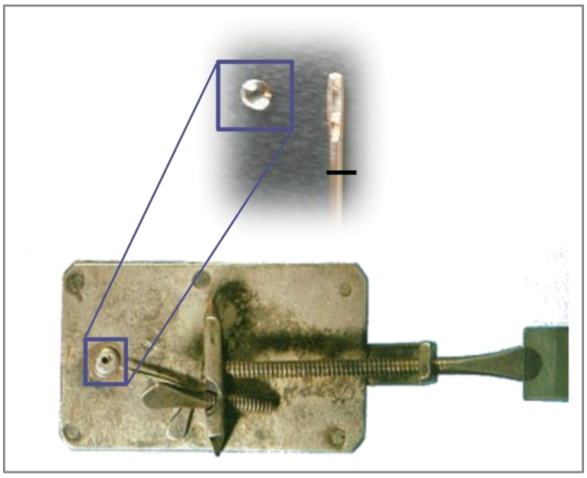

Figure 2:2: History of grinded and polished optical lenses. A polished lens made by Antoni van Leeuwenhoek in late 17th century, and a handheld microscope to attach the lens [69].

2.1. Optical materials for lens making

The choice of material for any optical component depends on the application they are built-for and thus ensuring certain attributes of the components, such as, transparency, transmission, abbe value, resistance, thermal conductivity and so on. Traditionally glass has been the most commonly used material for optical components especially lenses and there are abundant of literature addressing the attributes [70]. Nature has given us with crystals and natural glasses which have been used as magnifiers long before 2000 BC. Eventually, in the late 17th century, popularly known as Father of Microbiology, Antoni van Leeuwenhoek, was the one who formally polished and grinded glass to make them perform as optical lenses and then designed handheld simple microscopes for observing over 500 biological specimens [69]. Later and until now glass lenses are most popular for optical imaging due to the high optical qualities, such as transparency, transmission especially over the visible spectrum (400 – 800 nm) [71]. But in past century, plastic has emerged as an alternative for optical components, especially lenses, as the cost of manufacturing plastic optics are always lower than glasses. In the following subsections we will briefly discuss about the different optical materials used for manufacturing lenses. Recently emergence of metamaterials for has added another dimension to offer ultrathin optical components that can achieve properties not achievable by traditional materials, such as, negative refractive index, cloaking and so on [72].

2.1.1. Glass

The optical properties of a material determine how light will interact with the material. While considering the material to manufacture optical lenses it is important to minimize distortion when light goes through a lens. Historically most commonly used materials for glass lenses are the oxide based glasses (such as, crown glass, which is produced from alkali-lime silicates that contains 10% potassium oxide) as they possess high chemical and mechanical properties [73]. Glass has low fatigue resistance, high scratch resistance compared to plastics. Also, glass exhibits higher thermal stability, which is the change of refractive index with the change of temperature ($\frac{dn}{dT} > 0$, where n is the refractive index, T is temperature), is better than plastics (at least 10 folds better) [74, 75]. Although, it must be noted that, different glass materials exhibit different values of thermal instability. A summary of the discussion around the low tolerances of different glass lenses can be found in Table 1.1 in the book [76]. Furthermore, a list of properties of different kinds of glasses (crown, fused silica, flint) can be found in [77].

While glass is a quality material for optical lenses and still considered to be the best, the lens making process is tedious and exhaustive. A typical microscope objective lens (Figure 2.3(a)) and the manufacturing process has been outlined in Figure 2.3. Among other parameters, surface roughness of optical lenses is crucial for the quality performance of lenses as the roughness is proportional to wide-angle scatter. Wide-angle scatter is a phenomenon that describes image quality in terms of veiling glare present in image, which in turn determines the signal-to-noise ratio or the contrast present in the image [78, 79]. To observe biological specimen or to reach smaller resolution (even $\sim 10^{-10}$ m), it is essential to have less glare and improved contrast. This is achieved in glass lenses through the complicated and exhaustive process shown in Figure 2.3(b). Glass lenses also require anti-reflection (AR) coating to mitigate reflections off the surface, increasing the transmission efficiency for transmissive optics [80].

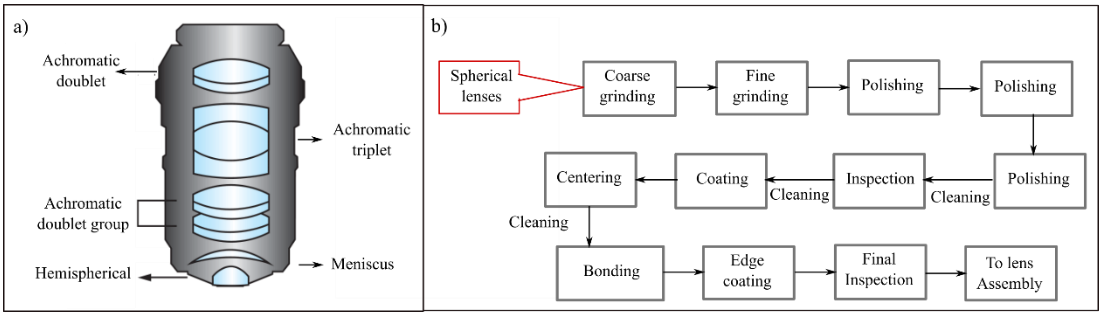

Figure 2:3: A scenario depicting the complex design process of objective lens made from glass. a) A typical microscope objective lens with auto correction capabilities. b) Typical spherical glass lens making process, redrawn with permission [81].

2.1.2. Plastic/polymer

Glass has been proven to be a high-quality material to produce optical lenses because of the degree of freedom (*e.g.* radii of curvature of the surfaces, thickness and distance between elements, dispersive powers). Also, glass offers a range of refractive indices (*e.g.* refractive index of crown glass is ~1.517, whereas lens systems using solid immersion lenses can offer refractive index up to 3.38 for GaP) and high optical transmission quality at the visible spectrum. More information about ranges of refractive indices can be found in [82]. Yet, it is an important research question to find competitive alternatives which have the options to be producible in bulk, in cost-effective manner and offering high quality optical imaging.

Figure 2:4: Sample commercial polymer optics manufactured in industry using injection-molds. Image source: online, used with permission [83].

Polymer has been found to be an alternative, generally known as optical plastics, have found to be used extensively since World War I, has been used to create optical components and prototypes. These polymer optics possess a wide range of advantages over their glass counterparts, such as, i) simple and fast mass production, ii) low-cost, in terms of manufacturability, raw material, repeatability, iii) more durable due to higher impact resistance, iv) optical system design flexibility, often a single polymer lens can be used to develop a prototype, v) lighter, in between 2.5 – 5 times lighter thus making the prototypes lighter and portable [75]. For the sake of clarification, in the literature polymer and plastic optics are used interchangeably and here in this thesis, the mention of polymer optics will include both thermoplastics and thermosetting plastics.

Polymer optics have been emerging as precision optics that can be designed and manufactured using thermoplastics or thermosetting polymers, such as, acrylic, styrene, ultem or zeonex (manufactured by Zeon Chemicals), topas (manufactured by Topas

Advanced Polymers), and silicone polymers [84]. Almost any optics used in the optical systems for any purpose such as, illumination, alignment, imaging, detection, can be manufactured using polymers/elastomers [85]. The thermoplastics group of polymers can be hardened and molten back and forth whereas thermosetting plastics once cured cannot go back to uncured state. An example list of polymer optics that already found market are, barcode scanners, medical disposables, defence optics, CCD camera etc [84]. Figure 2.4 displays some commercially manufactured optical products where the optical thermoplastic materials are, polysterene, polycarbonate, PMMA and topas. It is worth mentioning that AR coating and other coatings are required during the process for manufacturing high quality optical components which adds another complex step to acquire high quality optics.

2.1.3. Transparent Elastomer

As already mentioned previously, liquid droplets naturally retain a non-flat surface, making the droplet usable as a lens or other form of optics, liquid polymers (as they are transparent) then became a contender to be considered as optical lenses because they can be easily shaped into a plano-convex lens by only generating a desired amount of liquid droplet, with the advantage of natural curing to form a soft plastic. Once a plastic lens has been obtained, that lens can be used repeatedly, with smart device, or in a prototype application - unlike water droplets. These groups of polymers are specifically known as elastomers and fall into the category of thermosetting plastics.

Elastomers are a class of amorphous polymers that are both viscous and elastic in nature. The monomers that form the elastomers are found as carbon, hydrogen or silicon. A thermosetting silicon elastomer is cured via an irreversible process called vulcanisation where the polymers crosslink after being exposed to pressure or heat; then the elastomer forms a plastic which is resilient to pressure yet deformable to some extent [86]. The elastomer that has been used extensively for producing optical components is PDMS (one available brand is Sylgard 184 [87]). PDMS has demonstrated high optical qualities and is easily accessible. Liquid droplets extracted from fluid PDMS jet can be cured, via cross-linking to form three-dimensional network of soft plastics without using any mold (or using molds) to form high quality optical lenses [88-91].

Here, we introduce certain attributes of the liquid elastomer PDMS to offer a comprehensive idea about the material. PDMS is an odourless, transparent, organic, viscoelastic liquid having flexibility (shear modulus G varies between 100 kPa – 3 MPa, depending on the amount of crosslinker), low loss tangent ($\tan\delta \ll 0.001$), low melting point ($T_m \approx$ -40 °C) and low glass transient temperature ($T_g \approx$ -125 °C), operational over a wide range of temperature (-100 °C to +100 °C), high gas permeability, high dielectric strength (~14V μm^{-1}) [87, 92].

The chemical formula of PDMS is $CH_3[Si(CH_3)_2O]_{mon}Si(CH_3)_3$ where, "*mon*" is the number of repeating monomer units ($SiO(CH_3)_2$), with molecular weight of 207.4 g/mol. PDMS is available in 2 parts, (i) base and (ii) cross-linker/curing agent. The chemical bond structure of PDMS before curing has been articulated in Figure 2.5(a). PDMS is curable when the base and agent/cross-linker are mixed, which is known as polymerization.

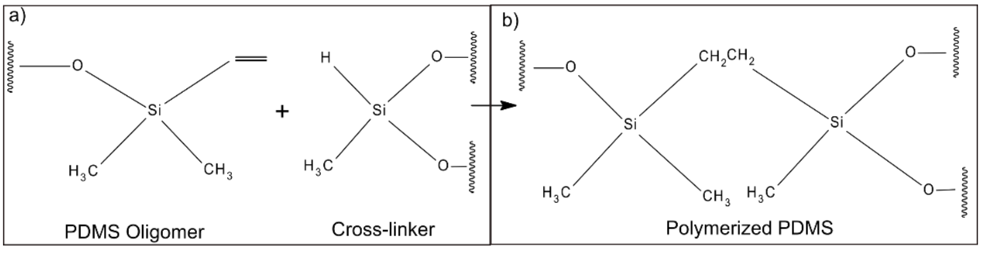

Figure 2:5: Polymerization process of PDMS. a) The monomer of PDMS and the cross-linker/curing agent. b) Bonded PDMS after polymerization.

The amount of curing agent determines the hardness of the cured plastic. A ratio of 10:1 has been standardly used over last decades as a quality ratio for various applications, which means for 10 ml base, 1 ml curing agent is mixed to get desired softness/hardness. For elastomer lenses this ratio successfully produces high quality optical lenses if proper curvature is generated. Once cured, that is after polymerization, PDMS based materials act as soft, deformable plastic, with hydrophobic surface providing a glossy outlook but with quality optical transparency. Post-polymerization PDMS chemical bond structure can be found in Figure 2.5(b). As water or inorganic solvents are unable to deform the PDMS structure after polymerization, the developed prototypes are more robust.

Although for some applications, it is necessary to alter the surface properties of PDMS based prototypes (such as, microfluidic chip), plasma oxidation is often used to make the surface hydrophilic and thus alterable, attachable to applications per requirement [93, 94]. The optical and chemical qualities of PDMS that have been discussed in the literature have been articulated in Table 2-1.

2.2. Study of droplet formation

Formation of dews/water droplets in atmosphere/nature happens through a process called nucleation where humid air condenses into water which has been of interest for many areas of science, like hydrology, physics, optics, medicine, agriculture and etc. [95].

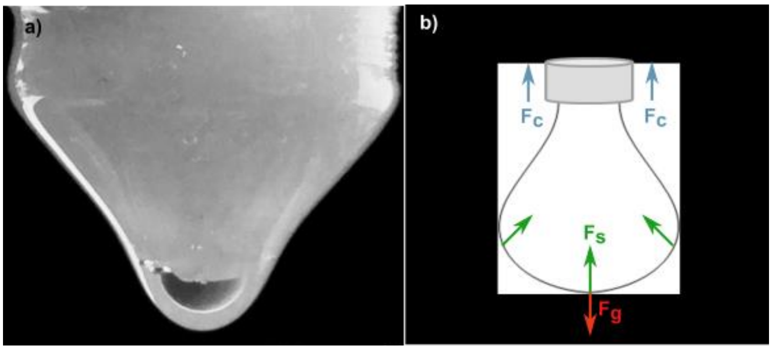

Figure 2:6: Formation of a pendant drop. a) A pendant PDMS drop hanging at the tip of a solid plastic (ABS). b) Different forces acting on the pendant drop to help it retain a convex shape.

On the other hand, if we look at a flowing liquid jet, then droplet formation is a process of disturbance/instability in the flowing fluid [96]. A liquid flowing freely breaks up into small mass of liquids, namely drops, due to the instability discussed by Lord Rayleigh and Plateau, popularly known as Rayleigh-Plateau instability [96]. In this section we will discuss the fluid dynamics for a flowing liquid that is relevant to droplet formation especially where the liquid is a viscoelastic liquid (lens making material of our interest is viscoelastic liquid).

2.2.1. Droplet (pendant and on a surface) and relevant forces

There are different ways droplets can be retained, either on a surface or hanging as a pendant. In Figure 2.6(a) we can see the silhouette of a liquid PDMS droplet hanging at the tip of a solid, commonly referred to as pendant drop, whereas in Figure 2.6(b) a schematic has been shown to explain the forces that act on a pendant drop that is just stable. The force that acts at the interface of a liquid-solid is known as, capillary force, denoted in the figure as, F_c, that is responsible for a liquid attaching to a solid, thus allowing adhesion, and rising in opposition to gravitational force (F_g). On the other hand, surface/interfacial tension dependent force, shown using green arrows, F_s, acts at the liquid-air/gas interface. As a result, the molecules at the surface of the liquid tend to pull themselves closer with an inward cohesive force. This ensures the convex/spherical shape at the liquid-gas interface. The cohesive forces are measured over unit length and thus the unit for surface tension (γ) is Newtons per meter (N/m). Whereas, gravity is responsible for $F_g = mg$, where m = mass of the liquid drop, g = gravitational acceleration.

When dews or water drops form in nature via condensation, they usually form on a solid surface. This brings us to a discussion about wetting, another natural phenomenon that occurs when a liquid-solid contact happens. Figure 2.7 depicts the concept of wetting and spreading that is crucial observation in fluid dynamics in order to design and fabricate fluidic applications, as the height of the droplet changes over the period of time if the spreading is not restricted by some measure. In Figure 2.7(a) the concept of wetting has been portrayed with the use of a liquid droplet that has been dripped on a solid surface (microscope slide) at *t*-th second (with contact angle θ_{before}), and after 5 seconds the droplet image has been taken (Figure 2.7(b)) again where it is observable that the contact angle θ_{after} has been changed, that is reduced after a given amount of time.

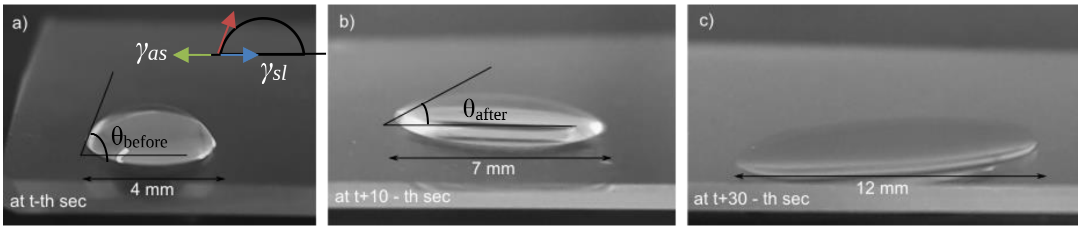

Figure 2:7: Wetting and spreading phenomenon that are important while using a liquid droplet to harvest optical lenses where sufficient. a) Liquid droplet resting on a surface right after deposition. b) After 10 seconds spreading/wetting started to happen. c) Wetting continues as there is no external mechanism to stop the spreading.

Wetting happens until the droplet reaches its equilibrium state (S_{eq}), which is known as thermodynamic equilibrium, takes place when mechanical, thermal and chemical equilibriums are achieved. In reality a droplet equilibrium state is hard to observe within days, so $S_i \neq S_{eq}$, especially if the liquid is non-volatile [97]. As shown in Figure 2.7(c) a droplet at almost thermodynamic equilibrium, when the different forces acting on the different interfaces of the droplet – i) solid-liquid γ_{sl}, ii) liquid-gas (air), γ_{la} and iii) gas-solid, γ_{as} are related as,

$$\gamma_{as} = \gamma_{sl} + \gamma_{la} \cos\theta_{eq} \tag{2-1}$$

Here, air has been considered as the only gas medium, as the manufacturing processes involved throughout this research involved air as the gas medium. In the case of PDMS in mixed state, the wetting occurs until polymerization restricts the spreading, that is until it becomes a soft, hydrophobic soft plastic. But, if we intend to generate lenses with high magnification and resolution capabilities we need to restrict wetting and spreading even at an earlier state, not reaching up to the angle as shown in Figure 2.7(c), as that flat curvature will generate very low magnification lens.

2.2.2. Dimensionless entities for flowing liquid and droplet formation

It is important to discuss some dimensionless numbers that are relevant to the behavior of a flowing liquid and are responsible for droplet generation. These quantities determine the properties of fluids in different scenario and hence are crucial for modelling of microfluidic channels or other applications. Table 2-1 summarizes the relevant values of different parameters and calculated values of the dimensionless quantities for liquid PDMS once it has been mixed with cross-linker.

Reynold's number: Reynold's number is the ratio of two forces to determine the flow regime of a liquid, laminar, or turbulent or transient. Given by,

$$\mathrm{Re} = \frac{\text{Inertial forces}}{\text{Viscous forces}}, \text{ that is, } \mathrm{Re} = \frac{\rho u d}{\mu}, \tag{2-2}$$

Here, ρ – density of liquid, u – velocity of the flow of the liquid, d – characteristics distance and μ - viscosity of the liquid. Reynold's number calculated for PDMS liquid free flowing downwards (under the experimental conditions used for proposed process) is very low <<1 which suggests that the flow is laminar, desirable for optical lens making. It also implies that the viscous forces are dominant.

Weber number: The measure that quantifies the dominance between inertia and surface tension is known as Weber number. The Weber number can be determined by the ratio of kinetic force and surface tension when a spherical droplet is concerned [98]. is given by,

$$\mathrm{We} = \frac{\text{Inertial forces}}{\text{Surface tension force}}, \text{ that is, } \mathrm{We} = \frac{\rho u^2 r}{\gamma}, \tag{2-3}$$

where, ρ – density of fluid, u – fluid velocity, r – radius of jet and γ – surface tension. For PDMS flowing in air, the value of We is very low which implies that droplet formation is dominated by surface tension.

Froude Number: The dimensionless quantity names as Froude number is a ratio of inertia and gravitational force that determines the impact of external forces (gravity) when a liquid is flowing freely. Froude number is calculated using equation (2-4).

$$\mathrm{Fr} = \frac{\text{Inertial forces}}{\text{Gravitational forces}},\ \mathrm{Fr} = \frac{u}{\sqrt{gd}}, \tag{2-4}$$

where u – is the fluid velocity, g - gravitational acceleration and d – characteristic length/distance. If Fr < 1 it means the flow is subcritical and is dominated by gravity.

Bond number (Bo): The relationship that states the ratio between capillary forces vs. the gravity is known as Bond number (also known as Eötvös number) and is given by,

$$\mathrm{Bo} = \frac{\text{Inertial forces}}{\text{Viscous forces}},\ \mathrm{Bo} = \frac{\Delta\rho g d^2}{\gamma}, \tag{2-5}$$

Here, $\Delta\rho$ – difference between density, g – gravitational acceleration, d – characteristic length and γ – surface tension. A value of Bo >> 1 indicates that the gravitational forces dominate the inertial forces.

Ohnesorge Number: Another dimensionless quantity that relates the viscous forces to the inertial forces and surface tension of a liquid jet is the Ohnesorge number. A value of high Ohnesorge number indicates that viscosity of liquid is dominant and that is crucial for determining if a liquid is jettable. PDMS has a high value (~4) which is expected due to the high viscosity of PDMS. Ohnesorge number is given by,

$$\mathrm{Oh} = \frac{\text{Viscous forces}}{\sqrt{\text{Inertia}\times\text{surface tension}}},\ \text{so, } \mathrm{Oh} = \frac{\mu}{\sqrt{\rho\gamma d}}, \tag{2-6}$$

where, μ - viscosity of the liquid, ρ – density of fluid, d – characteristic length and γ – surface tension. Also, Ohnesorge number is related to Weber number and Reynold’s number by,

$$\text{Oh} = \frac{\sqrt{We}}{\text{Re}} \tag{2-7}$$

Capillary number (Ca): As the name suggests capillary number is concerned with the measure of capillary force relevant to a liquid when there is a liquid-air/gas interface or liquid-liquid contact. The capillary number is calculated by the ratio of viscous forces and surface tension, given by,

$$\text{Ca} = \frac{\text{Viscous forces} \times \text{Velocity}}{\text{Surface tension}}, \text{ so, Ca} = \frac{\mu u}{\gamma}, \tag{2-8}$$

Table 2-1: Dimensionless quantities for mixed PDMS liquid flowing in air.

Dimensionless quantity	**Value**
Reynold’s number	0.0008
Weber number	0.0001
Froude number	0.0058
Bond number	4.07
Ohnesorge number	14.23
Capillary number	0.17

Usually the value of capillary number indicates the impact of viscous forces in the flow of the liquid in discussion. A value of For PDMS flowing through air the value is ~0.2 and that indicates that viscous forces are dominant and capillary forces are negligible. Critical capillary number $\text{Ca}_{\text{cr}} \approx 10^{-2}$ is a measure to realize droplet formation process and if Ca > Ca_{cr} then shear is responsible for droplet formation [99]. The following table has been generated considering a mixed liquid PDMS with velocity of 1 mm/sec, characteristic length/distance of 3 mm, density of 965 kg/m^3, viscosity of 5.1 pa-sec and surface tension of 0.0209 N/m.

2.2.3. Droplet formation from a falling jet

Joseph Plateau observed in 1873 that when the length/diameter ratio of the jet exceeds a factor of 3.13-3.18 the droplet formation happens. This process can be seen in Figure 2.8. Its observable that the droplet formation happens when a sinusoidal pattern is formed, and the radius of the jet starts reducing to a point where the mass at the tip detaches itself to form a droplet. Interestingly, this was observed by Leonardo da Vinci who incorrectly concluded that the detachment of the droplet is due to gravity as he wrote, "*How water has tenacity in itself and cohesion between its particles. This is seen in the process of a drop becoming detached from the remainder, this remainder being stretched out as far as it can through the weight of the drop which is extending it; and after the drop has been severed from this mass the mass returns upwards with a movement contrary to the nature of heavy things*." [100, 101]. Later, throughout 19th century it has been established that the detachment of the droplet itself could be attributed to fluid motion and surface tension.

Droplet formation is a process initialized by instability in a flowing liquid. The instability depends on the radius, length and velocity of the liquid jet. When a liquid jet is flowing only with gravitational force acting on the flow it maintains a constant radius until it reaches a maximum length. After that the cylindrical shape of the jet thins and the droplets start to form. The factors responsible for this are surface tension, intermolecular forces, velocity, radius, length of the jet.

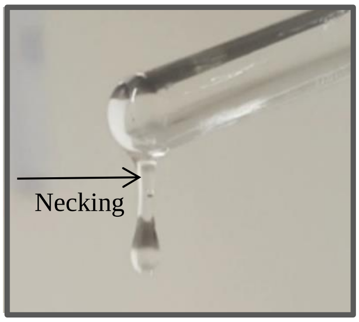

Figure 2:8: A falling liquid jet forming a droplet and a neck is forming. Image has been acquired in the lab using mixed PDMS.

Droplet formation from a flowing liquid jet usually has different regimes (further discussed in section 2.6.2).

2.3. Applications of droplets in optics

Silicone elastomers have found lots of applications in the field of optics especially because they are readily transparent with high optical transmission [85]. They are highly efficient contender for fabricating optical components, such as, lenses, gratings, mirrors, resonators, lasers and waveguides [8, 102-106]. In this section we will only highlight the applications where liquid droplets have been used to develop optical applications.

2.3.1. Lasers

Droplets, having smooth convex surfaces, are capable of performing as optical resonators (providing microcavities) that can find its root way back in 1977 when Ashkin and Dziedzic observed resonance in a dielectric sphere with changing surface waves [107]. In 1984 laser emission using ethanol droplets (60 µm diameter) has been reported first time, where a 514.5 nm laser has been used with Rhodamine 6G dye [108]. After that a wide range of works have been done to create lasing/micro-lasing using droplets as cavities such as, Saito *et al* showed in [109] the use of organic dyes to create droplet in a solidifying elastomer to create tunable lasing. The dye injected into the semi-solid elastomer mold forms a spherical shape naturally due to surface tension. Once the sphere has been formed the shape could be altered to ellipsoid by putting pressure on the solidified elastomer mold.

2.3.2. Sensors

Droplet micro-resonators can be used as sensors by detecting change in refractive index at the surface of the sphere. The use of droplet resonators has been found to create resonances in whispering gallery mode (WGM) that has been used for protein/chemical detection due to the advantage of confining the experimentation in a small microdroplet [110, 111].

2.3.3. Tunable lenses

Another important application of polymer in optics is to design lenses with tunable focus which is possible due to the compressibility in the plastic [112, 113]. Typically, these lenses are manufactured using an optical fluid, run inside a thin polymer membrane, where the adjustable focus can be achieved by using mechanical forces to alter the membrane shape for example, simply by using a metal ring and moving the ring along the membrane. The change in the membrane shape allows the fluid to take varying shape (from flat to convex to aspheric) along with allowing the focal length to vary. Interestingly, lenses made of elastomer, such as, PDMS can be tuned using less efforts, with the use of controlled strain that can deform soft PDMS lenses hence allowing the focus to vary; which also can be used to vary aberrations [114, 115].

2.4. Manufacturing of optical components

Typically, in the industry high volume, precision optics (diffraction gratings, lenses prisms, etc.) are manufactured using various techniques. The manufacturing processes can be broadly segregated in 2 categories, i) Mold-based (using a mold, cavity to form the desired shape of optics) and ii) Moldless. In the following subsections we will discuss these manufacturing processes in terms of their pros and cons. We will limit our discussions to polymer/plastic optics and liquid elastomer optics primarily.

2.4.1. Mold-based

Industrial mold-based manufacturing processes for variety of optical components can be further segregated into 3 classes, i) Injection molding, ii) Compression molding and iii) Hybrid injection-compression molding (also referred as coining).

Injection molding: The injection molding processes have been used to obtain surfaces such as, spherical, convex, cylindrical, aspheric biconvex, meniscus, which have been practised over decades [93, 116, 117].

While, injection molding is highly sought after for high quality precision optical components with high throughput, the initial setup cost is high as the cost of mold preparation is high which is typically in the order of millions for the factory and mold setup. Figure 2.9 shows a pie-chart where an estimation of cost for injection molding approach has been shown. It is observable that 78% of the cost resides in the molding part whereas the rest is for coating and tooling [118].

Precision injection molding: Polymer optics industry observed that the conventional molding approach for polymer industry was not sufficient for manufacturing optical components due to high precision requirements in terms of mechanical engineering, tooling and process engineering. Modification of the process gave rise to “Precision Injection Molding (PIM)” approach which till date is very popular for fast, massive production of polymer optics, such as spherical, aspheric, freeform and diffractive optical lenses, typically of 1 mm – 100 mm diameter, 1 mm – 30 mm thickness yielding a diameter-to-thickness ratio of 1:1 to 5:1.

The requirements for successfully acquiring polymer lenses using PIM approach include, i) expert knowledge, ii) design experience, iii) tool shop capabilities, iv) injection molding machinery and v) injection molding process. Injection molding processes perform by injecting a hot melted liquid polymer into a cold polymer mold. Typically, the mold used in injection molding approach are component specific, thus each mold having the capability of producing one specific optical component.

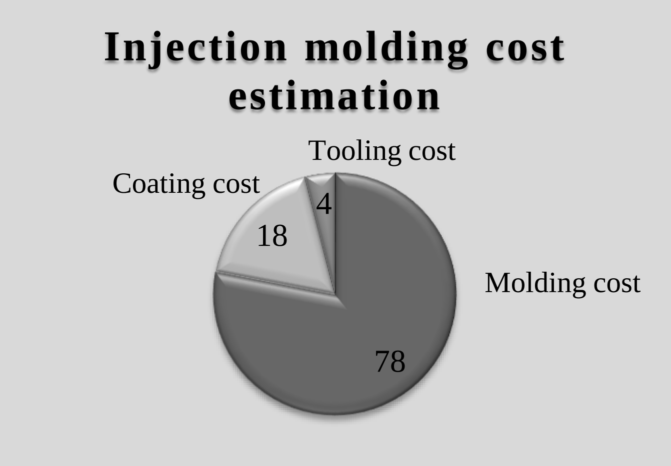

Figure 2:9: Pie-chart showing example of injection molding plastic optics manufacturing cost [118]. It is observable that most of the cost resides in the molding part of the process.

However, the fact that non-uniform mold contour shrinkage takes place (0.5% – 0.6%) during the mold manufacturing process, this leads to contour error during lens making, that is undesirable for optical lenses. Alongside, the surface roughness of the mold contour itself is crucial to generate high quality optical lenses. The performance of injection molding approach to manufacture optical lenses has another disadvantage that there is stress induced distortion, the stress originating from the injection of viscous, hot, liquid/melted polymer, resulting into birefringence [119].

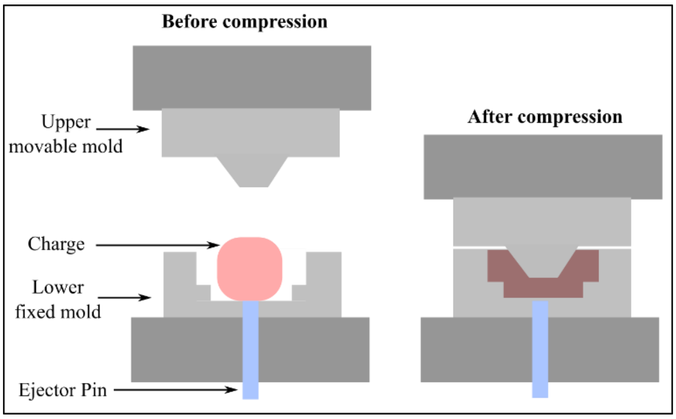

Figure 2:10: Compression molding process. The process typically uses two halves of a mold and a piece of solid substrate. The solid substrate is brought to molten stage using high temperature and then placed into the bottom mold. The top mold is then compressed to acquire the desired molded component.

Compression molding: Compression molding has been used to manufacture mostly freeform polymer optics, and also, to manufacture Fresnel lenses [120] or microlens array

[121]. The process of compression molding involves, using two mold-halves and a sheet of solid substrate. Using high temperature, the solid substrate is brought to a molten state, and then two mold shapes are used to compress onto the substrate, thus hot-embossing the mold onto the molten substrate. The cooling of the molten substrate is required to acquire desired product. Figure 2.10 shows compression molding process.

The embossed substrate with the mold embedded has been used for low-cost, rapid manufacturing of lens arrays [122]. As the process of compression molding involves very minimal liquid flow, there is no stress induced distortions present in the manufactured optics. However, speed of embossing, amount of pressure, movement of the mold during compression, these are some of the key factors for determining optical performance of the developed produces. The process of compression molding is lengthier compared to injection molding, because of the temperature cycle, thus is not popular for high volume prototyping applications.

Hybrid Injection/compression molding: A trade-off between two (injection and compression molding) approaches have been developed, known as “coining”, which is a hybrid injection-compression molding (ICM) approach, commonly used for manufacturing CD, DVDs, optical lenses using microinjection [123]. A liquid jet is injected into a chamber of a mold with two parts, and the two parts are then compressed to shape the product into desired shape. The initial setup cost for ICM is not as high as injection molding, whereas the precision and high throughput is also not as efficient.

In the literature, the other mold-based approaches for making high precision quality polymer optical elements are vacuum injection molding (VIM), extrusion molding, UV curing, diamond turning [124].

2.4.2. Moldless

The use of mold is highly effective for rapid prototyping of precision optics. For many applications achieving high precision is a desired requirement. The abovementioned approaches offer high throughput, high precision products but are complex, time-consuming, requires expertise and are costly. The complexity in the involved machinery, high initial setup cost, overall process duration, make them less attractive for mass manufacturing for R&D purposes, where the initial setup cost mitigation is important for allowing access to more students and academics. Low-cost, high quality optical lenses have also found use in building consumer products such as disposable medical, wearable devices and lab-on-a-chip products. The cost and complexity of the mold-based approaches led to innovation of moldless approaches. This brings the highlight on 3D printing objects that revolutionized manufacturing world with the endless possibilities of printing any object [9, 125], possibilities of de-clustering when necessary, printing even human organs with the advent of bioprinting [126], even printing bacteria [127]. 3D printing is a moldless manufacturing approach that is cost-effective and more accessible for researchers and enthusiasts which does not need high initial setup cost (commercial 3D printers, as shown in Figure 2.11(a) can be purchased for household use even at a cost of $199 USD, for a build volume of 140 mm× 140 mm×140 mm), or highly skilled expertise to learn CAD design, making them a choice of moldless manufacturing where time and mass production is not of primary concern. However, 3D printing has still a long way to go to be considered for mass manufacturing as the printing can take even up to days depending upon the size or amount of printing [128]. A comparison between injection molding and 3D printing has been shown in Figure 2.11(b).

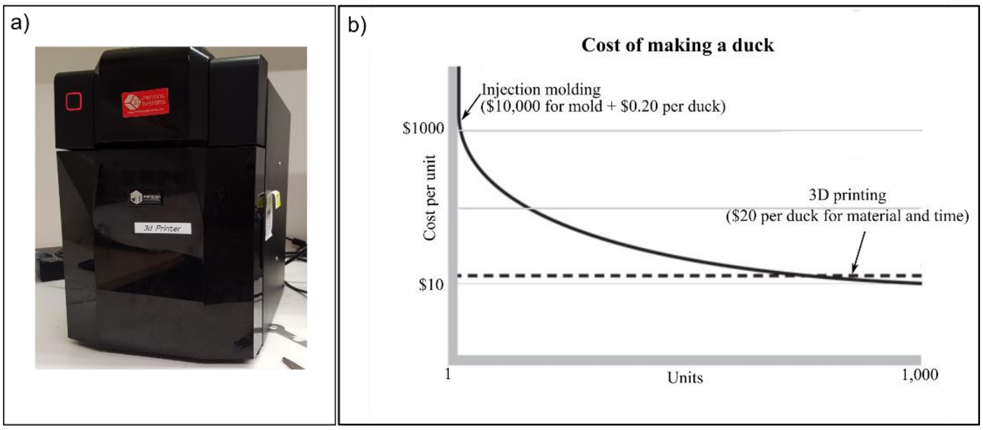

Figure 2:11: Alternative manufacturing using 3D printing. a) A commercial 3D printer, up mini printer that can print a volume of 120 mm x 120 mmx 120 mm. b) A comparison showing how injection molded manufacturing and 3D printed are effective in different circumstances [128].

3D printed optical components are possible [129, 130] but can be costly due to the requirement bound by, choice of material, precision and accuracy. Moreover, mass manufacturability is still far-fetched for 3D printed products.

From the above discussion based on various advents in the manufacturing process and their pros and cons, it can be observed that there are multiple factors that can lead to a choice of manufacturing process for a product; there are always trade-off factors to be considered. For the proposed manufacturing process using moldless approach, the initial aim was to develop a process with, i) the capability of mass manufacturability, ii) cost-effectiveness, iii) repeatability without adding overhead cost, iv) ease of access to the process, v) and of course, high quality end-products.

As already discussed, liquid droplets can be used as optical lenses, and droplet generation can be possible from a flowing jet. Thus, another moldless approach for optical lenses could be the simple use of droplets acquired from liquid with high optical qualities (such as PDMS). Liquid PDMS can easily be formed into a shape of a droplet, due to the variable forces acting on the droplet; it will essentially retain the curved surface leading to a droplet. Once polymerized/cured, the lens is a soft plastic and transparent, easily attachable to a smart device or in a 3D printed prototype to be able to image. The surface roughness is low due to cross-linking of the polymers at the surface, making them quality optical lenses.

The interest in droplet generation to manufacture liquid droplet lenses led to the discussion of different droplet generation approaches, which can be found in following sections

2.5. On-demand droplet generation

Droplet generation can be ubiquitous – as found in nature, or precise, controlled, either continuous – generating a continuous stream of liquid droplets, or on-demand. The important consideration in this area of research is to generate controlled monodisperse droplets of desired size and shape (diameter, volume, shape specific). Drop-on demand (DoD) is popular for applications where droplet generation on demand is necessary, for example one application of inkjet printing technology where the printer generates droplets when necessary and the droplets can be ejected differently (using electrostatic force or piezoelectric crystals or heat to thermally activate droplets) [131].

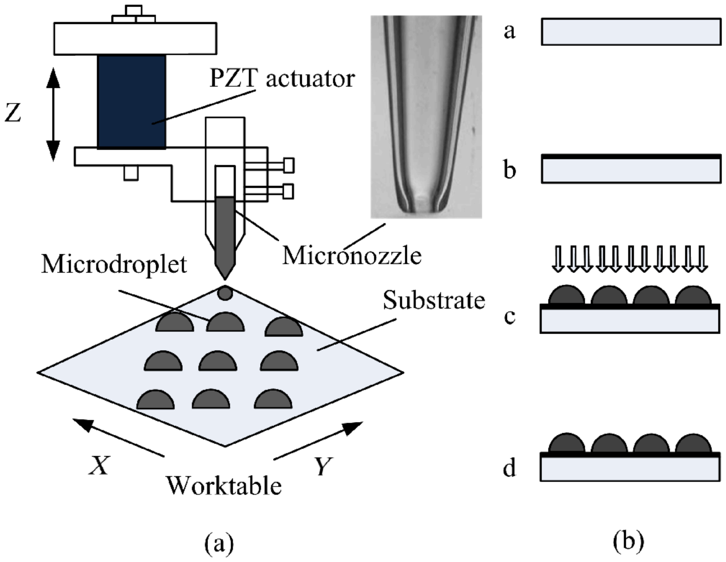

Figure 2:12: On-demand droplet generator where the mold substrate has been fabricated using PDMS and the Norland 65 optical adhesive has been used for the lens material that is a photopolymer [132].

Unlike continuous inkjet technology where the fluid jet has to be conductive, hence limiting biological applications, DoD can be applicable for biological systems, making these approaches eligible for dispensing biological cells [133, 134]. Other popular applications of DoD inkjet printing are, biopolymer arrays, microlens array, printing of organic transistors, polymer light emitting diodes [135-138]. Figure 2.12 shows a DoD used for manufacturing polymer microlens array.

On the other hand, microfluidic droplet study in a microfluidic environment has been very popular as discussed by Huebner *et al* in "Microdroplets : A sea of applications?" [139]. Microfluidic devices, containing channels of micron size, allow the miniaturization of applications (*e.g.* lab-on-a-chip systems) to observe fluidic behavior in small volume, along with the possibilities of simulating a macro environment in small scale with improved analytical performance at low-cost and on-demand droplet generation of nanoscale. These features enabled microfluidic devices to find applications to mimic chemical and biological systems, especially creating an environment to observe isolated microdroplets to suppress dispersion of reactants into a shape – allowing compartmentalization, at high throughput [140]. Also, it has been found that flow of more than one liquid stream in a microchannel, where one liquid is immiscible to the other (oil in water, for example, where oil flow is known as dispersion, and water flow is known as continuous, with the possibilities of other variations) allows formation of emulsion droplets with the presence of shear stress or force [141].

For the ease of introducing some droplet generation approaches, it is worth mentioning that common droplet generation geometries in microfluidics are cross-flowing streams, commonly known as, "T – junction" (Figure 2.13(a)), elongational flow known as "flow focusing" (Figure 2.13(b)) where multiple fluid is flown through a small channel [142]. Other possibilities being, co-flow, 3D flow-focusing etc [143].

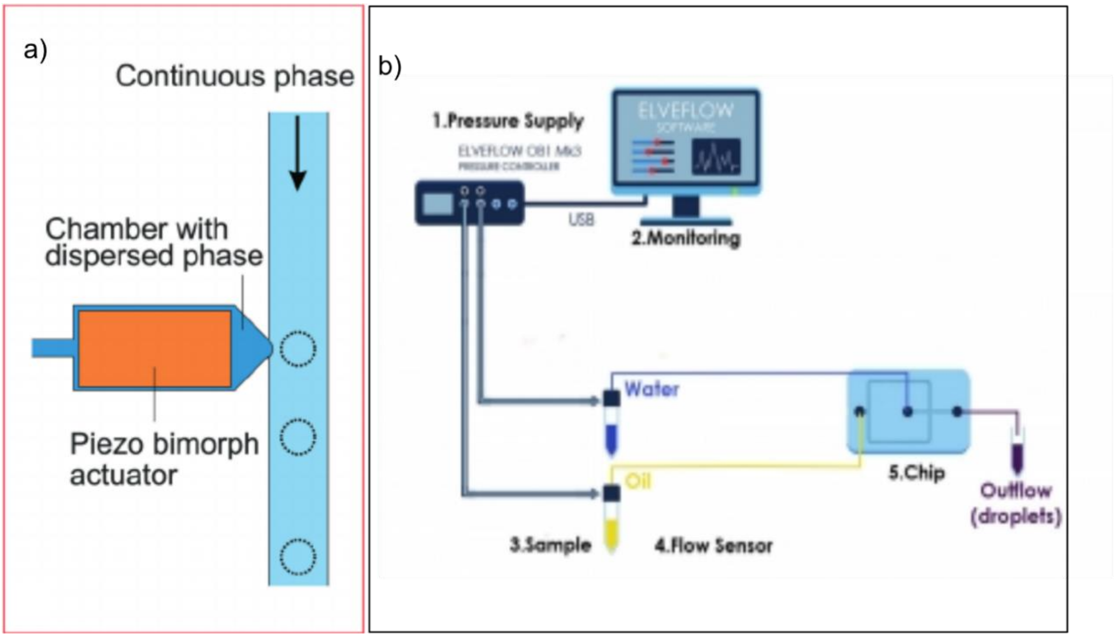

Figure 2:13: Different microfluidic geometry used for droplet generation. These two approaches are the most popular approaches. a) A T junction where a piezo-actuator has been used to inject the dispersed fluid [142]. b) A flow-focusing device where two fluids have been used to create droplets [143].

Now, as we have discussed the applications of "droplets on-demand", it is important to note that there are various kinds of on-demand droplet generators, mostly being "active". The other obvious option is, "passive" droplet generator. The impact, application, and comparison between active vs passive microfluidic droplet generators can be found in [144] while Figure 2.14 summarizes the steps of typical active vs passive environments.

2.5.1. Active droplet generation

As the name suggests, in active droplet generator the formation/generation of droplets is initiated by some active force or pressure – mechanical disturbance, like the inkjet printer technology discussed in previous section. [145, 146]. This can be as simple as ejecting a drop of liquid through pressing the plunger of a syringe. There are various active droplet generation used for on demand droplet generation. Use of piezoelectricity is one popular way of effective, precise droplet generation, such as, piezo bimorph actuator for dispensing or piezoelectric disc for creating mechanical vibration etc. The use of pneumatic valve also has been found to create micro to nano-scale droplets on-demand with highly controlled [147]. Controlling pneumatic micropumps by programming (using LabView) was found to be efficient in droplet generation where the continuous flow of liquid was injected using a syringe pump and a dry vacuum pump was used to control the valves [148]. This work was claimed to produce microdroplets at a higher rate by using three-way actuation of the pumps with the option to control over the selection of pumping frequency that in turn can control the droplet generation frequency along with a control over droplet size.

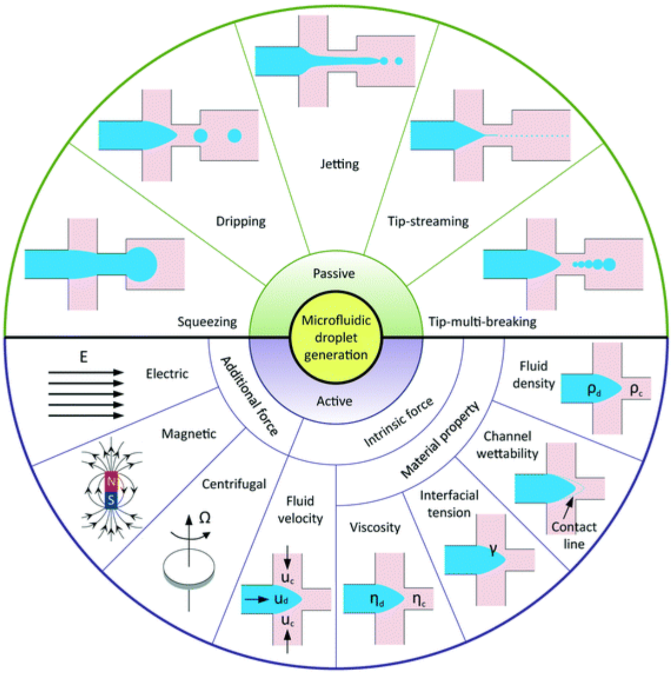

Figure 2:14: Droplet generation in microfluidic devices. The droplets achievable can range from picoliter to ml (milliliter) [144].

2.5.2. Passive droplet generation

Passive droplet formation, on the contrary to active droplet generation, does not involve use of external control mechanisms like pressure, heat or force. Droplet formation from a flowing liquid jet is the most fundamental form of passive droplet formation. In section 2.2 this has been discussed further. Other form of passive mode of droplet formation usually can be found in microfluidics where two co-flowing/cross-flowing fluids are used to generate droplets passively. We discuss some approaches of passive droplet formation on-demand in the following sections that have been found in literature.

Pressure driven passive droplet generator: Passive droplet formation approaches require flowing of (cow-flow, cross-flow, T-junction) two immiscible fluids, where, the fluid for which the droplets will be generated are usually known as dispersed fluid and the other fluid that is immiscible is known as continuous fluid. The breakup of the aqueous fluid in shear-based approaches can occur in different modes, such as, i) squeezing, ii) dripping, iii) jetting, iv) tip-streaming and v) tip-multi-breaking.

Flow focusing passive droplet generator: In the flow-focusing devices dispersed liquid is flown through a confined channel and the pressure caused by the continuous liquid surrounding the dispersed liquid continues to build until squeezing takes place and causes detachment of the droplets.

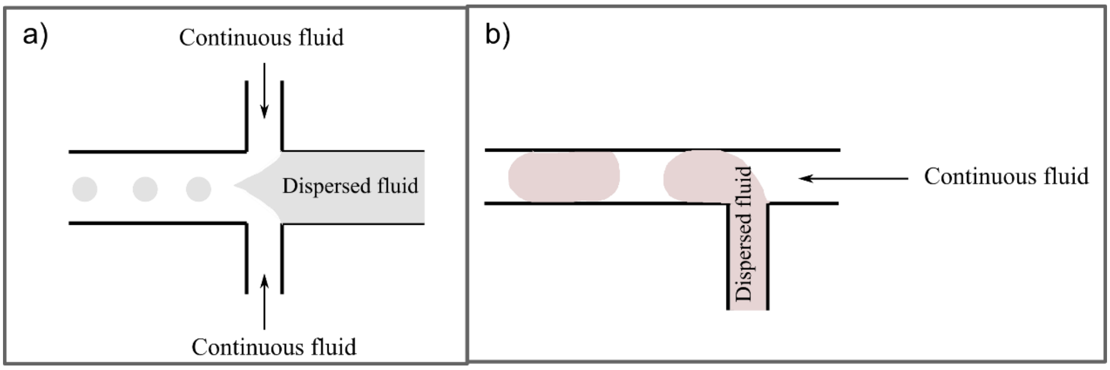

Figure 2:15: Pressure driven droplet formation using multiple co-flowing fluid. a) Squeezing mode of droplet breakup. b) Dripping mode of droplet breakup.

When, the dispersed fluid is flown with a flow rate Q_a and the carrier fluid is flown with a flow rate Q_c. The ratio of Q_c and Q_a is important to decide the size of droplet formation. At the junction, shear force of the career and the interfacial tension are kept balanced as, $F_{drag} = F_{interfacial}$. Due to shear force at some moment the droplet detaches itself from the aqueous fluid, when $F_{drag} > F_{interfacial}$ enough. This droplet formation approach is known as dripping.

Jetting is another approach caused by instability in the flowing jet, which can be achieved by increasing flow rate of any of the fluids, that leading to formation of droplets. Tip streaming and tip-multi-breaking are also achieved through the phenomenon discussed by Rayleigh-Plateau which has been elaborated in section 2.2. Figure 2.15 shows 2 scenarios where two fluids have been co-flown to achieve droplets via squeezing (Figure 2.15(a)) and dripping (Figure 2.11(b)).

2.6. Chapter Summary

Polydimethylsiloxane (PDMS) is a class of silicone-based polymer that is found in a wide range of applications in biomedical research laboratories and food/consumer industry. A primary reason for PDMS to be used in constructing lab-on-chip devices is because it exhibits high optical transparency, ease of manufacturability, mechanical deference, chemical stability (for inorganic solvents), non-toxicity, non-flammability and bio-compatibility. Liquid droplets extracted from fluid PDMS jet can be cured, via cross-linking to form three-dimensional network of soft plastics without using any mold (or using molds) to form high quality optical lenses [88-91]. Popular industry-based manufacturing of optical elements has been discussed to guide towards the motivation for the moldless droplet lens making approach.

As this work is focused on harvesting the droplets as optical lenses, our study does not end with the formation of droplets. It is pivotal to hold the droplets and retain them to harvest as lenses. Further discussion about the retention can be found in Chapter 3, where the proposed passive droplet dispenser has been elaborated.

It is undeniable that using a mold-based approach is costlier and requires high level of complex design processes to achieve products. Although, it is also undeniable that the quality and mass-manufacturability of the mold-based products are also high. However, we always quest for alternative manufacturing processes, that is high enough in quality and also can achieve mass-manufacturability, the manufacturing process that requires minimal operator training, least high-end laboratory equipment and space, and at low cost. This alternative approach then is a quality process, that aids in scientific advancement especially in the field of microscopic imaging, off-shelf prototyping of various compact imaging systems and also wearable technology.

CHAPTER 3

PRODUCTION AND PERFORMANCE ANALYSIS OF MOLDLESS LENSES

Plastic has been an alternative material for manufacturing optical components for decades [121]. As discussed in Chapter 2 through literature review, that they can be considered as quality counterpart of glass optics and can be better for designing prototypes in terms of mass manufacturability and cost. While injection molding is a highly sought out manufacturing process, the cost and complexity involved with molding approach make these approaches less attractive for consumer-based products and high throughput low-cost applications. In this chapter, we will discuss moldless lens making approaches that can produce high quality lenses with different dimensions and focal lengths, at no additional cost of machinery or without the need for extensive training. As already discussed in Chapter 2, moldless lenses have been manufactured using a highly viscous elastomer, known as PDMS (Dow Corning Sylgard 184) because of the optical and chemical qualities offered by PDMS, ease of accessibility and cost. During the course of this work, both passive and active droplet generation approaches have been used to acquire droplets of PDMS, which later were converted into lenses through polymerization. The lenses are easily attachable to a smart phone or tab and are capable of microscopic imaging on-the-go. These advantages make the moldless lenses very attractive for a wide range of stakeholders, starting from high school students to university students, researchers in academia or industry, or just science enthusiasts. In this chapter, we will thoroughly discuss about the moldless elastomer lens making approaches, characterization of the performances and comparison.

3.1. Passive droplet formation

Passive droplet formation is possible due to the role of various forces working on a liquid. In nature droplet forms through process of nucleation with the condensation of moisture. Alternatively, if there is a liquid flow then the jet breaks up into smaller masses due to the surface tension, velocity of the liquid, creating droplets. Droplet generation can be controlled and automated using various external means, forces, and triggers. This is known as active droplet generation. These concepts have been discussed in detail in chapter 2.

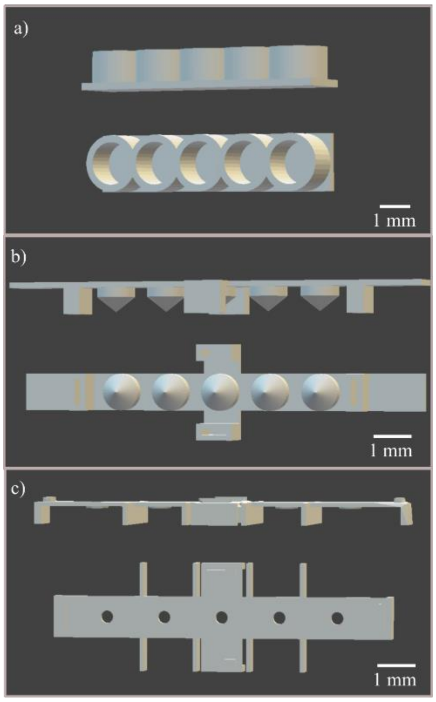

Figure 3:1:Ppassive droplet dispenser containing three-parts for moldless elastomer lens manufacturing. Both sideview and top-down view. a) Basin with 5 wells. b) Conic-dropper with 5 conic tips. c) Droplet-holder with 5 holes, each 3 mm diameter.

In the following subsections we will introduce a passive droplet dispenser for generating droplets on demand. We will also introduce alternative simple approach for active droplet generation, which was also used during this research. This demonstrates the possibilities of various moldless lenses using simple droplets.

3.2. Passive droplet dispenser

Here, a passive droplet dispenser for production of moldless elastomer lenses has been introduced. A set of tools have been designed and 3D printed (the design models have been shown in Figure 3.1) to acquire passive droplets of mixed PDMS. The tip-multi-breaking mode of droplet formation has been used in this approach, which is a consequence of Rayleigh-Plateau instability. Throughout this research ABS has been used for 3D printing. The proposed tools are a simple set of “dispenser” that use natural fluid dynamics concepts to extract liquid PDMS (mixed) droplets without using any external pressure or complicated, expensive laboratory equipment. The design has opened up opportunities for a simple lens manufacturing process with the capabilities of mass-manufacturability at low-cost [8]. The lenses developed using the passive dispenser contain a fixed base, that is fixed diameter (3 mm), but with different heights/radius of curvature, that is different degree of convexities, achieving varying levels of magnifications.

3.2.1. Design and optimization

The passive droplet dispenser comprises of three parts, i) a set of wells – will be called as basins, ii) a set of cones – will be called as conic-droppers and iii) a set of cylindrical holes – will be called as droplet-holders. Figure 3.1 shows the 3 different tools manufactured to dispense macro-droplets (of volume 20 – 35 µL) and hold the droplets to acquire optical lenses of different focal lengths (4 mm – 25 mm). While the acquired droplet volume depends on the factor of fluid dynamics (critical droplet volume), especially due to the Rayleigh-Plateau instability, the design goals for the manufacturing process set by our research, also allow certain control over the acquired volume of the droplets.

Design development process: The manufacturing process objectives were roughly outlined in Chapter 2. With the product "idea" and objectives in mind the passive droplet dispenser was developed. The idea originated from different literature that liquid elastomer droplets can be used to acquire lenses. But then the requirements for this product were different and so requirements analysis was done in the next stage.

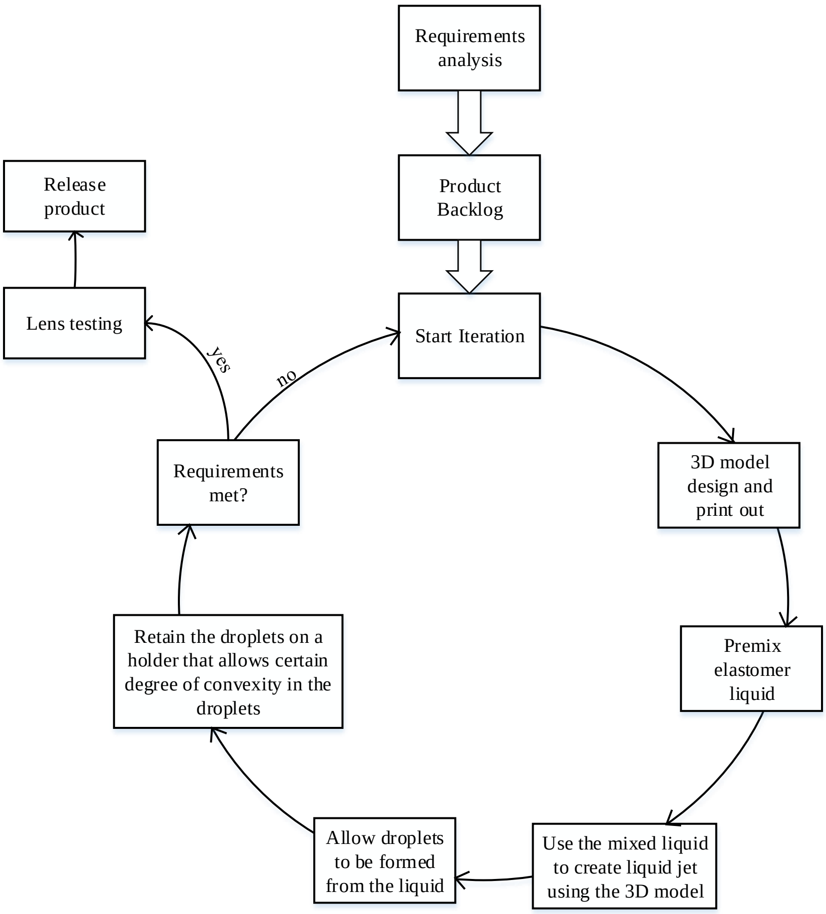

Figure 3:2: Product development life cycle (PDLC) for the passive droplet dispenser that went through iterations to reach to a set of 3D printed tools.

The overall "product development life cycle" has been articulated in Figure 3.2. We used "Agile Waterfall Hybrid model", which has been used for software development extensively, sometimes also known as "agifall", for the development process with the aim of increasing speed, decreasing cost and improving quality for formal and guided manufacturing of the passive droplet dispenser and elastomer lenses [149]. As "agifall" is a hybrid model it uses the strengths of both agile and waterfall methods. Agile method is a highly interactive method that uses feedback for product development, whereas, waterfall is a sequential, non-iterative approach of product development.

The developed dispenser, with the combined use of the 3 parts, has been able to create a PDMS liquid jet with sufficient instability to detach pendant drops, and hold the droplet in the holes of the droplet-holder successfully. At this stage, it is essential to verify the design and identify parameters in terms of the established fluid dynamics theories.

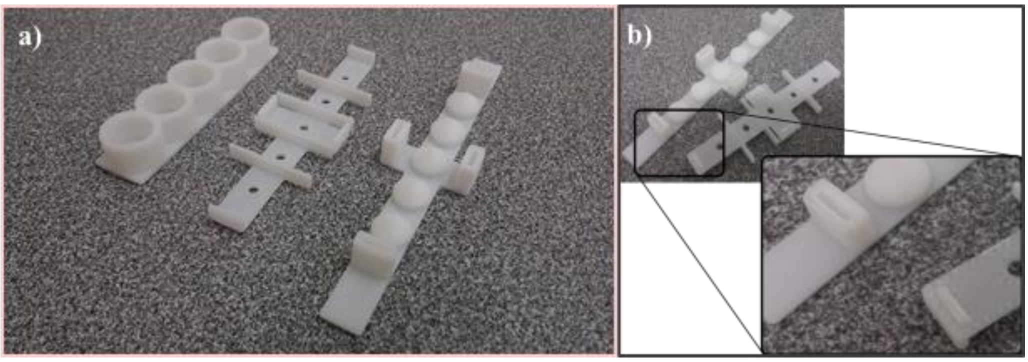

Figure 3:3: Passive droplet dispenser 3D printed parts printed using an UP mini printer using ABS as material. a) Three parts, basins, droplet-holder and conic-dropper respectively. b) Clipping mechanism in the design to achieve mechanical stability to avoid perturbation.

To discuss further it is imperative to introduce the roles of the 3 tools. The ABS printed tools have been shown in Figure 3.3(a). The use of the wells of the basin is to hold liquid mixed PDMS that is ready (free from entrapped air/bubbles) for lens-making. The conic-dropper has been designed to form a liquid jet that in turn generates droplets. To form the droplets using the cones, they are pressed into the basin filled with PDMS, and then pulled out to form a flowing PDMS jet. With sufficient instability the jet is able to detach droplet from the tip of the dropper. Lastly, the droplet-holder with 5 holes holds the droplets that have dripped off the tip of the cones. The holes of the holder perfectly align with the cone tips of the dropper using the clip attachments as shown in Figure 3.3(b).

Before discussing the optimization analysis, it is important to note that the fluid dynamics analysis for the optimization of the dispenser has been done empirically mostly by observing the liquid jets, droplets using a simple, low-cost optical setup in the lab.

To elaborate on the analysis, we will dissect the process of moldless droplet lens making using the 3D printed tools in the following parts, i) immersion, ii) extraction, iii) formation of fluid jet, jetting iv) droplet detachment, dripping and v) retention of the droplet at the holder.

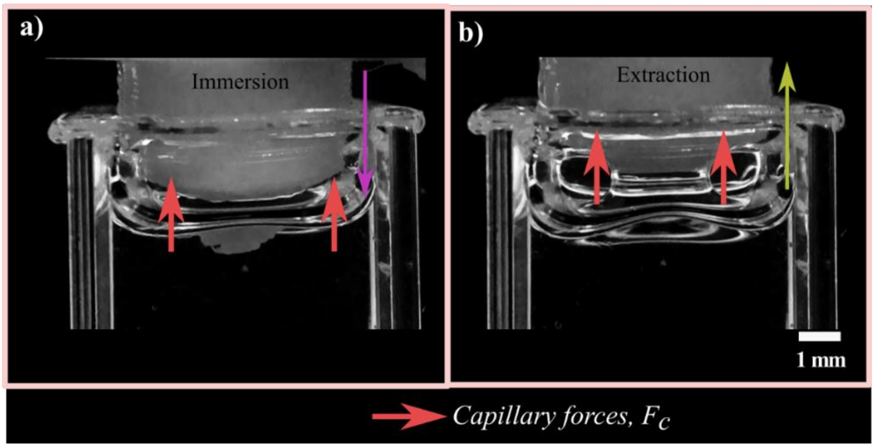

Figure 3:4: Demonstration of the fluidic behaviour when a plastic cone is immersed and extracted within/from a liquid. a) Immersion, b) Extraction. It is observable that due to capillary forces, the liquid attaches to the tip of the solid cone.

The immersion process is a simple consequence of capillary forces acting at the solid-liquid interface when the conic-dropper is pressed into the wells of the basin (assuming the dip is happening at 80% height of the cone). This step has been shown in Figure 3.4(a). For the sake of observing the capillary forces a transparent cuvette has been used. In Figure 3.4(b) the conic-dropper is being pulled out of the liquid where the liquid is attached at the tip of the cone. We refer to this step as, extraction. The viscosity and density of the liquid is important in determining the amount of liquid retaining at the tip of the cone.

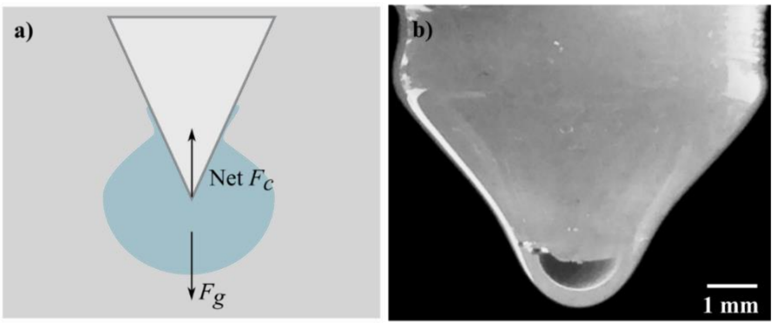

Figure 3:5: Post extraction tip of the cone accumulating a volume of liquid PDMS. a) Schematic showing different forces acting during this observation. b) Experimental observation of the tip of one cone after immersion/extraction.

As soon as the tip of the cone is extracted, liquid attached at the tip of the cone can be observed to accumulate a mass as shown in Figure 3.5 (both schematically and empirically). The different forces acting on the droplet at the tip of the cone, has been shown in Figure 3.5(a). Here F_c is the net capillary force, and F_g is the force caused by the gravitational acceleration. Figure 3.5(b) shows a PDMS drop forming at the tip of the proposed conic-dropper. Following this event, a liquid jet immediately forms, and jetting occurs.

As shown in Chapter 2, and in Figure 3.6 (video of flowing jet has been acquired using the raspberry pi camera at 90 fps) the flowing liquid jet starts elongating and due to the instability discussed by Rayleigh-Plateau, droplet forms when the mass at the tip of the flow is sufficient enough, the jet radius starts reducing.

As soon as the jet radius is thing enough, the droplet detaches itself from the liquid jet and dripping happens. The moment before a droplet is getting detached has been captured and shown in Figure 3.7. It is observable that the jet radius got reduced and the jet has elongated compared to Figure 3.6.

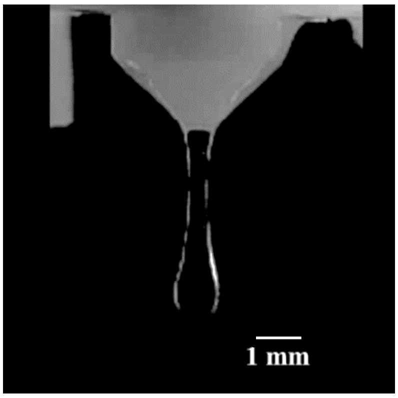

Figure 3:6: Jetting when the tip of the cone has been pulled out of the basin. In order to observe the jetting behaviour, the jet has been allowed to fall freely. We can see that a droplet has been formed at the tip of the jet.

While the drop is free flowing at the direction of gravitational force it gains momentum. So, the Bond number, Bo $\gg 1$ decides the momentum of the liquid jet. After the droplet drips it needs to be retained so that it can be cured/polymerized to perform as an optical lens. The droplet-holder providing a thin (0.9 mm height) capillary, works as a holder that provides sufficient capillary force to hold the droplet. Hence, a droplet is retained.

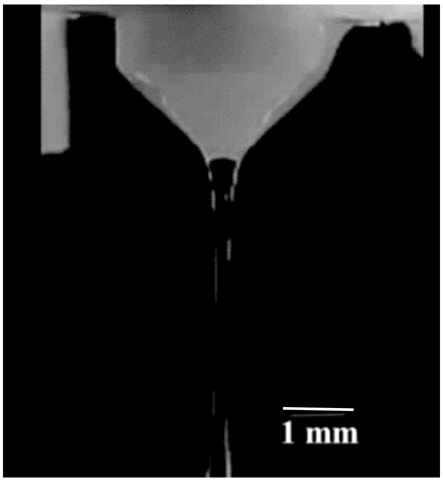

Figure 3:7: Due to Rayleigh-Plateau instability a liquid jet forms. Then we can observe the dripping process, just the moment before a droplet is getting detached from the flowing liquid jet.

A schematic of the different forces working on the droplet at the droplet-holder has been shown in Figure 3.8(a), whereas Figure 3.8(b) shows a droplet has been retained at our proposed 3D printed droplet-holder.

In the next sub-sections, we will discuss how the dispenser design has been optimized by observing fluid dynamics at different stages of droplet formation.

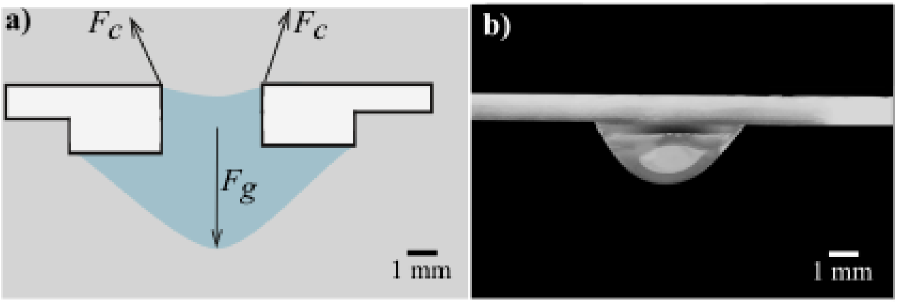

Figure 3:8: Thin height (~1 mm) droplet holder holding a droplet. a) Schematic depiction of the process with different forces shown. b) Experimental observation of the retention step.

Optimization of the dispenser (conic-dropper): As we worked out the design of the dispenser was able to have high droplet retention rate, it was important to discover the optimality of the design. In Figure 3.9 a set of cones have been shown where the cone angles have been varied. Figure 3.9(a) shows the flattest cone tip with angle 16.9º. The proposed cone tip has been shown in Figure 3.9(b) with angle 31.1º. We observed behavior of a steep cone with the angle 58.3º as shown in Figure 3.9(c).

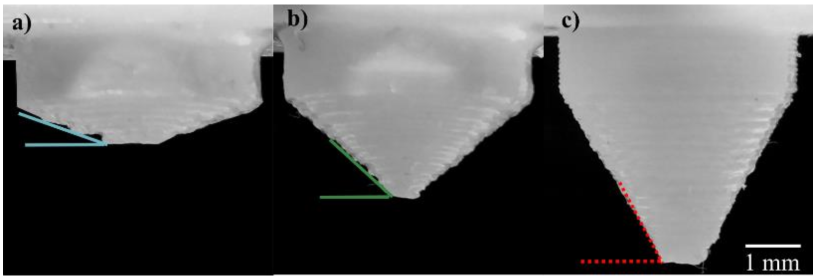

Figure 3:9: Three different conic-droppers with varying cone angles, in order to find an optimum cone angle. a) Flattest tip with cone angle 16.9º. b) Proposed conic-dropper with angle 31.1º and, c) Steepest cone with the angle 58.3º.

Figure 3.10 shows the same tip of cones, after immersion and extraction took place, that is with retained PDMS liquid at the tip of the cones. It is observable that the height of the droplets as seen in Figure 3.10 are proportional to the cone angle, that is the flatter the cone (less angle) the smaller the height. The height h_1, shown in Figure 3.10(a), at the tip of the flat cone is smallest. Whereas h_2 and h_3 are comparatively larger, shown in Figure 3.10(b) and Figure 3.10(c) respectively.

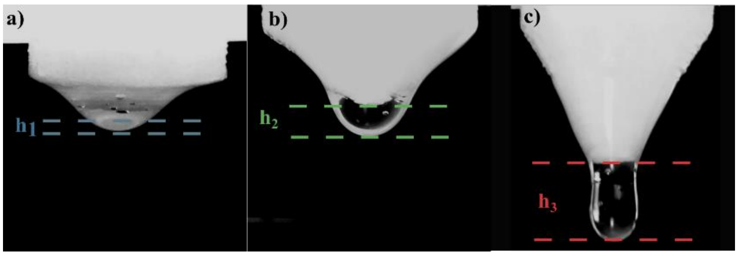

Figure 3:10: Amount of PDMS acquired after immersion/extraction using three different conic-droppers earlier shown in Figure 3.10.

The volume at the tip depends on, i) the capillary rise getting restricted when the angle is flatter, and ii) the surface area available at the tip of the cone being smaller. An angle of 16.9° provides a cone tip that can obtain insufficient amount of droplet volume (height $h_1 \approx 0.5$ mm) at the tip of cone, allowing a small height of the droplet, resulting into a bond number of ~0.1 which indicates that the interfacial forces are dominating, compared to the gravitational force. Consequently, this cone tip fails to provide a flowing liquid jet and hence is not suitable for droplet generation.

If we keep increasing the cone angle of the tip then the amount of volume at the tip of the cone increases. When we reach our proposed dispenser cone angle (38.9°), we acquire sufficient height of the droplet at the tip of the cone, $h_2 = 2.2$ mm, that can generate a bond number of ~2.19 that is sufficiently large to create a flowing jet. If we keep increasing the angle of the cone and reach ~58.3°, higher PDMS volume is retained at the tip of the cone, of $h_3 \approx 5.5$ mm and can successfully create a fluid jet as the bond number is even higher, ~13.7. While observing different flowing jet from the different cone tips, it was observable that no jet was created from the cone shown in Figure 3.9(a), as the amount of PDMS attached at the tip of the flat cone is not sufficient. Whereas, the flowing jet using the proposed conic-dropper of angle 38.9°, a single droplet is generated.

However, the steeper cone retains large volume of PDMS at the tip. Consequently, the liquid jet has larger momentum and has higher volume; that leads to generation of multiple droplets. The generation of following droplets are known as, satellite droplets, which follow the parent droplet. For our proposed dispenser this is undesirable as the droplet-holder does not have sufficient capillary to hold more than one droplet at a time. Hence, despite acquiring a flowing jet successfully, the conic-dropper with steeper angle is incapable of successfully retaining droplets.

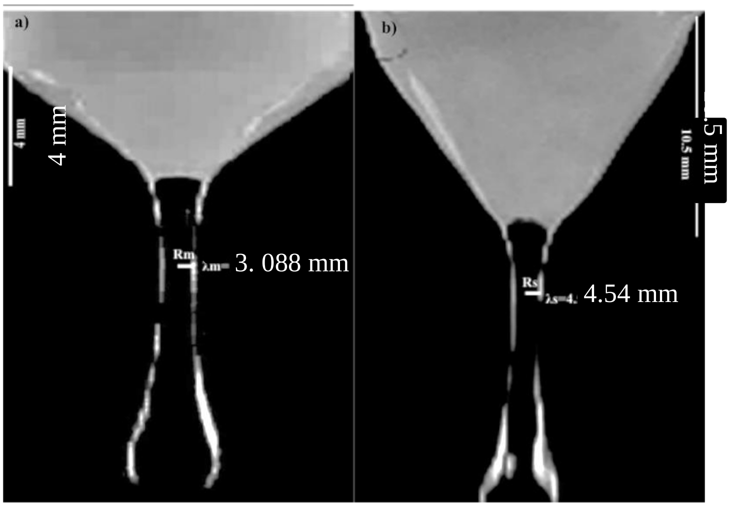

Figure 3:11: Two different flowing jets from the tip of two different conic-droppers. a) Proposed conic-dropper generating a jet of radius 3.088 mm. b) The steep conic-dropper generating a jet of 4.54 mm radius.

. To quantify the differences in the two different jets produced by the proposed conic dropper and a steep conic-dropper, we show the two different jets in Figure 3.11. The radii of the two jets are different. The steeper cone generating larger radius indicates there is higher volume of PDMS.

In order to further demonstrate the amount of liquid generated from the different conic-droppers with varying cones, we placed a droplet-holder under each of the dropper to hold the droplets generated. This observation has been outlined in Figure 3.12. Figure 3.12(a) has no droplet retained at the holder, understandably as there has been no flowing jet from the flat cone tip. Figure 3.12(b) is the proposed conic-dropper and the holder retains a droplet of sufficient height and convexity as desirable for an optical lens. However, due to multiple droplets generating at the tip of the steep conic-dropper, Figure 3.12(c) shows the liquid PDMS flowing through the hole of the droplet-holder, with an unsuccessful retention.

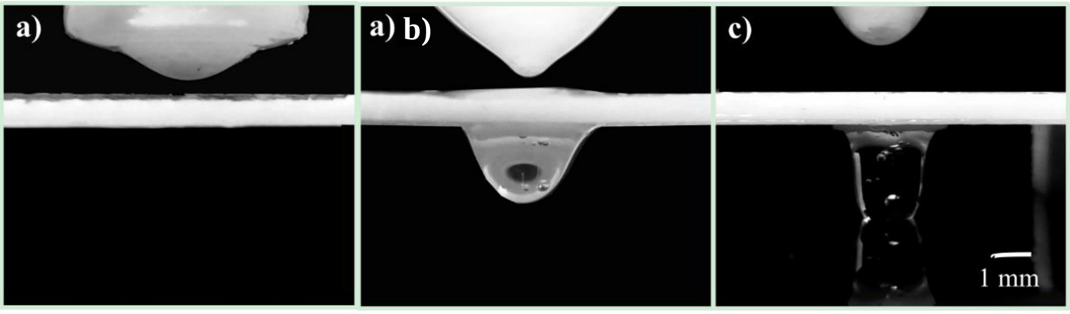

Figure 3:12: Three different conic-droppers of different angles, generating droplets that are supposed to be retained at the droplet-holder. a) The dropper with a flat cone is unable to produce a successful droplet. b) Proposed conic-dropper generating a droplet. c) Steep conic-dropper generating liquid with multiple droplets and larger volume that is falling through the hole due to larger bond number.

So, the proposed conic-dropper can extract sufficient PDMS at the tip of the cone that forms into a falling jet. Due to tip-multi-breaking then, a droplet is detached from the jet.

Optimization of the height between dropper and holder: As the conic-dropper forms a fluid jet and we place the dropper on the holder to hold the droplets, the height between the dropper and holder is a design factor that has been considered. As the liquid jet elongates (with radius r) and a sinusoid is generated with a wavelength, $\lambda_{jet} = 2\sqrt{2}\pi r$ [150]. For a PDMS liquid jet forming at the tip of the proposed dropper, through several experimental observations we found that the jet radius is ~0.34 mm providing a wavelength of ~3 mm. We used $\frac{\lambda_{jet}}{6} = 0.5$ mm to let the droplet have enough momentum to reach the holder and can be successfully retained. If we reduce the distance to $\frac{\lambda_{jet}}{8}$, the droplet gains more momentum and then the holder fails to successfully retain the droplet. Sinusoids arising from PDMS fluid jets can be seen in Figure 3.11.

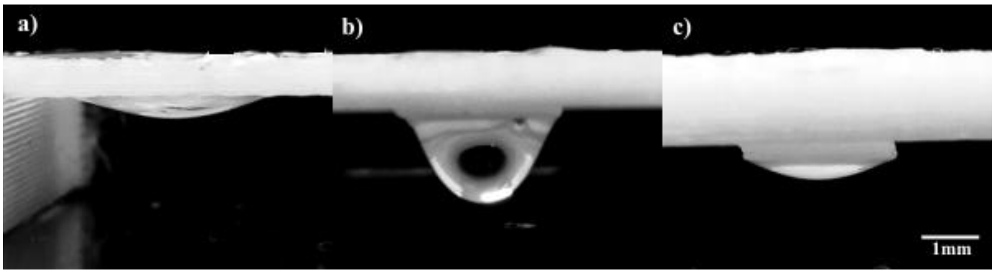

Figure 3:13: Droplet-holder with varying heights. a) Wetting/spreading observed at a droplet-holder of 0.5 mm height. b) Droplet-holder of 0.9 mm height, the proposed design holding a droplet of PDMS. c) A 2.82 mm height droplet-holder generating a droplet of very small convexity.

Optimization of the dispenser (droplet-holder): The droplet-holder contains holes of 3 mm diameter each and has a thickness of 0.9 mm providing sufficient capillary to retain droplets detached from the flowing liquid jet, as discussed earlier. We observed variation in thickness of the holder (0.5 mm, 0.9 mm and 2.82 mm) as shown in Figure 3.13(a), (b) and (c), respectively. While, a thinner capillary of 0.5 mm can retain droplets but does not provide a successful lens. The thinner holder causes wetting/spreading of the liquid droplet hanging at the hole due to insufficient capillary at the holder. Whereas, the thicker holder with 2 mm height can also successfully retain droplets but with a tall base and smaller achievable convexity.

As shown in Figure 3.14, the thicker droplet-holder causes a tall stem at the base of the lens, reducing the achievable convexity of the lenses. The lenses also don’t perform as a thin lens as desired by this work. However, when we use the proposed droplet-holder, a small base of less than 1 mm is generated and that does not impact the lens performance significantly. Figure 3.14(a) shows the 3D printed droplet-holder of 2.82 mm with a droplet of PDMS hanging at the hole. The moldless lens acquired using this holder can be seen in Figure 3.14(b), with evidently a longer stem, which is no longer a thin lens. Figure 3.14(c)-(d) schematically depicts the scenario of a thicker base of the droplet-holder.

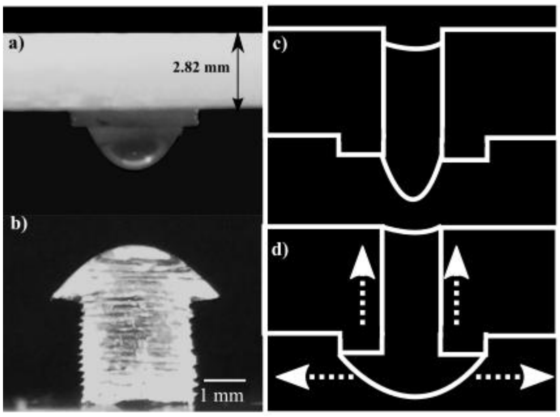

Figure 3:14: A lens harvested using the thick droplet-holder showing a thick cylindrical stem. a) The thick holder used to harvest the lens. b) A shadow image of the lens. c) Schematic showing the thick holder retaining liquid PDMS. d) Due to capillary rise the liquid is pulled up through the thick droplet-holder cylinder.

The proposed droplet-holder is capable of successfully retaining droplets with varying heights (up to ~ 3.5 mm) as the holder contains a barrier that restricts wetting/spreading and pins down the droplet at the periphery of the barrier. This has been articulated in Figure 3.15.

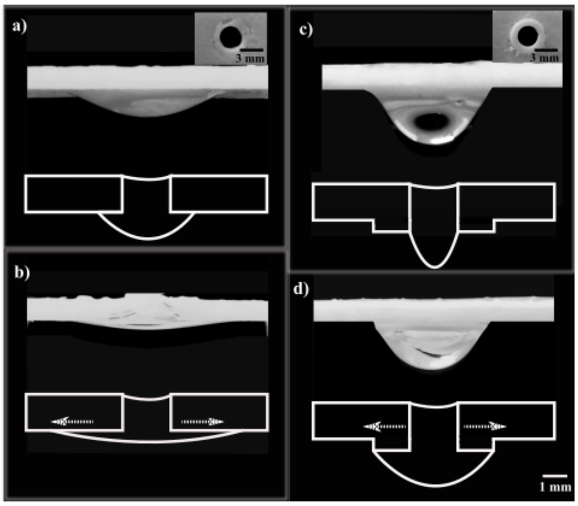

Figure 3:15: Wetting/spreading and pinning effect. a) A hole of a droplet-holder without the proposed barrier. b) Spreading/wetting causes the droplet to disperse as much as possible. c) A hole of the proposed droplet-holder with a droplet retained. A 0.5 mm thick barrier has been shown inset. d) The droplet height reduced by a small margin due to wetting/spreading and inertia caused by surface tension. The spreading has been pinned at the edge of the barrier.

Figure 3.15(a) shows a 3 mm hole of a droplet-holder which was printed without the barrier, as can be seen in the inset. While there is no barrier the impact of spreading/wetting continues to reduce the contact angle as has been previously discussed in Chapter 2.

3.2.2. Lens making process:

The proposed passive dispenser is capable of dispensing on-demand droplets without the necessity of laboratory setup or high-quality operator training with high success rate. It is also important to discuss how the droplets are extracted and later polymerized to obtain optical lenses which have been demonstrated with the use of a process flow diagram as shown in Figure 3.16(a) and graphically in Figure 3.16(b).

Required Equipment (for quick and best results): For this lens making approach we will require, i) assuming a precision (UP mini printer) 3D printer has been used to print out the 3D printed tools successfully with supports removed, ii) a clean beaker/plastic cup, iii) a clean spoon/stirrer, iv) a pair of gloves (not mandatory as PDMS is non-toxic), v) for quick results, a vacuum pump (or alternatively a simple air tight jar/desiccator for longer time) – to ensure no entrapped air/bubble remains in the PDMS mixture, vi) a convection oven (to provide higher temperature for rapid curing). If an oven is being used preheating the oven while the start of the process at 70-80ºC is a good idea to speed up the whole process, vii) a plastic syringe – 5 ml, viii) a timer to track time, ix) PDMS in two parts (base and cross-linker/curing agent).

The process starts by acquiring raw material, here, PDMS Sylgard 184. Desired amount of PDMS base is mixed with the cross-linker/curing agent as a ratio of 10:1 which ensures sufficient viscosity in the fluid to allow forming a liquid jet and once polymerized, solid plastic lenses with sufficient deformability. That is for a PDMS base of 20 ml, 2 ml cross-linker is mixed. Liquid PDMS base, cross-linker is poured in a clean jar and stirred using a stirrer for 3-4 minutes.

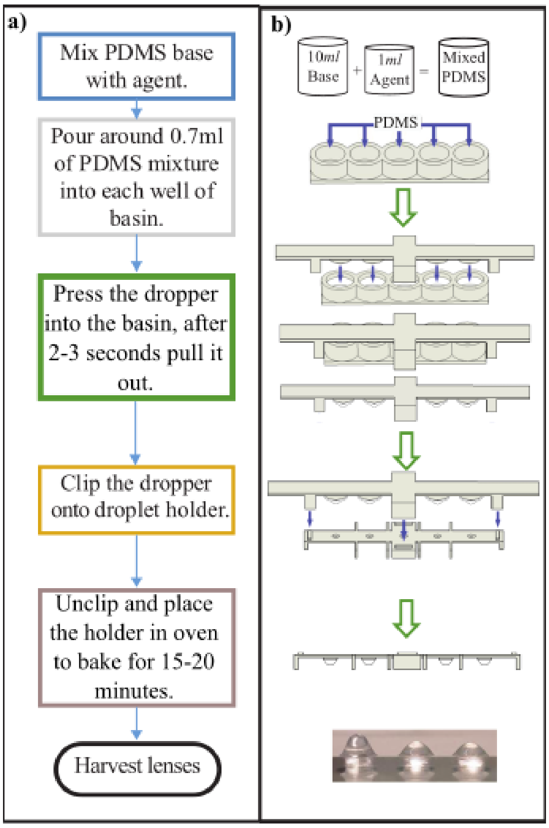

Figure 3:16: Lens making process using the passive droplet dispenser. a) Using a flow chart the process has been articulated. b) Graphical demonstration of the process.

As the mixed liquid contains a lot of entrapped air, which is undesirable in an optical lens, we use a vacuum pump for 15-20 minutes. The required time is proportional to the amount of PDMS mixture is getting de-gassed, the higher the amount, the more time is required. If the mixing is done in vacuum, then this step is not mandatory. Furthermore, the use of a desiccator or air tight container can be used to naturally degas the liquid mixture, typically in 2 hours for 30 ml of liquid. A timer can be used to keep track of time.

Now, to use the 3D printed tools, we fill-up the basin wells. A clean syringe is used to extract ~ 3.5 ml PDMS mixture, that has been de-gassed and then made sure no bubble retains in the syringe. Each well of basin is then filled-up (~80% requiring ~ 0.7 ml liquid).

At this stage, the conic-dropper is pressed into the wells (2-3 seconds) of the basin to cover 80% surface area of the tip of the cone. This ensures sufficient PDMS liquid is extracted at the tip of the cone to generate a desired liquid jet.

As the liquid jet starts to form at the tip of the cone, we quickly move the conic-dropper to attach with the droplet-holder. As already mentioned, the clips at the 4 corners of the droplet-holder align with the 4 slots designed in the conic-dropper, ensuring the cone tip and the holes perfectly align. In 3-5 seconds a droplet forms, due to the falling jet perturbation and Rayleigh-Plateau instability, detaches itself from the jet and drips onto the hole of the holder. The conic dropper is then unclipped to allow the droplets sitting at the holes of the holder be stable.

The droplet-holder is then placed into an oven (preheated) for around 25-30 minutes. The temperature and time relationship for PDMS curing has been summarized in Appendix - A, Table A. But here, it is worth mentioning that the droplet-holder is made of acrylonitrile-butadiene-styrene (ABS) and can be warped if too high temperature is used for curing, as the temperature tolerance for ABS ranges from -4ºC to + 80ºC.

After the curing process lenses can be found at the droplet-holder. In Figure 3.16(b) we can see some moldless lenses with different heights. Each lens in the Figure has a different level of magnification, with the leftmost having higher magnification capabilities, connoting, the higher degree of convexity allowing higher magnification (with shorter focal length, hence working distance).

Process summary: The passive dispenser can dispense droplets without the need for active force, with the use of gravitational force and fluid jet behavior droplets are generated. Droplets vary in height (1 mm – 3.4 mm) with a fixed base of 3 mm. Achieved focal lengths vary from 3.5 mm – 20 mm. A single 3D printed support can be used for any of these lenses for optical alignment. The promise of mass-manufacturability can be seen in Figure 3.17.

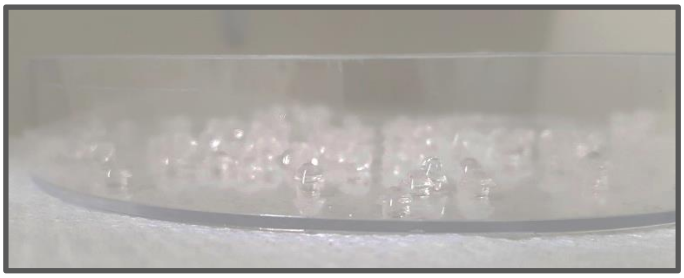

Figure 3:17: Lenses of various heights produced using the passive droplet approach. The high throughput of this moldless approach also has one added advantage, that the cost per lens does not depend on the number of lenses produced. The lenses cost ~1 cent per lens.

3.2.3. Drawbacks of the process

The passive droplet-dispenser can generate 5 droplets per iteration per set of tools, and if we have more than one droplet-holder (print duration 24 minutes using UP mini printer) the conic-dropper can be used more than once and steps 3-5 can be repeated once more to acquire 5 more droplets. However, like every process, this proposed approach has some drawbacks, such as, i) wastage of PDMS remaining in the basin wells. Although could be used as 10 mm diameter convex-concave lenses but due to surface roughness the performance would not be optimum, ii) printing of the 3D printed tools take approximately 2 hours if the 3 parts are printed at the same time. Iii) the circular holes of the droplet-holder are not symmetric. Hence the circular aperture of the produced lenses introduces distortions in images (imaging performances discussed in section 3.3). iv) the volume of acquired liquid droplets are not precisely controlled, hence the achieved magnifications are not precisely controlled during the manufacturing process. v) The clipping-unclipping process can cause more perturbation than desired resulting in unsuccessful droplets or low-quality lenses.

3.3. Active droplet dispenser for harvesting moldless elastomer lenses

The passive droplet dispenser is capable of on-demand droplet generation with success as discussed in the previous section. However, there are other moldless approaches that can open up alternative lens-making processes broadening the scope of applications and/or performances. Also, as literature review shows, there are more active droplet dispensers available for on-demand droplet generation, simplest being a syringe dripping a tip of liquid droplet when pressure is applied at the plunger of the syringe. The pendant droplet lenses have aspheric profile of curvature high due to the higher Bond number ≫1, suggesting gravitational forces dominated.

This lens-making process is a simple process that can be used to produce 100s of PDMS plano-convex lenses in just few seconds, as shown in Figure 3.18, a number of plano-convex lenses developed using this approach, with a yield rate of ~97%. The process does not ensure precise control of the base diameter and/or heights of the lenses but can produce high quality optical lenses. The process flow diagram and required equipment has been outlined in the following sections.

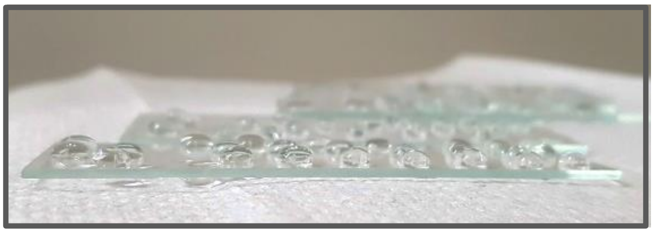

Figure 3:18: Plano-convex lenses of various diameter and heights manufactured using the simple active dispenser.

Required equipment: The following tools and equipment are required for making plano-convex PDMS lenses, i) a hot plate (preheat up to 200 ºC), ii) clean microscope glass slide, iii) clean syringe (1 ml), iv) PDMS in two parts, v) a clean plastic beaker/glass, vi) a plastic spoon/stirrer, vii), a vacuum pump (to speed up degassing) or desiccator, and viii) a timer.

The lens making process has been shown in Figure 3.19. In Figure 3.19(a) the process flow has been outlined whereas in Figure 3.19(b) graphical depiction has been shown. The process for this lens-making is similar to the previous lens making process discussed in section 3.2.2, where premixing of PDMS and degassing are required to acquire the raw material.

Once the liquid PDMS has been degassed, using a syringe (preferably 1 ml), a certain amount of liquid is extracted, and the syringe is loaded. A microscope glass slide needs to be cleaned properly and then placed carefully on the preheat hotplate.

Using the plunger of the syringe, a small amount of liquid is dripped onto the glass slide. This can be repeated as many times to acquire multiple droplets. As the hotplate has very high temperature, the droplets of liquid PDMS cures immediately (in less than 1 second), arresting the spreading/wetting of the PDMS and generating multiple plano-convex lenses in few seconds. This process allows to generate hemispherical lenses but requires very careful deposition of the liquid on the glass slide.

In Figure 3.18 we can see a slide full of lenses of different diameter and height, again achieving multiple levels of magnifications. This process can be improved if a flat-tip needle is used to control the volume of liquid that is deposited at the lens.

Drawbacks of the process: This process is a very simple process, that can be replicated easily, can generate multiple droplets and lenses in quick time, but also possess some drawbacks, such as, i) use of a very high temperature hotplate, so proper preventive measures (gloves, table where operating) must be taken, ii) as the active dispensing is done by a human with hands, a certain amount of tremor is expected, that can distort the expected shapes of the lenses. This can be improved by using a mechanical control method to control the force on the plunger, but with cost of complexity.

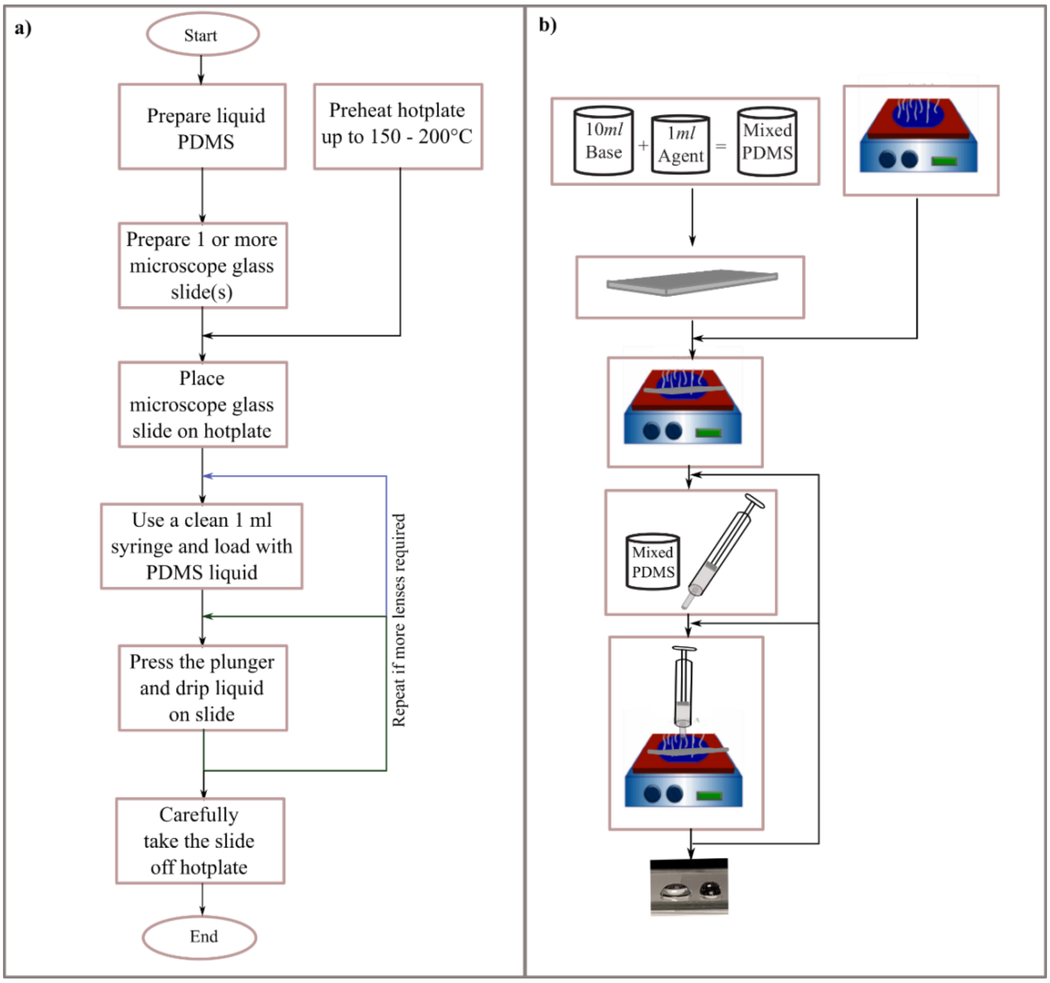

Figure 3:19: Simple active droplet dispensing plano-convex lens manufacturing process. a) Process flow chart. b) Graphical depiction of the process. Once the hotplate is preheat (up to 200 ºC), which takes 15 – 20 minutes, and the liquid PDMS is degassed within that time, then the lens-making process takes only a second to provide soft plastic lenses.

3.4. Performance analysis of passive droplet lenses

The lenses developed using the passive dispenser can achieve almost aspheric profile, due to the high gravitational bond number (Bo >1) that allow gravitational force to pull the pendant droplet hanging off the droplet-holder. As this process is quickly replicable without the need for new tools, a huge number of lenses can be easily produced. It is important to observe the quality of the lenses like any other manufacturing process. As obvious it is to observe imaging performance of the lenses, other optical analyses have been done on the lenses. For a number of optical characterization measurements, the passive droplet lenses have been compared with the performance of a commercial plastic aspheric lens (Thorlabs 352280, focal length 18.1 mm, diameter = 6 mm).

3.4.1. Wavefront observation using Shack Hartmann wavefront sensor

Typically, optical aberrations can be classified into two broad categories, geometric and chromatic aberrations. The geometric aberrations encompass the distortions that happen when light rays passing through a lens do not focus as they are expected to. This concept has been demonstrated in Figure 3.20 using both ray optics and wavefront. Ideally, light travelling through a lens is expected to focus at a single focal point, which is not true in practice. Figure 3.20(a) is a common geometric aberration, known as spherical aberration, where different rays focus at different points. The idea of aberration can also be seen as a wavefront. Whereas, the exit wave from a lens, which is expected to be spherical actually appear distorted, causing deterioration in image quality.

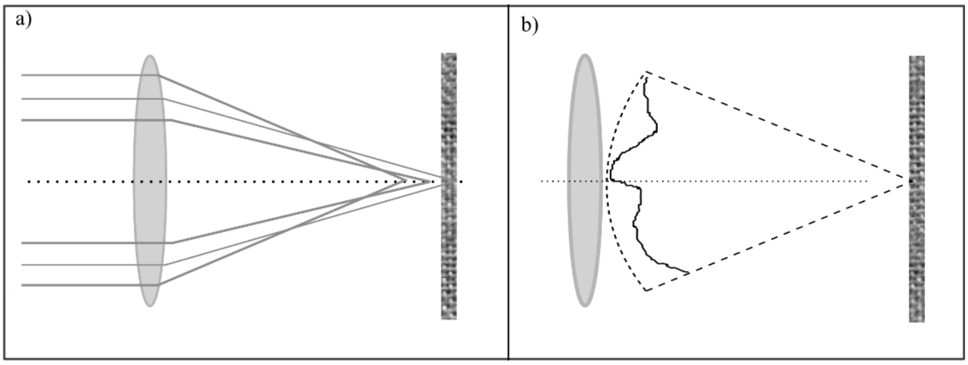

Figure 3:20: Geometric aberrations in optical lenses that can happen due to the inhomogeneity in refractive indices or irregularity at the surface of the lenses. a) Spherical aberration where different rays do not focus at a single point as expected. b) Wavefront distortion due to the geometric aberrations.

Shack Hartmann wavefront sensor (SHWFS) is an optical instrument created to find solution to a problem in late 1960s. The problem was posed by the US Air Force to the Optical Sciences Centre of University of Arizona in relation to the images acquired using a satellite, to improve the image quality. SHWFS works by using a set of lens array each of same focal length and measuring the deviation of the focal spot generated by each lens. SHWFS (Thorlabs, WFS150-5C) measures and decomposes optical aberrations into a set of orthonormal series of Zernike polynomials using an array of micro-lenses and a charged coupled device (CCD). The optical test bench setup used for SHWFS wavefront sensing has been shown in Figure 3.21.

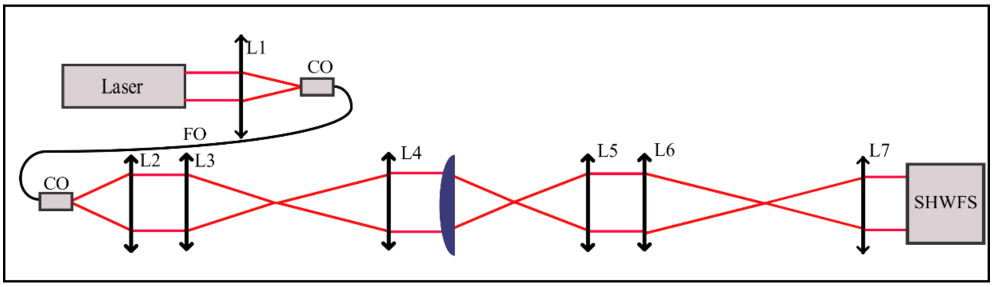

Figure 3:21: Optical setup for wavefront observation of the passive droplet lenses using a Shack Hartmann Wavefront Sensor.

A coherent laser diode (OBIS-Coherent, wavelength = 660 nm) has been used as the light source to test the aberrations. The first lens L_1 couples a low divergence output laser beam into a single mode fibre. The output from the single mode fibre is then collimated with L_2. The arrangements of lenses (L_3– L_7) are chosen to ensure matching conjugate planes and beam waist onto the input face of the SHWFS. The output beam goes through a pair of lenses (L_3, L_4) to expand the beam size to match the diameter (~2 mm) of the sample lens (PDMS or commercial aspheric). The sample lens under test, either passive droplet lens or commercial aspheric, is placed between L_4 and L_5, where L_5 collimates the output beam. The diameter of the beam output of L_5 is ~20 mm. Another pair of lenses (L_6 and L_7) has been used to reduce the beam diameter size to fill the active area of the SHWFS.

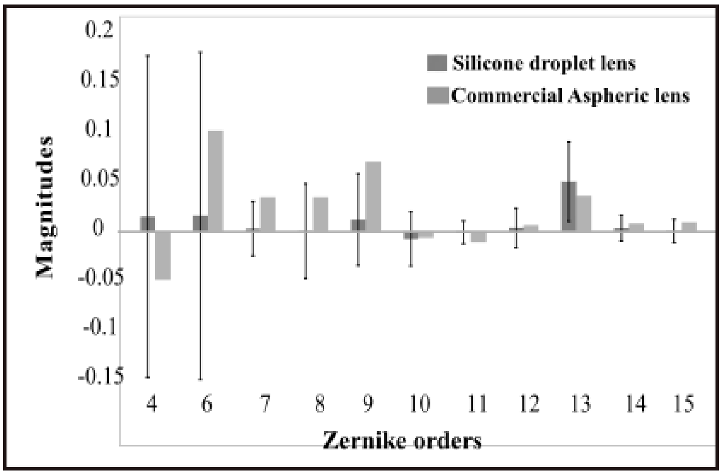

Figure 3:22: Magnitudes of different Zernike orders for the average of a total of 75 passive droplet lenses compared to the commercial aspheric lens (Thorlabs 352280).

The Zernike polynomials were used to express the magnitudes of the optical aberrations present in the lenses. Figure 3.22 shows the mean distribution of magnitude of the aberrations of over 75 PDMS lenses and the commercial aspheric lens. The results show that astigmatism and spherical aberrations from the silicone lenses are significantly larger than those from aspheric lenses. Astigmatism might have been introduced by the imperfect print of the droplet-holder, that show asymmetry in the printed holes, and unstable positioning during curing whereas spherical aberration has been caused by the non-aplanatic curvatures of the silicone lenses which are consequences of the almost conical shape of the curvatures. This observation has been found to be consistent while observing the spherical aberrations of lenses with shorter focal lengths. For this reason, further analysis has been done to observe the correlation between spherical aberration and focal lengths, as shown in Figure 3.23. The trendline suggests that the shorter the focal lengths, the higher the spherical aberrations, which is suggestable as the shorter focal length lenses have larger deviation from convexity.

For the next observation, we intended to find a control mechanism over the size of the lenses, that is if we could generate a lens of approximately f focal length.

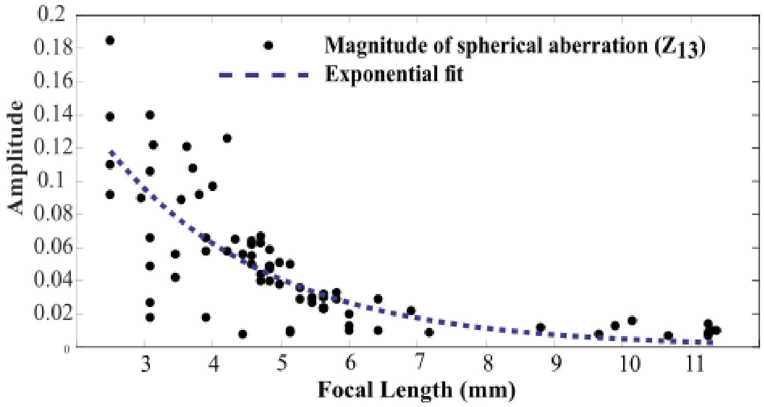

Figure 3:23: Magnitude of spherical aberration vs focal lengths of 75 passive droplet lenses.

The control over the height of the lenses can be simply controlled by the amount of PDMS extracted at the tip of the cone. If a single conic-dropper is used and the immersion/extraction process is done on the same basin wells, with each subsequent immersion/extraction, it is expected that the amount of liquid in the basin would reduce gradually.

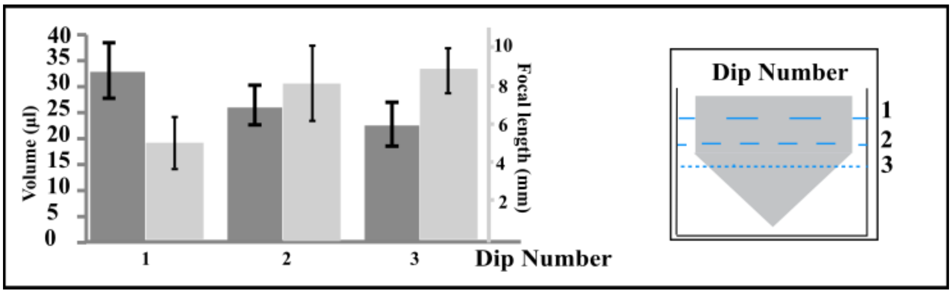

Figure 3:24: After filling up the basin wells, if a same conic-dropper has been used for immersion/extraction of liquid PDMS, with each subsequent immersion/extraction, the amount of liquid at the tip of the cone reduces. The bar graph shows, size of droplet acquired after each dip, alongside the corresponding focal lengths. The numbers 1, 2, and 3 in the horizontal axis refers to number of immersion/extractions.

Hence the amount of liquid retaining at the tip of the cones would gradually reduce too. This would cause large variation of focal lengths among the lenses yielding from each subsequent immersion/extraction (or dip) as shown in Figure 3.24. Dips 1 to 3 each produce lenses with increasing focal lengths ranging from ~3.5 mm to ~15 mm.

3.4.2. Focal length Optimization

Although the passive droplet lenses can be fabricated easily, focal length of the lenses have significant differences, as shown previously in Figure 3.23. This is due to coarse passive extraction process by the 3D printed cone. As such, it is important to quantify the focal lengths of the lenses. While standard focal length measurement provides an accurate measure of the focal lengths, it often requires a fair complex imaging setup. Here, we proposed a simpler method to quantify the focal lengths by simply capturing the profiles of the lenses and then mapping out the radii of the curvatures. The focal lengths have then been compared with the standard focal length measurements for accuracy.

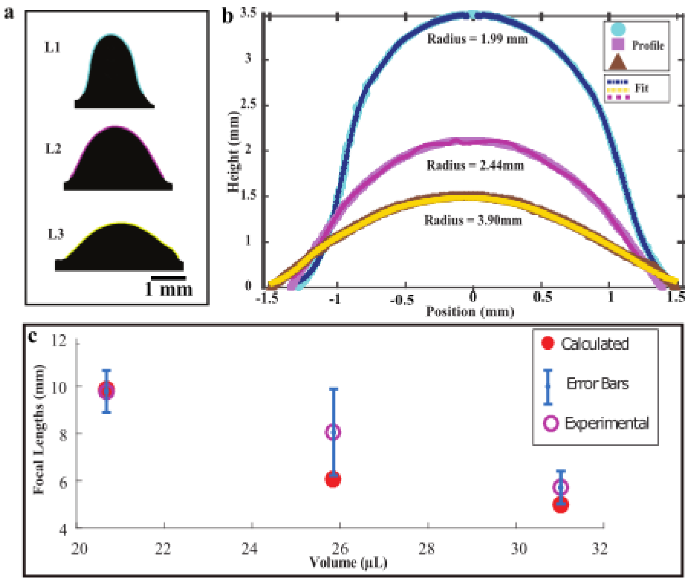

Figure 3:25: Focal length optimization. a) Shadow imaging of three different passive droplet lenses. b) Curve tracing and fitting of the curvatures of the corresponding lenses. c) Calculated vs. experimental focal lengths.

Figure 3.25(a) shows the outline of 3 passive droplet lenses that were captured using a simple optical setup consisting of a spherical lens of 30 mm focal length, Raspberry Pi camera and illuminating light. Figure 3.25(b) shows the surface profile of different silicone lenses. The surfaces of the lenses were found to be parabolic with varying heights and curvatures. All the profiles were captured through simple edge detection technique and then fitted onto a polynomial fit (shown in Figure 3.25(b)). The focal lengths were calculated at the vertex of the curvature of the lenses. Passive droplet lenses with longer focal lengths have a smaller amount of PDMS that result in a reduction of radii of curvatures of the lenses and vice versa. Based on the curvature profiles shown in Figure 3.25(a) - 3.25(b), the focal lengths have been calculated using the lens maker equation $\frac{1}{f} = (n-1)\left(\frac{1}{R_1} - \frac{1}{R_2}\right)$, where n is the refractive index of the lens and R_1 and R_2 are the radii of curvatures of each lens. In Figure 3.25(c) experimental and calculated focal lengths have been plotted.

3.4.3. Surface roughness measurement

During curing, it is also possible that the delicate liquid air interface of droplet formation can introduce uneven surfaces on the passive droplets [151]. To study the amount of unevenness, surface roughness of the lenses was measured using an optical profiler (Wyko NT9100: Mirau interferometer) and compared against a commercial aspheric lens (Thorlabs 352280). The results, as shown in Figure 3.26 in the forms of the 3D maps and cross-sectional plots, suggest that the passive droplet elastomer lenses (shown in Figure 3.26(a) and Figure 3.26(b)) have a highly conforming surface. Commercial aspheric lenses are shown in Figure 3.26(c) and Figure 3.26(d). The measurements suggest that the passive droplet lenses possess lower magnitude of surface roughness compared to the commercial aspheric lens. The RMS value of the surface roughness of the commercial aspheric lens was found to be 15 nm and for the silicone lenses harvested using the passive dispenser was found to be 3.21 nm for the front surface and 1.91 nm for the back surface.

3.4.4. Imaging performance of the passive droplet lenses

Various passive droplet lenses have been used for imaging various samples over a period of time during the research. In this section we summarize the performance of 3 different groups of passive droplet lenses, as grouped previously, by focal lengths and/or height of the curvature.

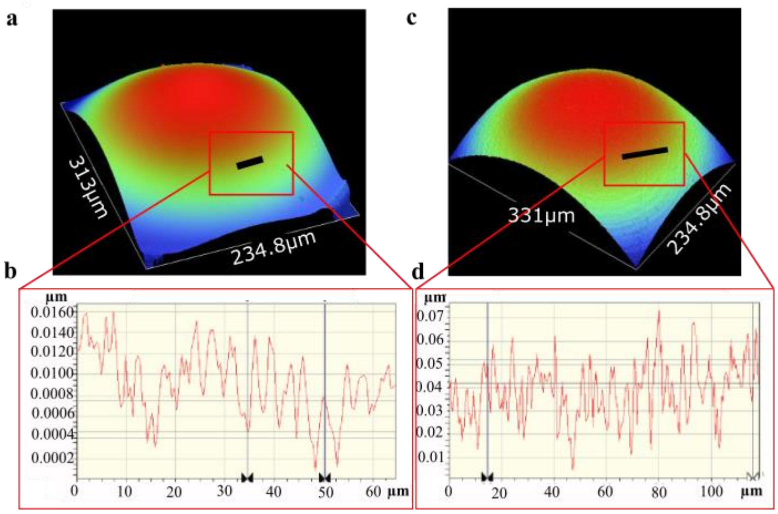

Figure 3:26: Surface roughness measurements. a) Front surface of a passive droplet elastomer lens. b) Line plot of the line section shown. c) Front surface of the commercial aspheric lens (Thorlabs 352280). d) Corresponding line plot.

Using a raspberry pi camera and simple LED, a transmission-based imaging setup has been built. The imaging setup can be seen in Figure 3.27. A USAF 1951 resolution target card has been imaged using different passive droplet lenses of different magnifications and a commercial aspheric glass lens using the experimental setup shown in Figure 3.27. The acquired images have been summarized in Figure 3.28.

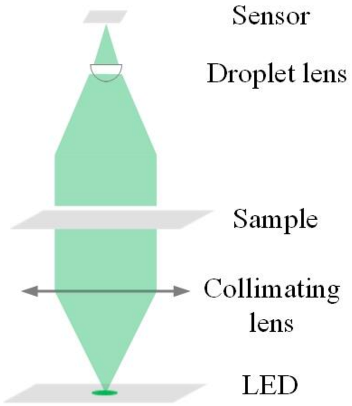

Figure 3:27: Transmission based imaging setup for imaging using various droplet lenses. A single LED has been used to illuminate the sample with the use of a collimating lens. Different moldless lenses were used for imaging. The camera used in this setup is a raspberry pi camera with a built-in lens.

In Figure 3.28(a) groups 2 and 3 of the target card are clearly visible with up to element 1 of group 4 resolvable (resulting into a resolution of ~30 µm). As seen in Figure 3.28(b) groups 4 and 5 can be resolved up to element 6, with ~8.77 µm resolution. The lens with the longest curvature producing the image in Figure 3.28(c) can resolve up to element 2 of group 7 yielding a resolution of ~3.4 µm. Figure 3.28(d) shows the image captured using the commercial aspheric lens.

The first 3 images have been acquired by three passive droplet lenses respectively. The lens parameters can be found in Table 3-1.

Table 3-1: Lens parameters corresponding to the lenses used for imaging of the samples as shown in Figure 3.28 and Figure 3.29.

Lens 1 **Passive droplet**	**Lens 2** **Passive droplet**	**Lens 3** **Passive droplet**	**Commercial** **Aspheric lens**
Focal length: 20 mm Height: 1.6 mm	Focal length: 10 mm Height: 2.4 mm	Focal length: 20 mm Height: 3.4 mm	Focal length: 18.1 mm Height: 1.5 mm

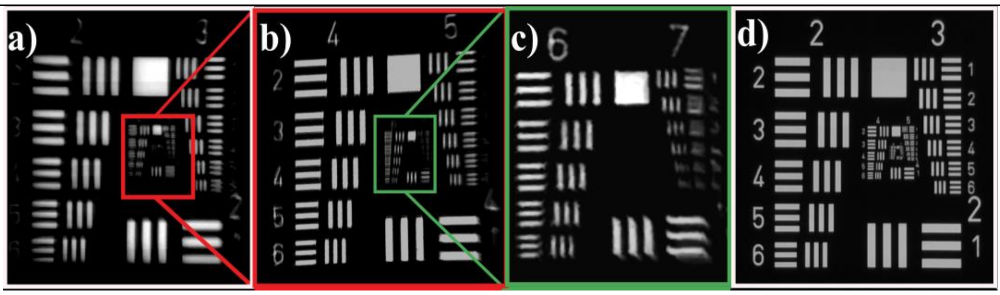

Figure 3:28: A negative USAF 1951 resolution target card with groups 0-7 imaged using various passive droplet lenses of various magnifications. Compared with commercial aspheric lens. a) Lens with longest focal length with larger FOV but reduced magnification. Achieved resolution is ~ 30 µm. b) Improved resolution (~ 8.77 µm) but reduced FOV image acquired using another moldless lens. c) The maximum resolution achieved using a short-focal length moldless lens, with a resolution of ~ 3.4 µm.

Figure 3.29 shows images of a histological slide of onion cells at the tip of an onion root, imaged using the same lenses as the USAF target card has been imaged. The lowest resolution image shown in Figure 3.29(a) shows the wider field-of-view structure of the onion root tip where the root cap and meristematic region can be seen with a part of elongation region. In Figure 3.29(b) the onion root image shows the root cap more resolvable with the cell walls and cells being more visible.

Figure 3.29(c) shows the clear view of the root cap with a number of cells and cell walls resolvable up to <15 µm. Figure 3.29(d) shows an image onion root, that has been captured using the commercial aspheric lens. The imaging performance of the passive droplet lenses are compatible with the commercial aspheric lens.

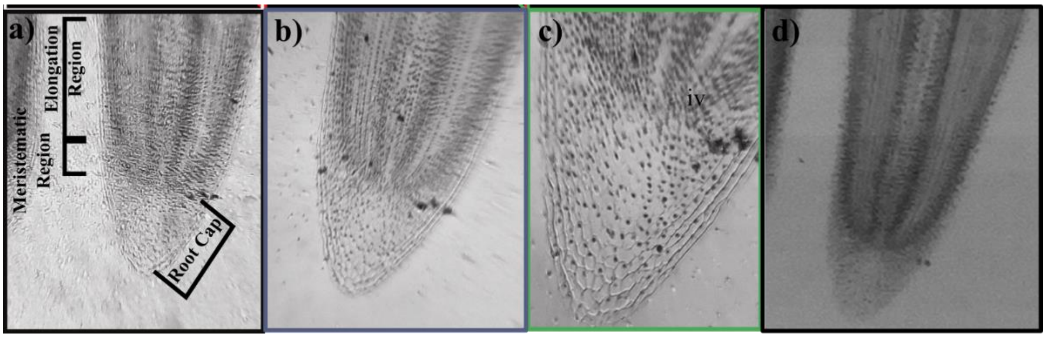

Figure 3:29: Tip of an onion root imaged using various passive droplet lenses and compared with commercial aspheric lens. Lenses used for these data are same as the lenses used in Figure 3.28.

3.5. Comparison among various moldless lens manufacturing methods

The different moldless lenses produced using the methods discussed in this chapter can be used for imaging in various optical setups, such as, with a clip on a smart device to have a portable microscope or on an optical table using opto-mechanical attachments. The different modes of imaging used for the imaging experiments are, i) transmission based imaging with both incoherent and partially coherent illumination, and ii) reflection based imaging using incoherent illumination.

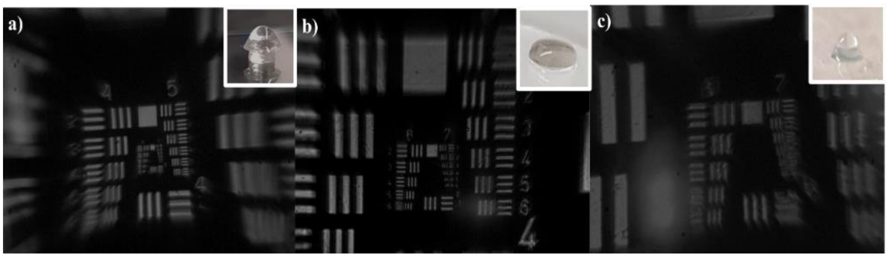

Figure 3:30: USAF target card images acquired using various moldless lenses. a) Passive droplet lens. b) Plano-convex lens using simple active approach. c) Thermal printed moldless lens (lens credit: Xu Tao).

In this section, the imaging performances of various moldless lenses have been articulated.

Table 3-2: Comparison among the different moldless lens-making approaches discussed.

Parameters	**Passive droplet dispenser based hanging droplet lens-making method**	**Active dispensed plano-convex lens-making method**	**Precision inverted moldless lens-making method (prototype shown in Figure 7.1*)**
Time required for lens making (post preheating of oven/stage and degassing)	20-25 minutes	5 seconds	5-10 seconds
No. of lenses acquired in above mentioned time	5	1	1
Replicability (post preheating of oven/stage and degassing)	High	High	High
Achievable resolution	up to ~2.76 µm (based on USAF 1951)	up to ~2.76 µm (based on USAF 1951)	up to ~2.76 µm (based on USAF 1951)
Precision	Low	Moderate	Higher
Complexity	Very low	Low	Higher
Expertise required	Low	Moderate	High
Focal lengths	3.5 mm – 25 mm	3 mm – 20 mm	3 mm – 20 mm
Base diameter	3 mm	2 mm – 6 mm	1.5 mm – 4 mm
Optical alignment	Comparatively easier because of the presence of ~1 mm stem at the base	Flat base so requires adhesive attachment	Smaller and flat base

In Figure 3.30 we have articulated images of an USAF target card acquired using 3 different lenses using 2 different manufacturing processes discussed in this chapter (the 3rd manufacturing process has not been shown as that is out of the scope this research but the imaging has been done with the lenses), with a passive droplet lens, a plano-convex lens and an inverted droplet lens, respectively. The properties of the lenses have been articulated in Table 3-2. As can be seen that the image in Figure 3.30(a) has higher optical distortions at the periphery of the images. This distortion is actually proportional to degree of convexity of the lenses as shown in Figure 3.25. Lenses with shorter focal lengths have higher distortions. However, images acquired using the plano-convex lenses with more hemispherical profile has less distortions at the periphery of the images, as shown in Figure 3.30(b). Similarly, images acquired using *in-situ* thermal cured inverted lens are compatible with other lenses. But, it has been observed that with the increase of the number of drops per lens, the imaging performance gets compromised, due to the internal reflection among the layers of the drops.

The different moldless elastomer lens manufacturing processes discussed in this chapter have their own pros and cons. In Table 3-2 we articulated some performance measures of the methods based on the mentioned parameters. We discussed parameters such as complexity, precision and expertise required to demonstrate the differences among the processes. Precision of the processes are mainly about the achievable precision for the droplet volumes. Complexity of the processes are in relation to the required resources and procedure. Whereas, expertise required are more focused on the DIY nature of the processes. These terms are loosely defined and are quantitative over certain empirical observations. The rightmost column discusses about a lens-making process that is out of the scope for this thesis, however, as the lenses have been used for imaging experimentation, the process parameters have been articulated in this table. The process can be found in [152].

3.6. Contributions

The manufacturing processes and characterizations discussed here are a team effort of a group of students working in the lab, under the supervision of Dr. Woei Ming Lee. Unless otherwise mentioned, this is a primary work of the proposed thesis. The passive droplet dispenser has been modelled and iterated by Rachel Watkins, Honours graduate. The Shack Hartmann sensor related experiments and data have been done by Zijian Cen, Honours graduate. The surface roughness related experiments and data have also been done by Zijian Cen, Honours graduate.

3.7. Chapter Summary

In this chapter, we have discussed about various moldless lenses. We have particularly offered a set of passive droplet dispenser that can be used to generate macro-droplets of PDMS on-demand. This process offers abundant droplet generation at low-cost and minimal operator training. The cured droplets can perform as optical lenses of high quality and can be used to develop compact, low-cost, portable imaging systems. The performance of the lenses has been demonstrated through imaging experiments. Also, the characteristics of the lenses have been observed using laboratory based optical techniques. Another lens-making approach introduced in this thesis is a fast way of rapidly manufacturing plano-convex moldless lenses. We compared the performances of various moldless lenses.

CHAPTER 4

INTEGRATED IMAGING SYSTEM DESIGN

Optical imaging system is a combination of multiple components – such as an object/sample to image, a sensor (CCD/CMOS) where lights can be recorded, preferably in digital format, a display that will be able to provide visual feedback to the user, a source of illumination of any kind, and preferably optical lenses for the sake of achieving higher spatial/axial resolution. The mentioned components can vary depending on the design goals and requirements of the system. While we mentioned the goal of this thesis is to focus on compact imaging system, in this chapter we intend to deliver the concept of integrated imaging systems. The necessary components for high-resolution imaging have been combined in an integrated approach to serve the purpose of macroscopic-microscopic imaging, either in a decoupled manner or off-shelf standalone manner. In both the circumstances key design goals were to keep the footprint smaller and compact, at low-cost with high quality imaging. Motivations for these designs, challenges and deliverables will be discussed in the following sections of this chapter. Figure 4.1 shows a conceptual diagram of components that a high-quality imaging system can contain.

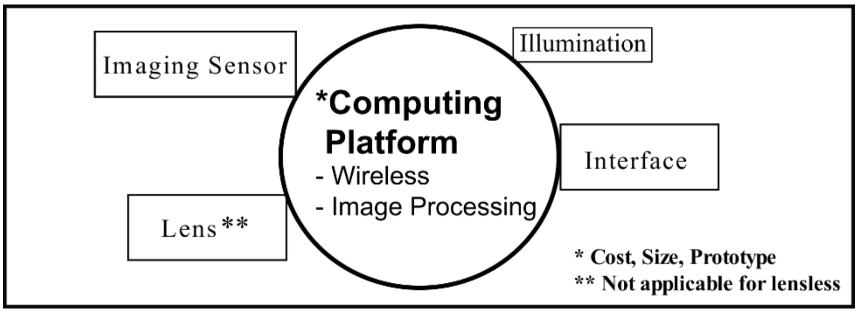

Figure 4:1: Schematic of the modules required for compact high resolution imaging. A computing platform or processor can offer on-field image processing, optical lenses for allowing high resolution imaging, imaging sensor to capture

4.1. Scopes for portable integrated imaging systems

Low-cost portable imaging systems have been used since the evolution of early portable telescope by Hans and Zacharias Janssen in 1590 where they supposedly used a pair of biconvex lenses with achieved magnification of (<10x) [153]. Later, early compound microscopes were developed by Antoni van Leeuwenhoek in late 16th century where he could achieve portable handheld microscopes providing 70x – 266x magnifications reaching resolution up to 1 µm. Then in the following 400 years optical microscopes have evolved to be better and complex, heavy, costly instruments which have evolved to become high performance instruments. However, over the last century quite a few innovations have been done in the field of microscope development where the aim was to develop portable, simple, compact low-cost microscopes in order to support the high demand of microscopic imaging in research, education and industry. These microscopes could be application specific, for example to diagnose skin cancer, [154] or for low-cost tuberculosis screening [33], or fingerprint scanner [155].

On the other hand, wearable technology is an emerging field of technology where technology meets with human gesture. Starting from smartwatches to smart clothing, wearable devices are aiding human interaction with the environment. The goal of these advancements is to attach technology with human body to enhance human-environment interfacing. The advancements of miniature LEDs and imaging sensors prompted the advent of smartphone microscopes and other portable microscopic systems.

4.1.1. Applications

There are needs for portable, compact imaging systems for high resolution imaging especially for digital pathology where a slide for diagnosis can be fully scanned at high resolution [156]. Moreover, for education in medical industry teaching pathology using traditional microscopes is expensive and a rise in virtual pathology has been observed to provide pathology education at low-cost [157]. Or, an *in-situ* imaging system inside an incubator could be of great interest for observing biological cells [32]. The other avenue for portable field microscopes could be to image irregular samples where the conventional portable microscopes would not provide convenient solution due to the structure of the microscope being fixed in a pre-defined manner, and the components are coupled. Also, for research at low-cost in schools, colleges it could be useful to have standalone microscopes, at low-cost and smaller footprint compared to traditional bulky microscopes.

4.1.2. Challenges

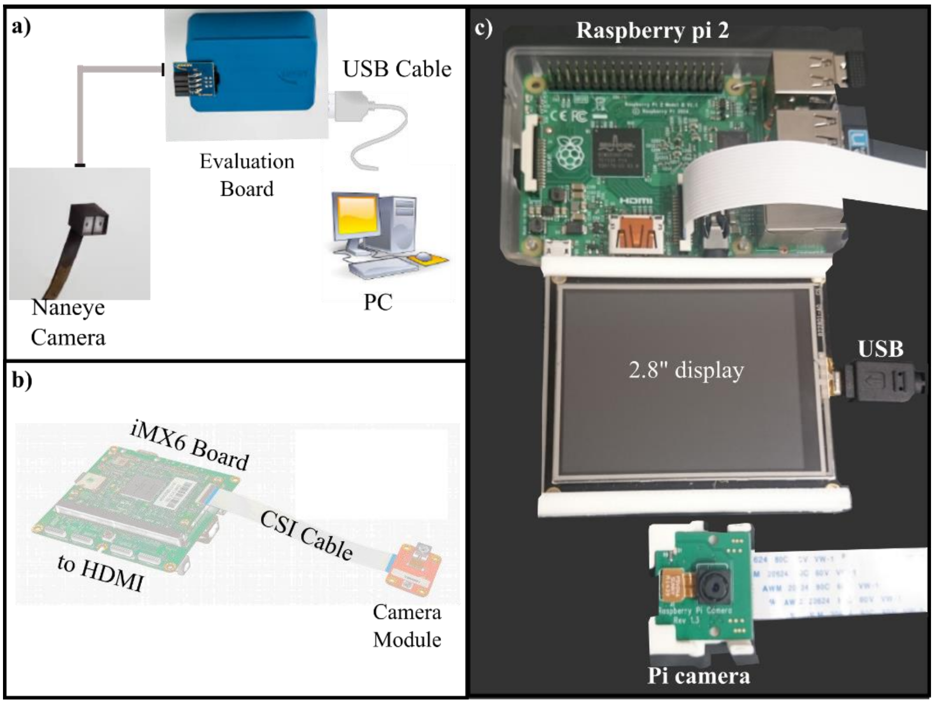

Figure 4:2: Different available imaging options for compact imaging. a) The smallest camera module in the market Naneye and required components for imaging. Scalebar indicates 1 mm. b) iMX6 board for image processing that works with commercial webcam but there is no display. c) Components of proposed, portable imaging system that includes an image processor, camera and a 2.8-inch (50 mm × 70 mm) touch screen display.

The design of portable microscopes is posed with challenges of multiple facets like, i) choice of low-resource setting, ii) choice of quality optics at low cost, low dimension, iii) choice of imaging sensor that can be used for low footprint imaging but at high quality,

iv) choice of display and v) choice of image processing unit. In Figure 4.2 we show a comparison among various available imaging systems that could be used for compact high quality imaging.

Figure 4.2(a) shows the smallest available camera in the market of size 1 mm × 1mm, with a pixel resolution of 3 µm. The camera module requires an evaluation board to work and also another computer for display. Figure 4.2(b) shows an image processing board known as iMX6, of dimensions, 70 mm × 40 mm, which is a quadcore, 1.2 GHz processor. This processor works with standard webcams for imaging. But requires a computer to provide display option for user. In order to choose a suitable camera, processor and display, the proposed compact imaging systems, the components shown in Figure 4.2(c) have been chosen, that can be used as a standalone imaging system or with the components being decoupled if needed.

4.2. Thimble imaging system

In this proposed imaging system, we have attempted to achieve an imaging system, specifically to entertain a request from a Plant Pathologist, who has been a part of Plant Biosecurity Cooperative Research Centre (PBCRC), and the project was funded by PBCRC. The request was to design a portable microscope that could be, i) used for macroscopic – microscopic imaging in a plant field, ii) that could be used to look under the leaves of a plant with visual and tactile feedbacks. Plant leaf diseases are important for agriculture economy which is most commonly observed through naked eyes of experts, whereas reliable imaging on-field is beneficial for proper diagnosis [158, 159]. Using images for phenotyping of plant diseases helps observing plant diseases over long period, consequently improving plant resistances and improving growth [160]

The design of the proposed imaging system was guided by the above design goals but was not tightly bound. Hence, we explored option of developing a low-cost, portable, compact, imaging system, which can be simple to use, and allowing freedom of movement for the user.

In Figure 4.3 we articulated a set of commercial/research applications of wearable technology. From commercial smart clothing and UV patch, as shown in Figure 4.3(a) and 4.3(b), through to new forms of wearable vision based devices such as Finger-reader (Figure 4.3(c) for visual impaired individuals, there has been an exposition of wearable devices intended to enhance human-environment interfacing. Figure 4.3(d) is the proposed thimble imaging system that can offer decoupled imaging system.

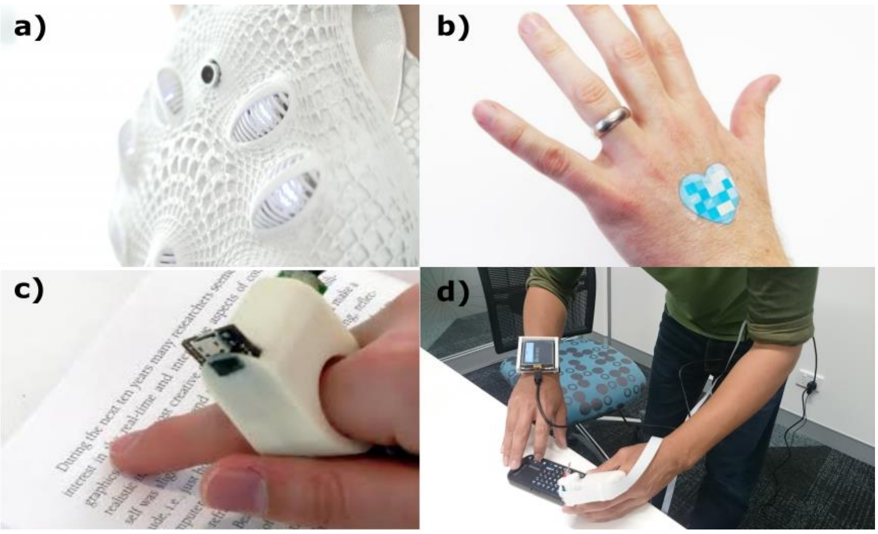

Figure 4:3: Wearable technologies. a) Synapse smart dress which can detect mood of the person based on heat sensors. b) UV patch designed by L'oreal to detect UV of the surrounding weather using sensors and a smartphone. c) FingerReader to aid blind people in reading texts d) Thimble imaging system designed for this work.

Wearable computing devices, *e.g.* google glasses, smart watch, embodies the new human design frontier, where technology interfaces seamlessly with human gestures. During examination of any subject in the field (clinic, surgery, agriculture, field survey, water collection), our sensory peripherals (touch and vision) often go hand-in-hand. The sensitivity and manoeuvrability of the human fingers are guided with tight distribution of biological nerve cells, which performs fine motor manipulation over a range of complex surfaces that is often out of sight. Our sight (or naked vision), on the other hand, is generally restricted to line of sight that is ill-suited to view around corner. Hence, conventional imaging methods are often resort to complex light guide designs (periscope, endoscopes etc.) to navigate over obstructed surfaces. Using modular design strategies, we constructed a prototype miniature microscope system that is incorporated onto a wearable fixture (thimble). This unique platform allows users to manoeuvre around a sample and take high resolution microscopic images. In this work, we provide an exposition of methods to achieve a thimble microscopy; with the thimble design, integration of miniature camera and liquid crystal display.

4.2.1. Design motivation

The leading design goal for the thimble imaging system was to provide an imaging system with decoupled components to improve on-field imaging experience with high quality imaging. Furthermore, motivation behind a thimble imaging system was to design a structure which is wearable and can be used on finger to maneuver over samples especially samples which cannot be conveniently brought into lab environment, such as, leaves of plants in a field. The reason the index finger was chosen because of the range of motion and dexterity the index finger provides.

The following is a summary of design goals, i) a decoupled imaging system with the options of microscopic imaging, having a display at a convenient location for the user to have visual feedback of the sample, while the camera “looking at the sample” ii) compact and wearable, iii) can capture macroscopic to microscopic images, with the option to take videos, iv) maneuver over objects of irregular shape or not on the line of sight, v) as the system has to look at samples under plant leaves, index finger was chosen for imaging tool because it has always shown to be highly dexterous.

4.2.2. Design optimization for thimble parts

The choice of camera was most important while attempting to develop an imaging system for the purpose of imaging under the leaves of a plant on field. The limitation was the size of the camera we are looking at, with an on-field image processor, and also that can attach a display for visual feedback. After choosing the raspberry pi camera (24 mm × 23 mm × 9 mm) for smaller size at low cost (current module v2 costs ~$29.95 USD) it was important to design the structure of the imaging system.

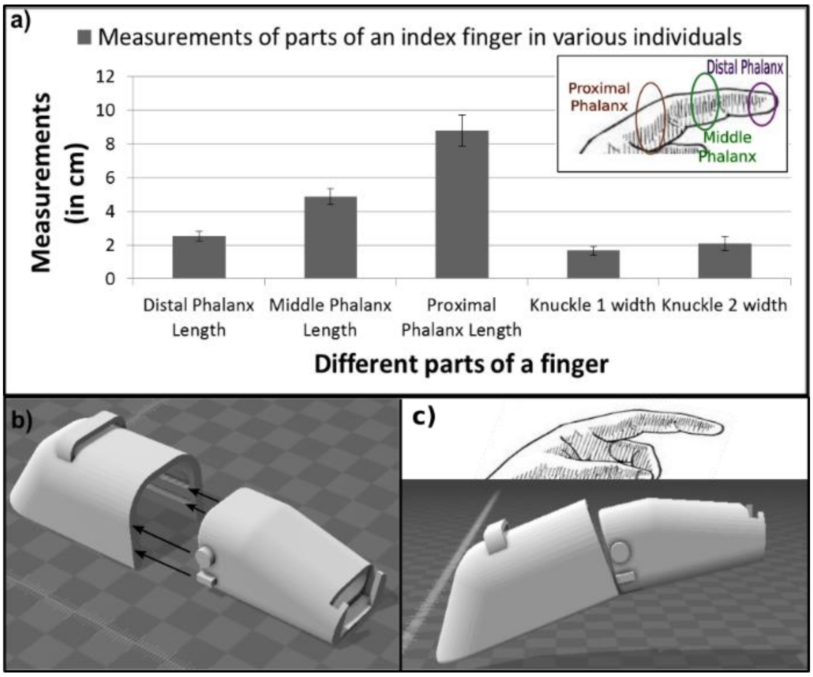

Figure 4:4: Thimble measurement for designing 3D printed thimble support. a) Different parts of index finger, with measurements of finger data from a population of 5 volunteers. b-c) The thimble design showing mechanical sliding option.

In order to hold the camera (weight about 3 g) for imaging at a sample then we opted to look for 3D printed support. We opted to design a thimble imaging system that would fit on the index finger of majority of people. It was important to find a suitable 3D printed support that would be able to hold the camera and would be comfortable for the user. Before designing a 3D printed fixture for the index finger a study has been conducted of the size of various parts of index finger over a range of population. An index finger, scientifically known as, *Digitus Secundus Manus* comprises of three parts (like other fingers), as there are 3 bones that make up a finger. The bones of the fingers, scientifically known as carpals are known as phalanges, as shown in Figure 4.4(a), where the tip segment is known as distal phalange, the middle one is middle phalange, and the one closer to the body is known as proximal phalange.

The length and circumference of the phalanges can vary among different individuals. Hence, the design optimization involved, i) finding a design to support pi camera at the tip of the index finger, ii) design iteration for the 3D printed to support to fit a range of population.

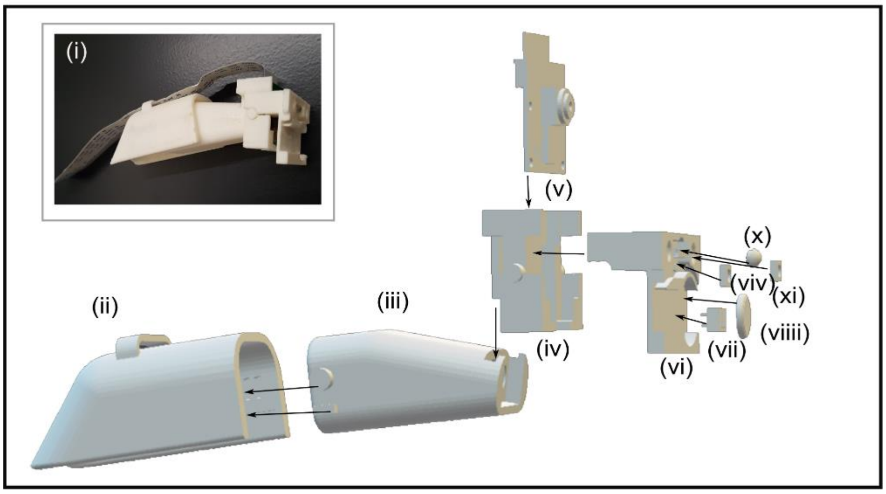

Figure 4:5: Thimble imaging prototype and components. i) Printed side-view of the thimble design prototype with camera and an optical lens attached, ii) proximal brace, iii) front brace, iv) back holder for the raspberry pi camera, v) The 3D model of the raspberry pi camera, vi) front holder of the camera that has the option to support optical lens and illumination, vii) a switch to control illumination, viii) a coin battery to supply power for the illumination, ix, xi) Two neopixel LEDs (5mm × 5mm) with integrated control, and x) A moldless lens for magnification.

Figure 4.4(a) summarizes the measurement data. A total of 5 volunteers has been used for this graph. The length measurements of different parts of the finger has been averaged and shown with an error bar. It is worth noticeable that the distal phalange has smaller variation whereas the proximal phalange has larger variation. In Figure 4.4(b-c) we have shown the 3D printed fixture which contains two parts (we will use front brace and proximal brace for the two parts respectively) and is wearable on index finger of most people. There have been multiple iterations (9 iterations) of the 3D printed designs.

The amount of comfort of the user was a design goal at this stage, so the front brace design has been optimized to a rather curved shape, so that it nuzzles the finger of the user. Also, the design optimization involved the attachment of the raspberry pi camera at the tip of the 3D printed front brace. The two parts were designed with the option for mechanical sliding that enables the front brace to slide through the proximal brace so that the design is more robust and usable for various users.

4.2.3. Imaging system prototype design

The 3D printed thimble design and the camera holder design were co-designed so that the brace can actually hold the camera while having successful capability of being used on an index finger. For the 3D printing, an UP mini printer (shown in Chapter 2) and ABS material has been used. Moreover, it is important to allow the imaging system to have capabilities of high resolution imaging. For that reason, the camera holder was segmented into two parts that can be mechanically attached to each other. The back part supported the back side of the camera. Whereas, the front part of the camera holder was designed to support optical alignment of an optical lens with the raspberry pi camera sensor and support for illumination. Figure 4.5 shows the thimble prototype imaging system. In Figure 4.5(i) we can see the overall thimble imaging system. In the exploded view (in Figure 4.5(ii) – (xi)) we can see the parts of the thimble prototype.

In the exploded view we can see the different 3D printed parts that can attach the thimble design to the pi camera at the tip, with the option to attach a moldless lens.

4.2.4. Choice of optics

The main purpose of the proposed thimble imaging system was to image samples under the leaves of a plant. For this reason, there has been a requirement of the level of magnification achieved from the system. Although, plant diseases mostly range in the macroscopic level, it is important for analysis to enhance the images with an optical lens so that further details of the disease can be observed. To support this idea, while maintaining the dimension of the thimble imaging system, we chose to use passive droplet lenses for imaging. Passive droplet lenses have been discussed in chapter 3. The base diameters of the lenses are same, 3 mm, and are suitable for imaging with the raspberry pi camera which has a CMOS sensor of 3.76 mm × 2.74 mm area. The imaging performance of the moldless passive droplet lenses have been demonstrated in chapter 3. So, to have a low-cost, compact, portable imaging system, we decided to use moldless lenses for this imaging system.

4.2.5. Choice of processor

Any imaging system requires a camera/photodetector and can contain an image processor. For the thimble imaging system, the consideration was carefully made based on numerous factors such as size, on-spot processing capability and cost. As shown earlier, in Figure 4.2, Naneye requires to be connected to a computer for visual feedback. Naneye camera costs ~US$1550 with resolution of 250 × 250. High-speed image processor IMX6 requires to be connected to a commercial webcam for the purpose of capturing images. And there is no visual feedback. It costs ~US$115.

The processor used for the proposed design has been Raspberry pi. Considering the cost and size of the overall system Raspberry Pi has been chosen. The attachment of a 2.8″ LCD USB display makes the whole system compact and flexible to use. The following were primary considerations during the selection of a camera and processor, i) self-contained programming and imaging unit, ii) low-cost (~ US$35), and compact and high resolution camera (5 - 8 MP) and with a size of 25 mm × 24 mm. Specifications of the Raspberry pi 2 model B have been outlined in Figure 4.6.

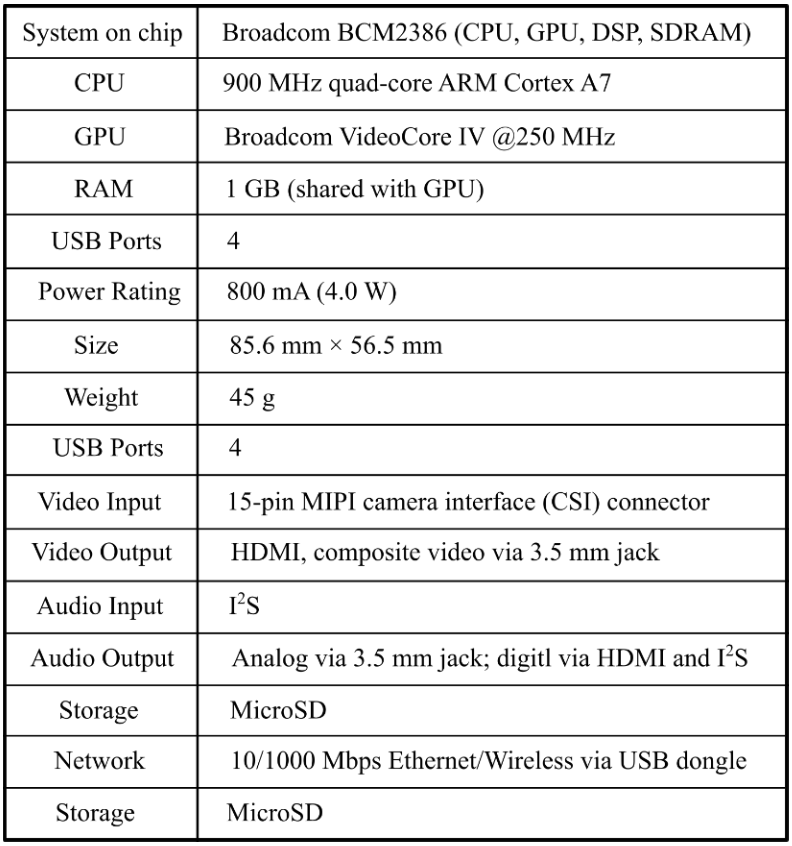

System on chip	Broadcom BCM2386 (CPU, GPU, DSP, SDRAM)
CPU	900 MHz quad-core ARM Cortex A7
GPU	Broadcom VideoCore IV @250 MHz
RAM	1 GB (shared with GPU)
USB Ports	4
Power Rating	800 mA (4.0 W)
Size	85.6 mm × 56.5 mm
Weight	45 g
USB Ports	4
Video Input	15-pin MIPI camera interface (CSI) connector
Video Output	HDMI, composite video via 3.5 mm jack
Audio Input	I^2S
Audio Output	Analog via 3.5 mm jack; digitl via HDMI and I^2S
Storage	MicroSD
Network	10/1000 Mbps Ethernet/Wireless via USB dongle
Storage	MicroSD

Figure 4:6: Raspberry pi 2 model B specifications. For majority of this research Raspberry pi 2 model B has been used for imaging.

Linux is the most popular choice of operating system for raspberry pi due to the open-source environment available for Linux. The OS most popularly used for raspberry pi is known as Raspbian that comes with 35,000+ prebuilt packages that make it easily installable and compact. Moreover, image processing using openCV library on raspberry pi is a convenient tool for any imaging especially for the field of microscopic imaging. OpenCV stands for “Open Source Computer Vision” which is a collection of library and is available in low-level programming languages like python and c++ for image processing [161]. It provides similar features like MATLAB but is faster and the libraries are available for free. It is also possible to use GNU-Octave on raspberry pi which is based on MATLAB functionalities.

4.2.6. Portable, compact system

In order for the thimble prototype to be really useful on-field with a self-contained imaging system, we chose to add a display unit for the system. Just like any microscope needs visual feedback, which could be eyepiece or a computer monitor, our imaging system also contains a display. As the primary challenge was to design an imaging system that could be beneficial for plant imaging on-field, where the use of large, bulky devices would not be possible, we decided to choose a small 2.8-inch touchscreen display which can be worn on the wrist with a simple 3D printed support. In order to show that the system is convenient compared to an image processor module that would require an additional device to run on-field, we have demonstrated the use of both the imaging systems in an outdoor environment, as shown in Figure 4.6.

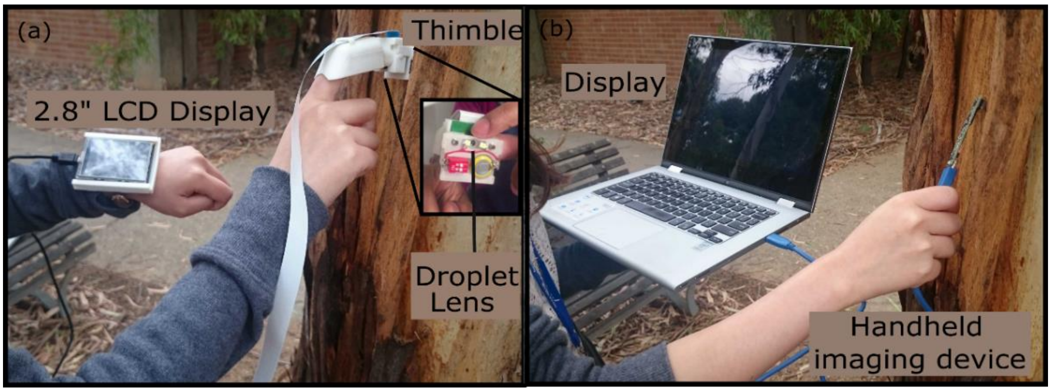

Figure 4:7: Portable handheld imaging systems for outdoor imaging. a) Proposed thimble prototype with a camera and optical lens for microscopic imaging (shown inset), all decoupled. b) An image processor that can be handheld for imaging but requires a computer to provide visual feedback.

In Figure 4.7(a) we have shown the proposed portable imaging system for on-field plant imaging. It contains, a wearable display, a thimble prototype for image acquisition (inset shows the lens, and circuitry for illumination). The processor has not been shown here. But that can be worn around waist, or on arm as armband while on-field image processing. Figure 4.7(b) shows an iMX6 image processor that can be handheld for imaging. This powerful image processor is a quadcore processor but does not have any option for visual feedback for the user. Hence, it requires to be attached to a computer to provide display, making on-field imaging inconvenient.

4.2.7. Imaging performance

The thimble imaging system with illumination is capable of providing reflection-based images of the sample. In Figure 4.8 we have articulated a range of images taken using the thimble prototype.

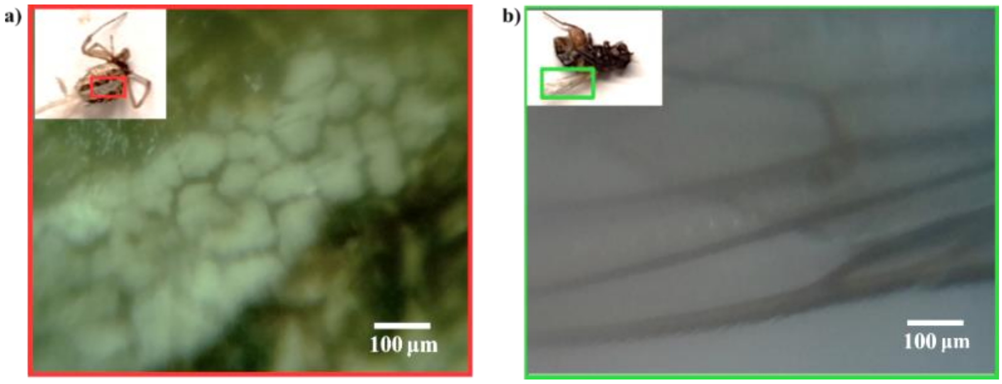

Figure 4:8: Reflection based imaging using the thimble prototype. a) Image acquired from the back of a male redback spider, *Latrodectus hasseltii*, of body length 3 mm. b) Wing of a common house fly, *Musca domestica*.

The imaging performance of the proposed thimble system is limited by the amount of light in the environment. The working distance between the sample and the imaging unit depends on the focal length of the droplet lens used, ranging between 4 mm – 20 mm. This can be overcome by the use of on-site image processing capability of the raspberry pi (brightness, contrast, saturation). This has been previously mentioned that it is possible to run python or c++ image processing libraries on raspberry pi that are available for free which is economical for low-cost solutions.

In Figure 4.9(a) an image of a *Lytechinus Pictus* (sea urchin) has been acquired using the thimble imaging system where three *globiferus pedicellariae* are clearly identifiable.

SimpleCV open-source library image processing techniques (Figure 4.9(b) –(c)) have been used to detect the sea urchin and measure the area and location of the sea urchin this could be used for plant disease diagnostics by detecting the shape, size and area of an image.

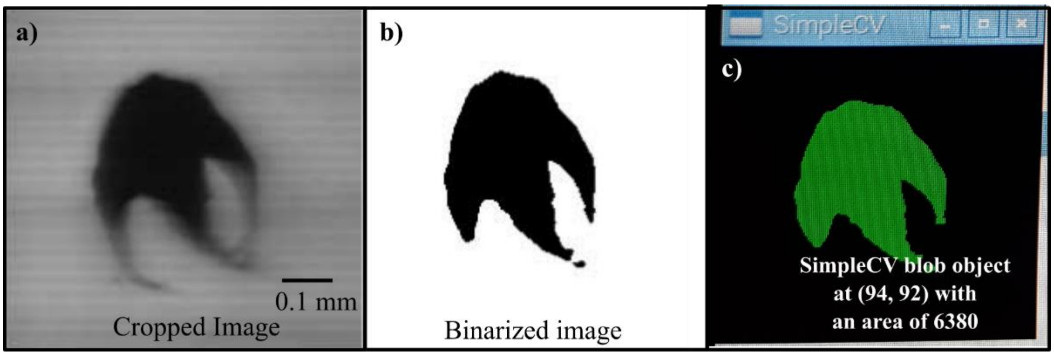

Figure 4:9: A sea urchin imaged using the thimble imaging system and in-situ image processing done on raspberry pi. a) A brightfield image of a sea urchin. b) Binarized image, c) Blob area and location detection in terms of pixels.

Alternatively, the thimble imaging system can be used for transmission-based illumination, as shown in Figure 4.10. In Figure 4.10(a) we can see an USAF 1951 negative resolution card has been imaged using the thimble imaging system with an imaging resolution of almost, 3.1 µm (Group 7 element 3). A young Australian cockroach, *Periplaneta australasiae*, has been imaged using the thimble imaging system (shown in Figure 4.10(b)) where the bristles of the antenna can be resolved.

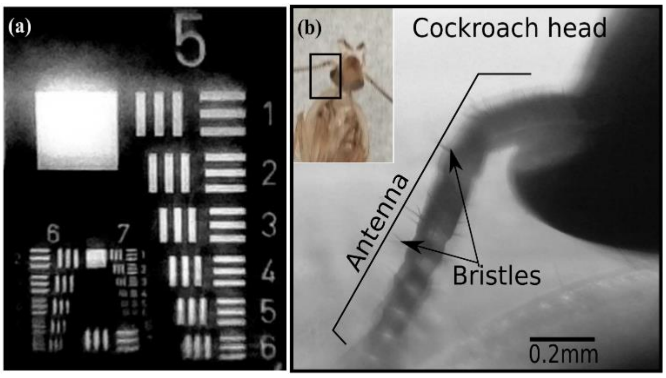

Figure 4:10: Transmission based imaging using the thimble imaging system. a) USAF target card image with achieved resolution of 3.1 µm. b) Parts of a cockroach antenna and bristles.

It is worth noticeable that although the thimble imaging system has been designed for plant pathology specifically, it is usable for other fields wherever there is a requirement for imaging irregular samples or line of sight compromised.

4.3. Portable standalone microscope

Science education for children is extremely important to equip a nation with more scientists in future. Children are capable of helping us to become a more science-literate society. In order for children to have better access to science and technology, we aimed our next portable microscope as a table-top standalone microscope which is low-cost, light-weight, and compact at the same time which has the capability to be used in classroom environment for primary to high school students.

A standalone microscope is always desirable for precise standard imaging where sample, illumination, imaging sensor, are stable and on a fixed optical path. This has been a common property of the traditional microscopes, for which they have been developed to provide brightfield images. But the size, cost and complexity of the traditional microscopes make them unattractive for mass usage. For educational purposes at affordable cost in high schools it is imperative to provide alternative imaging methods to ensure science education is reaching desired quality and breadth. Where grants are tight, research is crucial but equipment is expensive, to spread science education to mass, Jodo Gyan a small non-profit organization based in the capital of India, New Delhi, initiated a project, where they made ~$4 USD microscopes out of bamboo [65]. These microscopes with capacity of magnification of 20x, have been vastly used in a remote village in Eastern India where approximately 2500 microscopes have been made due to the popular demand. Another example of portable, low-cost microscope is, “Foldscope”, which implements the idea of origami to build a microscope which gained popularity to offer low-cost microscopes at schools [162].

4.3.1. Design goals:

In order to deliver a quality portable microscope as standalone microscope, we aimed to use 3D printed structures as prototyping using 3D printed substrates has been found to be cost effective and comes with the flexibility of replicability. Moreover, designing prototypes using 3D printed substrates allows for decoupling of the components, that can be assembled together to perform as a whole system. This helps understanding the scientific concepts behind the working principles of the design. Here, we outline the design goals for this imaging system in Figure 4.11.

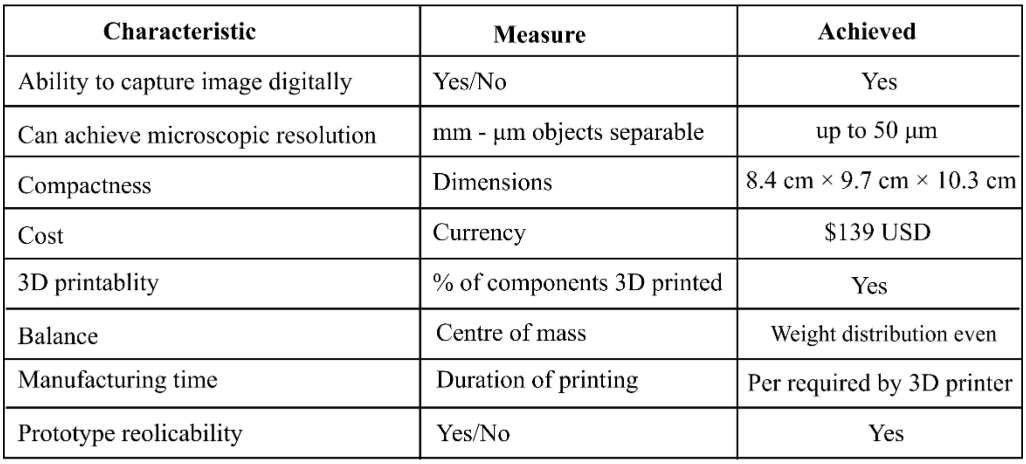

Characteristic	**Measure**	**Achieved**
Ability to capture image digitally	Yes/No	Yes
Can achieve microscopic resolution	mm - µm objects separable	up to 50 µm
Compactness	Dimensions	8.4 cm × 9.7 cm × 10.3 cm
Cost	Currency	$139 USD
3D printablity	% of components 3D printed	Yes
Balance	Centre of mass	Weight distribution even
Manufacturing time	Duration of printing	Per required by 3D printer
Prototype reolicability	Yes/No	Yes

Figure 4:11: Design goals set for the project on “Standalone microscope”. The design goals primarily involved, use of 3D printed parts to ensure open-source access of the parts, then cost and compactness.

Due to the successful use of raspberry pi as a processor and the advantage of a camera providing overall compactness, we have chosen raspberry pi for this imaging system as well. The choice of optics (low-cost moldless elastomer droplet lenses), processor (raspberry pi 2 model B), camera (raspberry pi camera) has been constant for the applications we have attempted for this work.

4.3.2. Design optimization:

In order for the design to perform as a whole imaging system with the capabilities of a standalone microscope, it was necessary to feed the design with the options, i) Source of illumination (shown in Figure 4.12, two alternative options), ii) Translational stage to adjust sample height (z axis) for focusing, iii) Translational stage to adjust sample ROI (region of interest), x-y axis, iv) A display to screen to provide visual feedback To achieve these requirements, the design had to go through several iterations to reach to a standalone microscope.

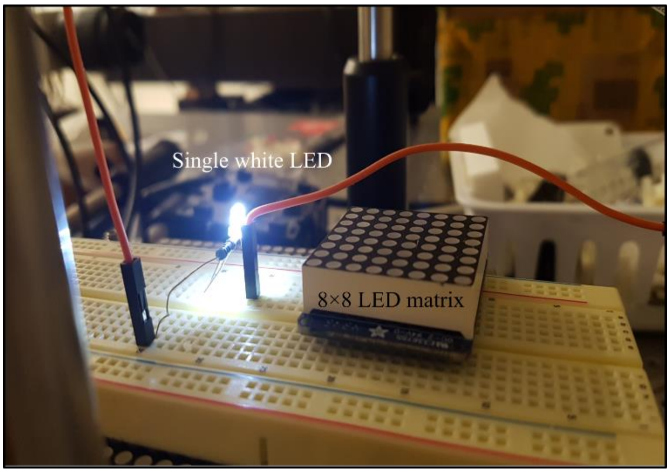

Figure 4:12: Illumination options for the proposed prototype. A single white LED offers simplicity and single brightfield imaging. Whereas, an 8×8 RGB LED matrix offers different angular illumination and spectral imaging options.

4.3.3. Prototype of the microscope:

A total of 11 parts have been designed using Solidworks to build the prototype of the microscope. The different parts were printed using UP mini printer (shown in Chapter 2) and ABS material. The design has been decoupled into, a display mount, as shown in Figure 4.13(a), that can hold a 2.8” USB display that has been discussed earlier in this chapter. Then, a front cover for raspberry pi 2 model B processor that has the capability to support the LCD display holder, alongside providing safe operating environment for user and protection for the processor, as shown in Figure 4.13(b). In Figure 4.13(c) the back cover for raspberry pi 2 model B processor has been shown, this also adds to the stability of the standalone microscope.

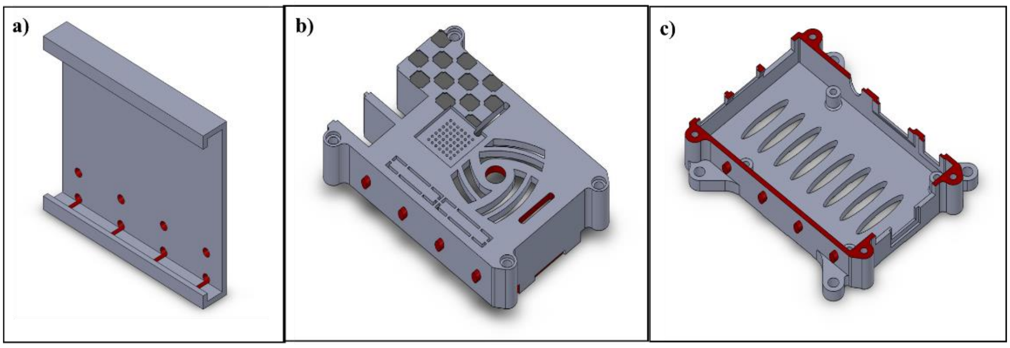

Figure 4:13: Three parts for the standalone microscope. i) A cover to hold the 2.8-inch LCD display, ii) Front cover for the raspberry pi processor, iii) Back cover for the processor.

The next parts of the microscope design are used for holding the pi camera with the option to provide optical alignment of the objective lens (a low-cost elastomer droplet lens), along with supporting the camera to position for imaging purpose. Figure 4.14(a) shows the front cover that provides an option to attach a lens and in Figure 4.14(b) we can see the back cover for the raspberry pi camera. The covers also ensure safety for user and the device.

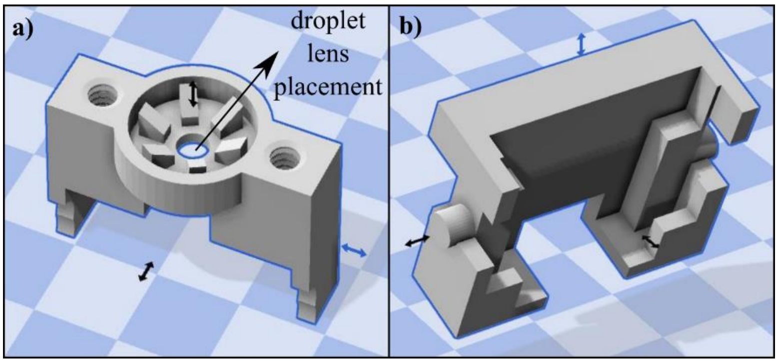

Figure 4:14: Support for optical alignment between camera and objective lens. a) Front cover for raspberry pi camera. b) Back cover for the raspberry pi camera/CMOS.

For the next parts, the design was focused into vertical and axial actuation of the system to allow image plane adjustment and to find a region of interest on the sample/object. In Figure 4.15 the complete design for sample holder with the option for x-y translation, or panning, has been shown. The mount that attaches with the raspberry pi cover (shown in Figure 4.13) and holds the sample stage, can be seen in Figure 4.15(a) and 4.15(b) (top-down view). In Figure 4.15(c)-(d) we can see the x-y stage, and the stage attached with the mount, respectively. In Figure 4.16€ the sample holder can be seen. A microscope glass slide (76 mm × 26 mm × 1.2 mm) inserted into the sample holder and the mount has been demonstrated in Figure 4.15(f).

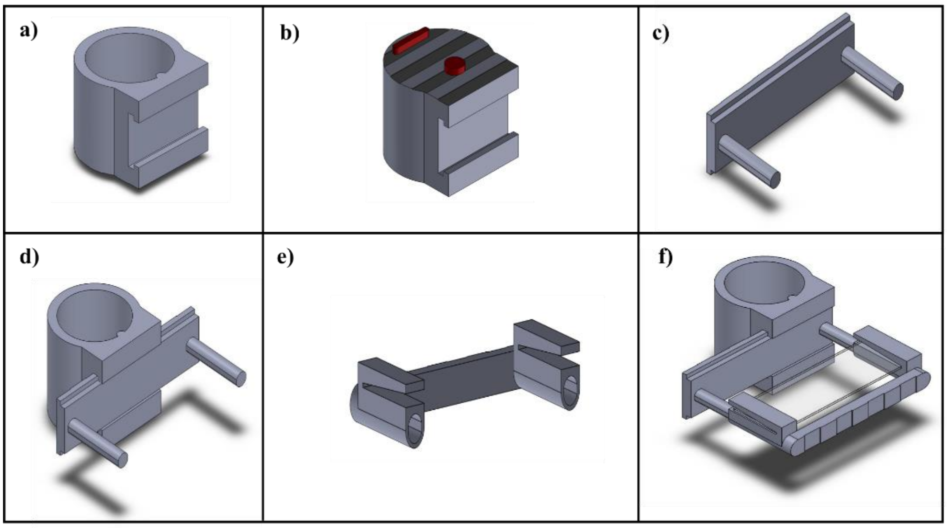

Figure 4:15: X-Y translational stage design and demonstration. a) Mount, bottom-up view. b) Mount, top-down view, c) x-y stage, d) the mount and the stage attached, e) The sample holder, f) Demonstration of the x-y stage with a microscope glass slide.

The next design step took several iterations to find an optimum solution for vertical alignment/actuation or image plane adjustment. The final design for z-alignment can be seen in Figure 4.16. A pillar shown in Figure 4.16(a) has been used to perform as the backbone for the z-alignment. A helix engraving has been used to rotate the collar (shown in Figure 4.16b) around the pillar for adjusting z-alignment, which is to focus the CMOS sensor at the focused image plane. The hemispherical anchor fits the width of the helical engraving and then rotational up-down allows z-alignment (as shown in Figure 4.16(c) - 4.16(d)). Despite using the hemispherical anchor, the collar demonstrated certain instability hence another top mount was needed to stop the collar from moving, which attaches to the back cover of the camera. The top mount has been shown in Figure 4.16(e) and the collar attached with the top mount has been shown in Figure 4.16(f).

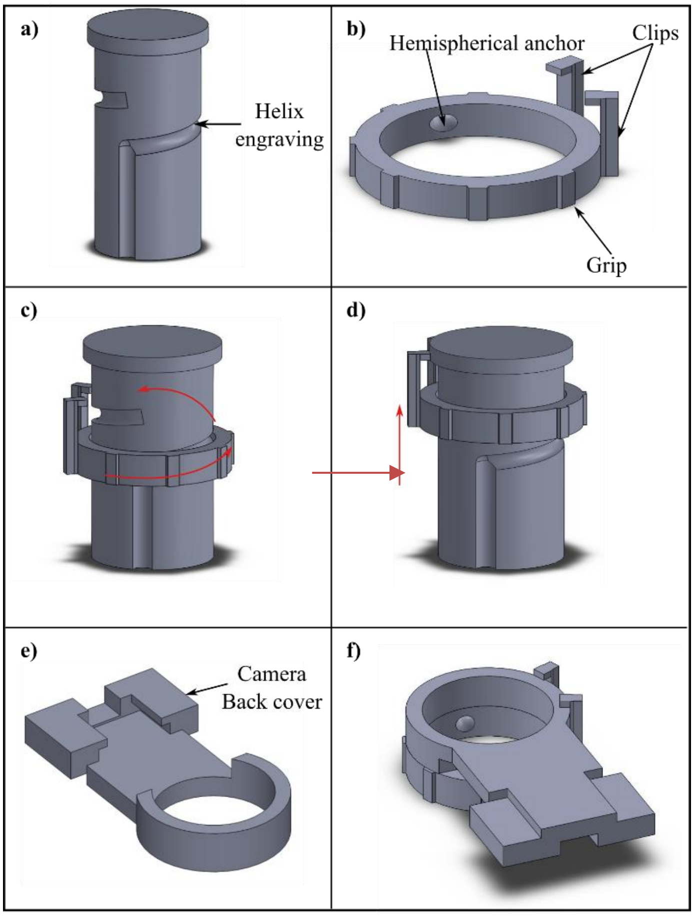

Figure 4:16: Z-axis (the axis normal to the x-y axes) alignment of the microscope for CMOS height adjustment. a) A pillar that provides the backbone support for the microscope with a helical engraving. b) A collar with clips and a hemispherical anchor, that allows for the collar to rotate and move up-down for z-alignment. c) Collar attached to the helical engraving, rotating left-right. d) Rotation causes the collar to move upwards. e) Top mount for the z-alignment control for stability attached with the back cover for the CMOS (bottom-up view). f) Collar and the mount attached.

While the proposed standalone/table-top imaging system design requires multiple components, they are easy to assemble as there are slides and fixtures for the parts to be attached together. The overall design model once assembled together can be seen in Figure 4.17(a). In Figure 4.17(b) the 3D printed prototype has been shown. Moreover, once the design files are available, replication of the model requires the time to print out the parts. The details have been summarized in Figure 4.18.

From the details it is worth noticeable that the overall dimensions of the microscope are very compact and small, 9.7 cm × 8.4 cm × 10.3 cm.

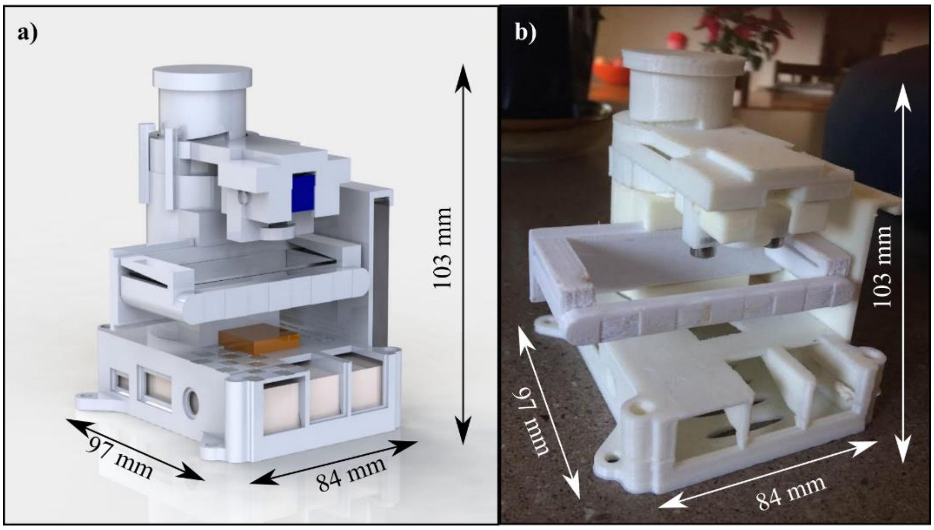

Figure 4:17: The proposed compact standalone microscope. a) The 3D model. b) The printed and assembled standalone microscope.

The design is also very lightweight of around 160 g costing ~$105 USD that includes the display, camera, processor, 3D printed parts illumination and elastomer droplet lens.

4.3.4. Imaging performance

As the design did not achieve the desired balance performance, the microscope did not perform as desired. But we were still able to capture images of biological samples as shown in Figure 4.19. The image is a tissue sample of lung cancer where the thick lung cancer cells can be observed that is a consequence of cancer.

Although the imaging performance was not found to be as desired, the microscope can still acquire images of samples for primary-elementary schools. Additionally, the design modification requires minimal effort to modify the design to offer better balance.

This proposed design was aimed to avoid any mechanical components and thus 3D printed stage translation was necessary to achieve, which the design could very well offer.

The next stage for this prototype will be to improve balance and introduce GUI (graphical user interface) so that children, school teachers can use the microscope with ease.

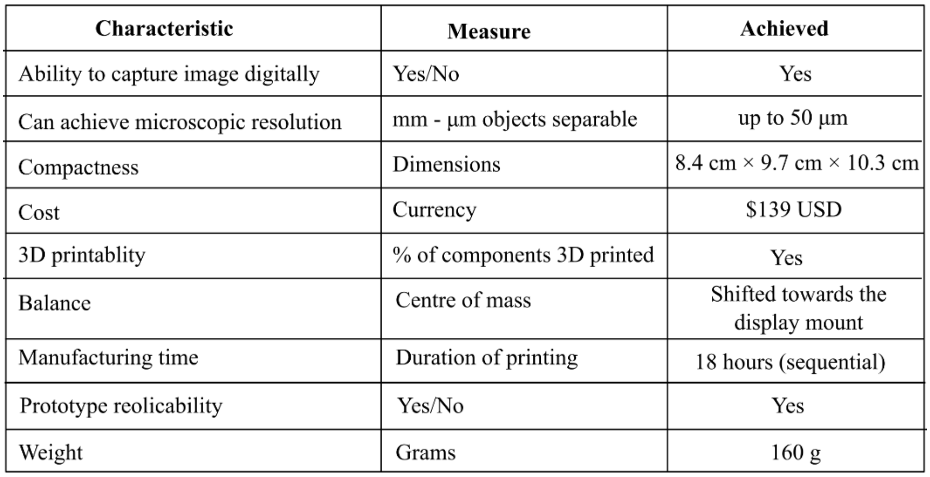

Characteristic	Measure	Achieved
Ability to capture image digitally	Yes/No	Yes
Can achieve microscopic resolution	mm - µm objects separable	up to 50 µm
Compactness	Dimensions	8.4 cm × 9.7 cm × 10.3 cm
Cost	Currency	$139 USD
3D printablity	% of components 3D printed	Yes
Balance	Centre of mass	Shifted towards the display mount
Manufacturing time	Duration of printing	18 hours (sequential)
Prototype reolicability	Yes/No	Yes
Weight	Grams	160 g

Figure 4:18: The properties of the 3D printed standalone microscope that has been achieved from the project.

4.4. Compact high resolution, high SBP imaging system

Here, we want to introduce another compact standalone microscope design. The design of the above-mentioned standalone microscope could be altered to allow a larger LED matrix (possibly with > 300 LEDs available) which would change the footprint of the microscope to about 14 cm × 14 cm × 15 cm and the weight to increase to about 250 g. The purpose of the design to add a larger LED matrix is to acquire more brightfield images of the sample using different LEDs from different angles. The motivation behind this approach is to allow synthetic scanning of the sample, without having to mechanically scan. A new imaging modality has been started in 2013 by a group from California technology where the use of synthetic scanning and later computational reconstruction on the images have been able to improve the imaging performance of a single imaging system, defeating the physical limitation of the optical lens of the system [11]. This allows for a low-resolution imaging system to computationally achieve higher SBP, higher NA over the full FOV of an image.

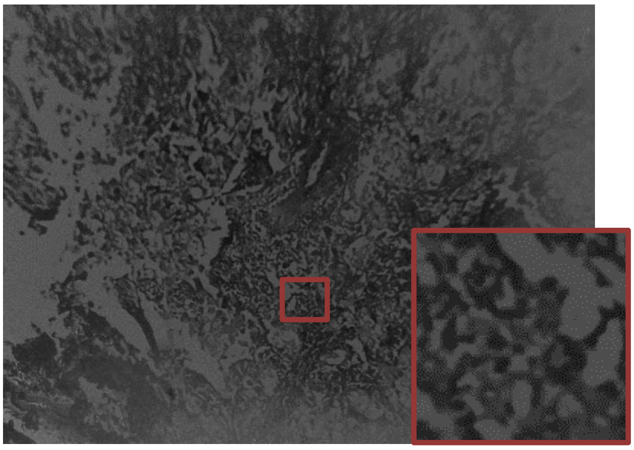

Figure 4:19: Lung cancer tissue sample imaged using the proposed standalone microscope and a cropped region shown in the red rectangle.

Now, we shall introduce the concepts of Fourier Ptychography and relevant computational techniques in Chapter 5. But here we wanted to demonstrate the idea of a small compact imaging system with capabilities beyond traditional light microscopes. This compact imaging system could be useful in incubator for imaging biological samples and live cell imaging at low-cost. This low-cost imaging system could be useful for any imaging system where light microscopes are used, with compactness and promises of higher SBP.

4.5. Contributions

The imaging systems proposed here have been developed and manufactured under the supervision of Dr. Woei Ming Lee as a part of different projects. Jaden Rubenstein, a 4th year honours R&D graduate designed the 3D printed braces of the thimble imaging system, the raspberry pi camera holder, for allowing optical alignment with an elastomer lens. The design optimization and thimble prototype were results of his hard work. The standalone microscope prototype has been designed and developed by Michael Petkovic, a 2nd year R&D student for which I was a supervisor. The design optimization and iterations were all carried out by Michael in consultation with me and our group leader.

4.6. Chapter Summary

In this chapter we offered ideas of portable, compact imaging that can achieve macroscopic-microscopic imaging. The imaging systems were built using moldless lenses to offer high-resolution imaging and the housing/infrastructure of the systems were developed solely using 3D printed substrates. Use of 3D printed design files offer easy distribution of the designs. The modular designs can be used in decentralized environment. The goal of this chapter was to offer ideas so that more people can engineer their own imaging systems. The design and performance of the systems have scopes to improve which we will discuss in future works.

CHAPTER 5

COMPUTATIONAL TECHNIQUES BASED ON FOURIER OPTICS

The need for decentralization of high performing imaging systems is salient in optical research to provide field-portable high quality imaging devices for health or other imaging needs as discussed in Chapter 1. Typically, improved performance of an imaging system relies on the optical lenses, especially for optical microscopy. In optical microscopic imaging majority of the times these performance indicators are resolution, and the space bandwidth product (SBP). Due to the fixed physical dimensions of the lenses the microscopes have been always limited in performance until recently when computational approaches have started to emerge [11, 54]. Computational microscopy finds its root in the idea of Fourier optics [163] that arises from image formation process of an optical lens. There are different optical imaging problems that have been tackled by various computational approaches, such as inverse problem [164, 165], ptychography or digital wavefront correction [166]. In this chapter we will discuss one such computational technique, namely Fourier Ptychography (FP), that has emerged recently which has reportedly been able to provide gigapixel imaging [11].

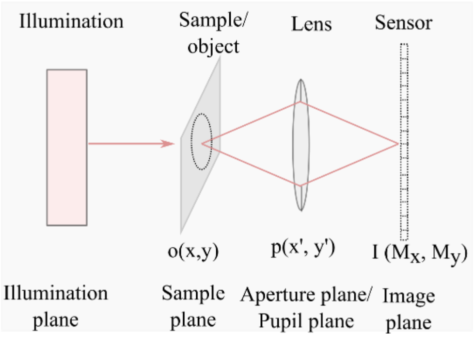

Figure 5:1: A simple imaging system. The mathematical model applicable for the majority of the thesis. In an imaging system we have an illumination plane to provide illumination, sample or object plane – sample of interest, the lens aperture plane which can be considered equivalent to the pupil plane. Finally, the image forms on the image plane. Redrawn from similar thesis [167].

FP incorporates the idea of aperture synthesis that has been used in astronomy before in microscopy to synthetically increase the aperture of the imaging system which in turn improves the resolution and SBP [168]. FP also addresses inverse problem by iteratively retrieving phase information from intensity images only. In this chapter we will introduce the concepts of mathematical manipulation of optical information, the ides of computational microscopy, such as Fourier Ptychography (FP) and the limitations of the existing FP performance on moldless lenses. The improvement of moldless lens based optical imaging systems will be discussed in Chapter 6.

5.1. Simple microscope system

Any compound microscope system involves the use of an objective lens and a tube lens to create an image of an object on the sensor/detector. However, in this work we have used a single lens-based imaging system mostly, hence we introduce a simple imaging system in Figure 5.1. Alongside, we introduce the different planes involved in microscopic imaging system.

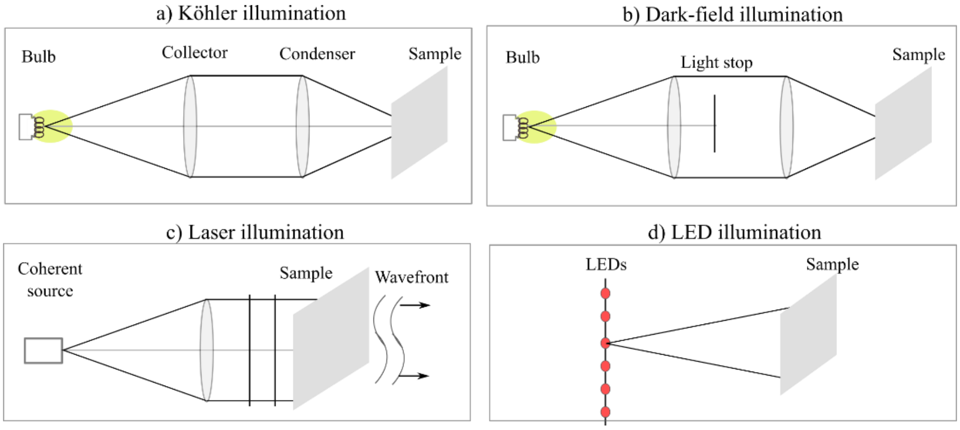

Figure 5:2: Different types of transmission-based illumination used for microscopic imaging. a) Köhler illumination is most commonly used brightfield microscope system used with incoherent illumination such as a bulb. b) If a disk is placed to block certain central portion of the light coming from the source and only the scattered light from the edges are collected by the sensor then that arrangement is known as dark-field illumination. Redrawn from similar thesis [167].

Illumination plane is the plane where the source of illumination is placed. As shown in Figure 5.2 different types of illumination are used in traditional microscopes, such as an incoherent source (bulb) in Köhler illumination, a coherent illumination source like a laser or an LED matrix providing varying angular illumination sources in a singular imaging system.

Sample plane is where the sample/object is placed, with the transmission function, $O(x,y)$ where (x, y) are the 2D spatial coordinates on the sample plane which are perpendicular to the optical axis. The light propagating through the sample then reaches the lens. The physical aperture of the lens limits the wave that can propagate further to the sensor. This wave at the aperture can be described as, $a(x',y')$, where (x′, y′) are the Fourier conjugates of the coordinates (x, y). This lens aperture has been denoted as aperture plane. For this simple imaging system this aperture plane is equivalent to the pupil plane $P(x',y')$.

This plane is actually at the Fourier conjugate of the sample and image planes [163]. The wave then terminates at the image plane where we place the sensor. Each pixel on the sensor samples the intensity of the incoming wave. The wave is the convolution of the aperture function and the sample function. Using Shannon's sampling theorem, it is possible to recover the exact intensity distribution of the incoming wave from the discrete samples recorded by the sensor.

5.2. Basic Fourier Transform

In this section, we will discuss about the concepts that lead to the use of Fourier transform in image processing. Fourier transform is a mathematical decomposition of periodic functions from time domain (or for an image from spatial domain) to the different sine/cosine components present in the function. That is, any periodic or aperiodic function can be expressed in terms of the different frequency components the function consists of. Generally, for any 2D function, it is given by the equation,

$$F(u,v)=\int_{-\infty}^{+\infty}\int_{-\infty}^{+\infty} f(x,y)e^{-j2\pi(ux+vy)}dxdy \tag{5-1}$$

And the inverse Fourier transform is given by,

$$f(x,y)=\int_{-\infty}^{+\infty}\int_{-\infty}^{+\infty} F(u,v)e^{j2\pi(ux+vy)}dudv \tag{5-2}$$

where, $f(x,y)$ is the function in the spatial domain, u and v are angular spatial frequencies and $F(u,v)$ is the function after 2D Fourier Transformation.

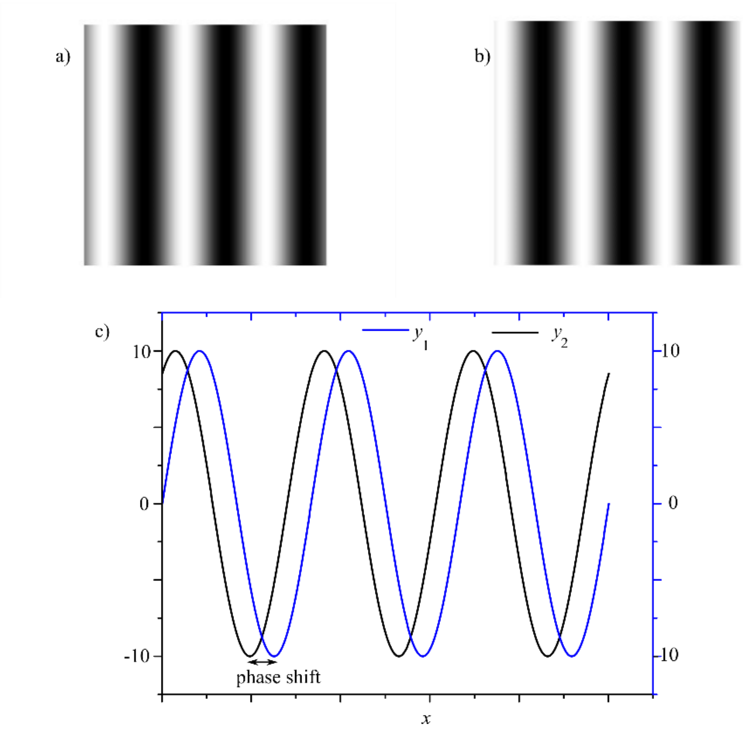

Figure 5:3: 2D sinusoidal gratings created in MATLAB to demonstrate concepts of spatial frequency, phase shift. In (a) we can see a grating corresponding to the equation, $y_1 = 10\sin(2\pi 3x)$, whereas in (b) we can see a 2D grating with a 45° shift. (c) demonstrates the phase shift with the use of 1D line plots.

Ordinarily any time/spatial domain function which is continuous consists of a large amount of data. Mathematically manipulating this information can be tedious and exhaustive. However, the information in the frequency domain condenses the information compared to the time/spatial domain information and thus the computational processing is simpler, requires less execution time and is exposed to many processing algorithms. Moreover, Fourier transform converts a complex convolution operation into a simple multiplication operation. Hence for computational optics Fourier plays an important role.

5.2.1. Numerical Fourier Transform in image processing

Fourier optics helps to transform an image in the Fourier domain and each pixel in the Fourier domain is a vector in the 2D space corresponding to the intensity information for a particular spatial frequency. The magnitude of the vector gives the intensity information whereas the position of the vector gives the phase information.

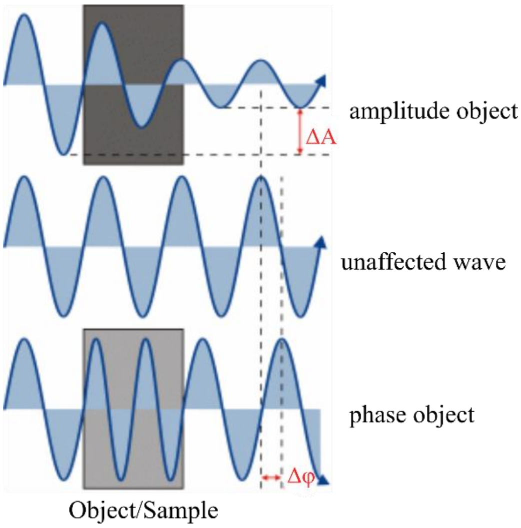

Figure 5:4: When light as a wave propagates through different samples the resulting waves alter differently depending on the sample. The amplitude of the incoming light wave changes enough through amplitude objects (ΔA) which can be detected by a detector due to sufficient contrast. However, for phase objects the amplitude does not change enough to create enough contrast. For these the phase delay information (Δφ) is of importance to create contrast [66].

When an image is transformed in the Fourier domain the transformed image encodes all information of the original image by encoding, (1) the spatial frequency of the image, (2) the magnitude and (3) the phase. The spatial frequency is the number of fringes present per distance (cycles/meter), the magnitude represents the level of contrast (difference between brightness and darkness, for example, 100% contrast means difference between pure black and pure white) present in the image and phase represents the level of shift in the image from the origin.

In Figure 5.3(a) we can see a 2D sinusoidal grating with the equation, $y_1 = 10\sin(2\pi 3x)$, meaning, spatial frequency = 3 and phase =0. Whereas, the gratings shown in Figure 5.3(b) represent the sinusoid, $y_2 = 10\sin(2\pi 3x + 45)$, has been shifted from the origin, as can be seen. The corresponding line plots for both these sinusoids have been shown in Figure 5.3(c), demonstrating the phase shift between the waves.

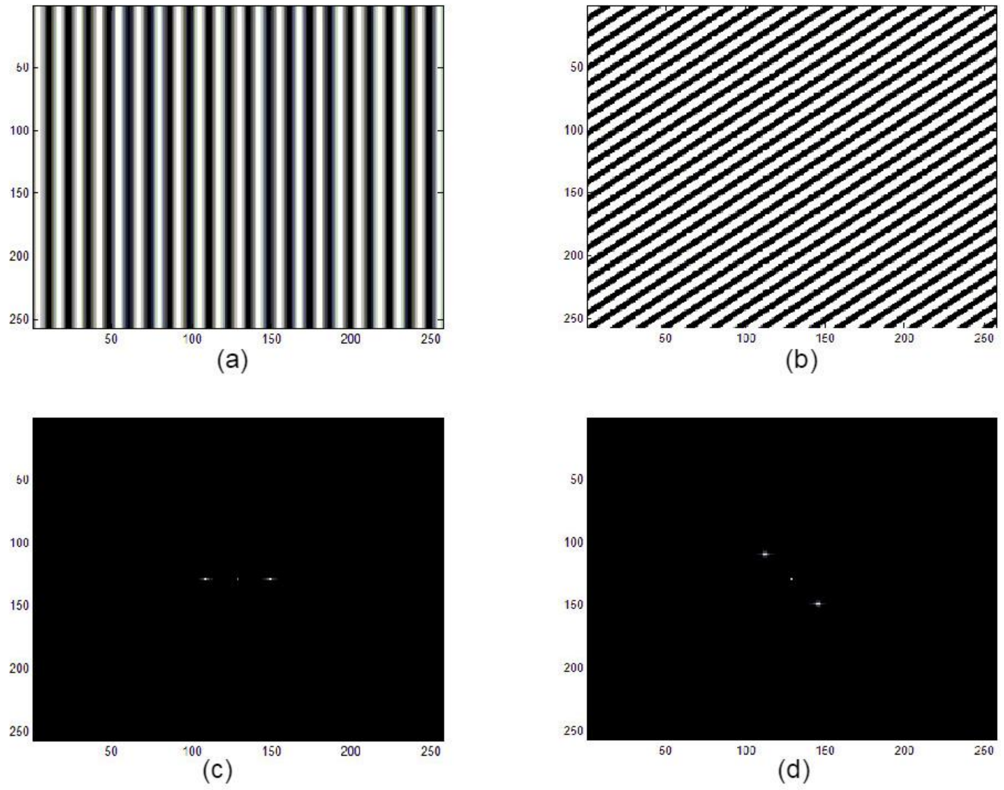

Figure 5:5: (a) An intensity image with vertical gratings. (b) Another intensity image where the gratings have certain angular displacements. (c) The Fourier transform of the image present in Figure 5.4(a). The three bright dots in the Fourier image represents that there is a single spatial frequency present in the original image. (d) The Fourier transform of the image shown in (b). The diagonal representation of the dots in the Fourier image represents the corresponding angular representation of the grating in (b).

Typically, brightfield images work well with samples that are readily available for transmission based imaging, are known as amplitude objects, as the light intensity change through the sample is detectable due to the change in amplitude. However, for thin biological samples, that are transparent, the change in intensity is not enough to be detectable using brightfield system due to lack of contrast. For situations like these, variation in refractive index and thickness across the sample are responsible for phase delay (also discussed in 5.3.1). These samples are labelled as phase objects. The difference between the scenarios has been articulated in Figure 5.4.

To demonstrate the idea that numerical Fourier transform on images can be used to acquire various information, we used certain simulations which have been demonstrated in the following discussions. Different gratings have been created using MATLAB and corresponding Fourier transforms have been articulate in Figure 5.5. For images shown in Figure 5.5(a) and 5.5(b) where both have single spatial frequencies, the Fourier transform will produce the images shown in Figure 5.5(c) and 5.5(d).

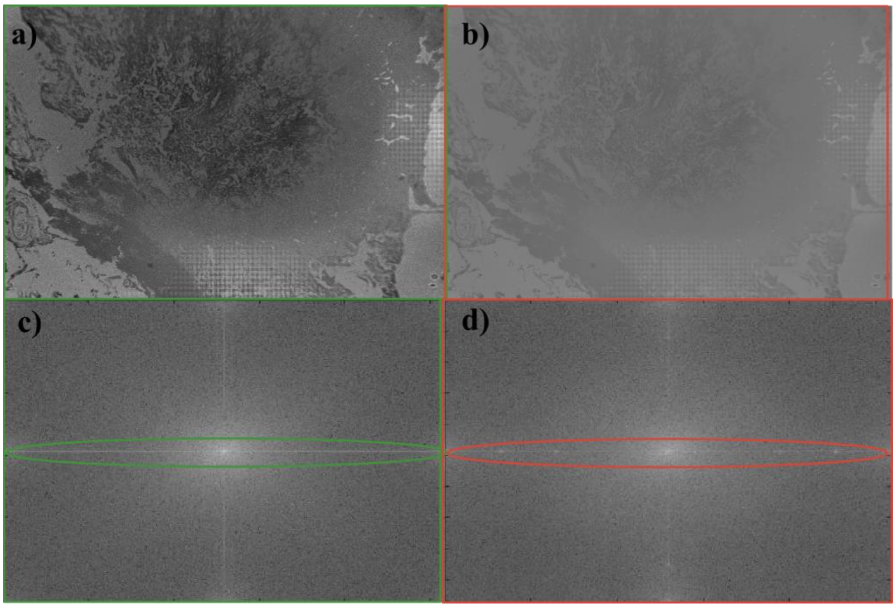

Figure 5:6: Two images and their corresponding Fourier Transforms. (a) A grayscale image (lung cancer sample). (b) the same grayscale image with a poor contrast. (c) Fourier transform of the image of 5.3(a). (d) Fourier transform of the image of 5.3(b). We can see that 5.3(d) has less bright spots than 5.3(c) that is because the spatial frequency in 5.3(b) is lower than 5.3(a).

Both the Fourier images have only three prominent components because there is single spatial frequency, where the middle spot is known as the DC term and the remaining two correspond to the spatial frequency, each being conjugate of the other. We can observe that the angular orientation of the gratings in the original image is reflected accordingly in the Fourier image as well. As the information in the Fourier image is in the complex representation (as shown in Equation 5-1, a+ib), the information can be used to extract both the magnitude and phase of the original image, given by the equations, magnitude = $\sqrt{a^2+b^2}$ and phase = $\tan^{-1}\frac{b}{a}$.

Additionally, if the two intensity images as shown in Figure 5.6(a) and Figure 5.6(b) are considered, then the one which have more spatial frequencies present, that is the one on the left, gives more bright spots in the Fourier domain (Figure 5.6(c)). On the other hand, the image which has poor contrast level provides less bright spots surrounding the DC component in the Fourier transformed image (Figure 5.6(d)).

5.2.2. Spatial Filtering

When Fourier transform is done on images the transformed image can be manipulated in the frequency domain. As an example, any image which is in the frequency domain can be manipulated using filters. A low-pass filter will block the higher spatial frequencies and is used to blur the image (Figure 5.7(d)), a high-pass filter blocks the lower spatial frequencies and they are responsible for the sharpness of the edges (Figure 5.7(f)) and band-pass filters can block/pass a frequency spectrum according to the purpose of interest and then using inverse Fourier transform they can be transformed back to spatial domain.

Figure 5.7 shows an image, its 2D Fourier transform, low pass filter and the corresponding output image, and also high pass filter and the resulting image.

5.2.3. Optical Fourier Transform

The simplest way of achieving optical Fourier transform is by using a diffraction aperture, illuminating the aperture with parallel lights (collimated) and observing the resulting diffraction patterns at a very far image plane [169]. But if we look at the Fourier transform integrals we can see that the limits are set to infinity, which means that for a lensless optical Fourier transform the image plane has to be set very far to approximately achieve Fourier transform and that in turn will generate very small Fourier transform unit. The other way would be to introduce an optical lens, which in fact will bring the Fourier information at the backfocal plane considering parallel waves are placed at a far-field image plane.

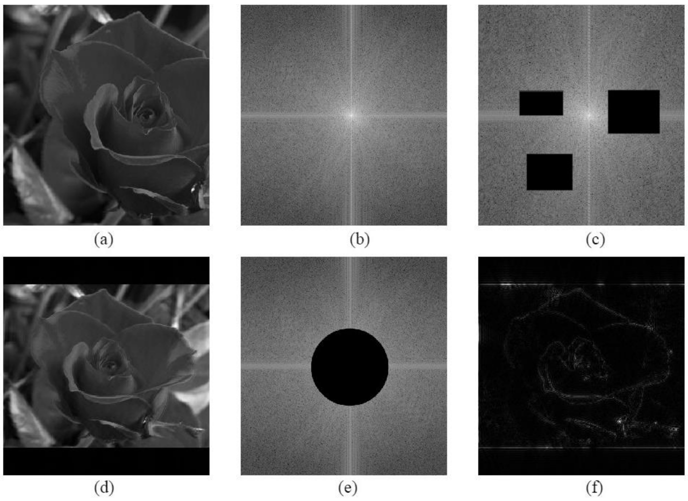

Figure 5:7: (a) A grayscale image [170]. (b) The 2D Fourier Transform of the image. (c) Some random filters blocking some high frequencies. (d) The corresponding image after applying the low pass filter which is evident to be blurred after some high frequencies are blocked. (e) A filter that is blocking the low frequencies. (f) The image corresponding to the high pass filter where it is evident the low frequencies are blocked, and the high frequencies are representing the edges.

Thus, when a monochromatic light as plane, parallel waves passes through a lens, Fourier transform of the wave is found at the focal plane of the lens where Fraunhofer’s diffraction pattern is generated at the focal plane [163]. This complicated operation can be done using, (i) very simple optical setup, (ii) the basic laws of diffraction and wave propagation. Figure 5.8 shows parallel waves placed at 1-focal length, being Fourier transformed by the lens and the FT image being created at the Fourier plane.

5.2.4. Imaging techniques using Fourier Optics

The computational strength of Fourier optics has been used for the advancement of microscopy systems such as, optical holography. Computational microscopes are structured in a manner where the objects are illuminated using partially coherent/coherent illumination and the intensities of the diffraction pattern are recorded on an image sensor. The image is then computationally processed using Fourier transform or other approaches to acquire high-quality image.

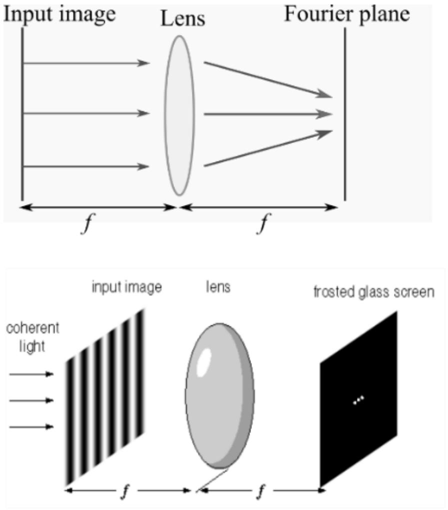

Figure 5:8: The concept of Fourier transform using a lens is illustrated here. When plane waves are diffracted off an object at 1-focal distance of the lens, an image is created at the conjugate focal plane of the lens, which is labelled as image plane. The image plane shows three points because of the transparency placed at the input image plane.

The emergence and growth of computational microscopes using the fundamental concepts of Fourier optics for various microscopic systems (holography, ptychographic) have been used to remove the restriction of the lens out of the optical microscopic systems. The introduction to computation microscopy offers a paradigm of achieving better resolutions, better magnification and better SBP of the microscopic systems[171-174]. Digital Holographic Microscopy (DHM), diffraction tomography (DT), Fourier Ptychographic Microscopy (FPM) are some examples of microscope modalities where Fourier domain information has been used for image processing. The computational strength of FPM has been used in this thesis hence the discussion on DHM/DT are out of the scope of this research. So, in the following sections we will discuss about FPM.

Moreover, Fourier transform has also been useful in cryptography, for securely transmitting imaging information over the network [175].

5.3. Inverse Problem

Typically, if there is a problem where the cause and effect share a direct forward relationship, the problem is known as forward problem. Inverse problem is the domain of problems where the effect is known but the cause for the effect is unknown and therefore, some optimization approach is required to acquire the cause information. This idea has been depicted in Figure 5.9.

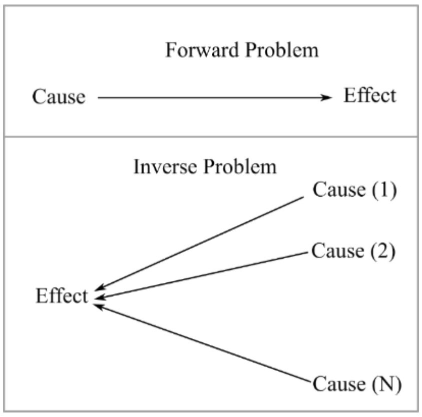

Figure 5:9: Simple schematic depicting forward vs inverse problem. If we consider the image acquired by the lens shown in Figure 5.13, then it is noticeable that the imaging system recorded only intensity information. From this intensity information using Fourier optics and iterative algorithms we can retrieve phase, which is the inverse problem for imaging systems.

This idea in the context of imaging systems is relevant where we use typical brightfield imaging systems without any additional means to capture the phase information. We only have the intensity information recorded by the sensor. Intensity is square of amplitude which does not contain phase information. Phase retrieval algorithms have been developed to allow computational image processing to iteratively retrieve phase information from intensity information only. These problems are known as inverse problems and typically fall into ill-posed problems as there are more than one solution available.

5.3.1. Phase measurement using optical techniques

In order to optically measure phase information of thin, transparent objects, different optical microscopes have been evolved since early 20th century.

Phase contrast: In 1942 Fritz Zernike introduced a phase plate in a brightfield microscope that shifts only the DC term and allows interference with high spatial frequencies. This in turn allows conversion from intensity to phase information, this popular idea is known as Phase Contrast Microscopy for which he received Nobel prize in 1952 [66]. We show a phase contrast image from Zernike's work in Figure 5.10. Previously we demonstrated in Figure 5.9 that the filters can be used to block certain imaging information that in turn helps in acquiring other information like edges. The same idea can be seen in Figure 5.10 where the use of a physical phase plate increases sharpness in the edges of the images.

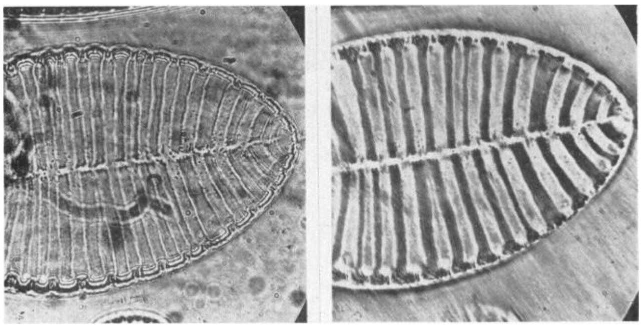

Figure 5:10: A diatom imaged using a brightfield microscope (left) and with a phase plate (right). Oldest photomicrograph recorded by Zernike in 1932 [176].

Holography using interferometry: In 1947 [177] Gabor proposed his popular means for measuring phase of a wavefront with the introduction of a reference wave in the system where the interference pattern created by the original and reference wave can be recorded as fringes, known as a hologram. Then using Fourier transform its simple to extract the phase information (the fringes appear like Figure 5.5(a) and (b)).

These ideas require modification in the imaging system. But our proposed idea is to offer decentralized, compact, modular imaging systems. So, we resorted to alternative approaches which fall into the category of inverse problems as we intended to use intensity information only that relies heavily on computational approach allowing further imaging performance improvements.

5.3.2. Computational phase retrieval techniques (inverse problem)

Later, in 1970 Gerchberg-Saxton (GS) proposed iterative algorithm to retrieve the phase information from intensity information only, which is where the foundation of FP "phase retrieval algorithm" lies [178]. Originally, GS algorithm used 2 intensity measurements, one at the object plane and another at the Fourier plane, and by imposing 2 constraints, Fourier transform back and forth between the 2 planes and an error reduction approach, the algorithm converges to a solution after a certain number of iterations or when the error reaches minimum.

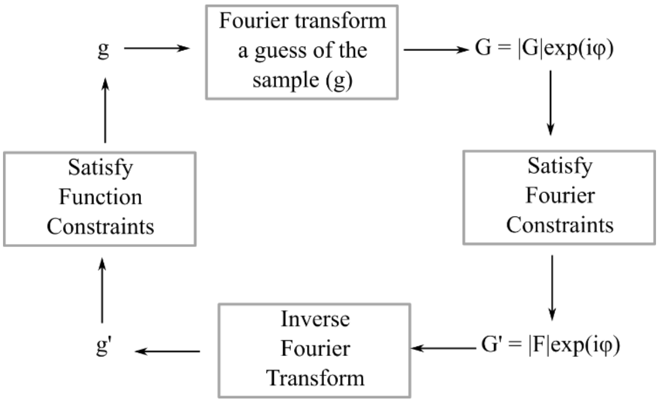

Figure 5:11: Original error-reduction algorithm used by Gerchberg-Saxton for phase retrieval from intensity images only [178].

The original GS algorithm has been articulated in Figure 5.11 which works by using measured images as constraints in both object (amplitude of the sample image) and Fourier planes. Later, Fienup updated the and that has been used in the first FP algorithm [11].

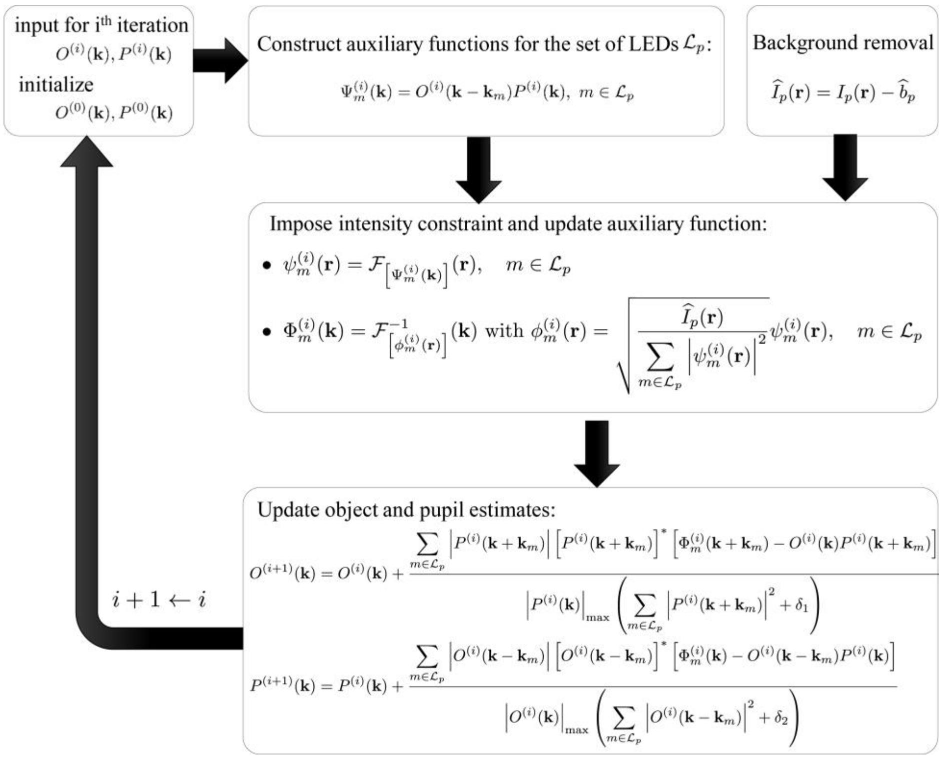

Figure 5:12: Iterative algorithm for optimization of object and pupil using Fourier Ptychography [12]. In this work they have used Newton's 2nd order optimization approach to iteratively improve the sample spectrum (O) and in parallel retrieve the pupil (P). Our proposed work uses a modified version of this algorithm.

Later a number of works have been done to demonstrate various 1st order (GS), 2nd order (Newton's) optimization algorithms can be used to iteratively retrieve phase from intensity information only, which can converge faster in lesser iterations, with lesser artifacts, especially when the dataset FP deals with is a non-convex, nonlinear optimization problem [12, 179]. The algorithm used in [12] uses 2nd order Newton's method for optimization which has been articulated in Figure 5.12.

5.4. Fourier Ptychographic Microscopy

Fourier Ptychographic Microscopy (FPM) is an emerging computational technique to improve imaging performance of microscopic images that otherwise is limited by lenses in the imaging system [11, 12]. The technique has reportedly been able to computationally, i) improve resolution beyond the limitation of the objective lens, ii) improve space bandwidth product (SBP) of the system, iii) retrieve phase information from intensity images only, iv) remove optical aberrations/distortions and v) retrieve pupil functions across the sample. FPM is a combinatorial performance of imaging experiments and optimization algorithms. In the following subsections we will first introduce the fundamental modelling blocks of FPM.

5.4.1. Illumination scheme for Fourier Ptychography

Brightfield optical microscope (using Köhler illumination) is the simplest form among all the microscopes where typically light passing through (transmission-based) or reflecting off (reflection-based) of a sample is recorded. The property of light is not altered in brightfield imaging, such as, no filter or polarizer is used.

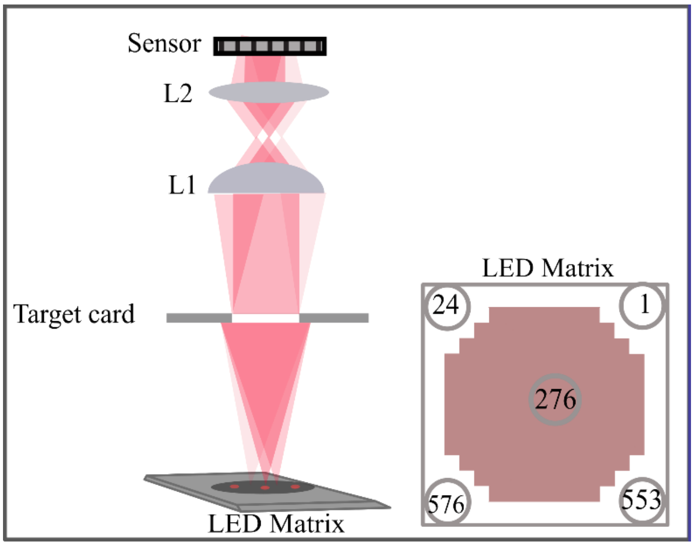

Figure 5:13: Schematic of experimental setup for Fourier Ptychography. An LED matrix (24 × 24 size with a total of 576 LEDs and the index of the centre LED being 276) is used to replace the illumination of a microscope to acquire multiple images of the sample.

Typically, a brightfield microscope is composed of the fundamental components, as shown in Figure 5.13, i) A source of illumination (typically a bulb or in modern compound microscopes, a laser), ii) optics, typically objective lens for image formation, iii) a sensor to record the data. Additional lenses, such as collimator, tube lenses, and condensers are used usually to control different properties of imaging, such as varying magnification.

Overall, brightfield microscopes provide high resolution imaging. In FPM the only change from typical brightfield optical microscope is the use of an LED matrix as an illumination source. More than one images of the sample are acquired in FPM by turning on different LEDs. The LED matrix typically provides incoherent illumination but if placed at a certain distance from the sample, and if the illumination area is significantly small, such as, ~200 µm, then the illumination is considered as spatially coherent.

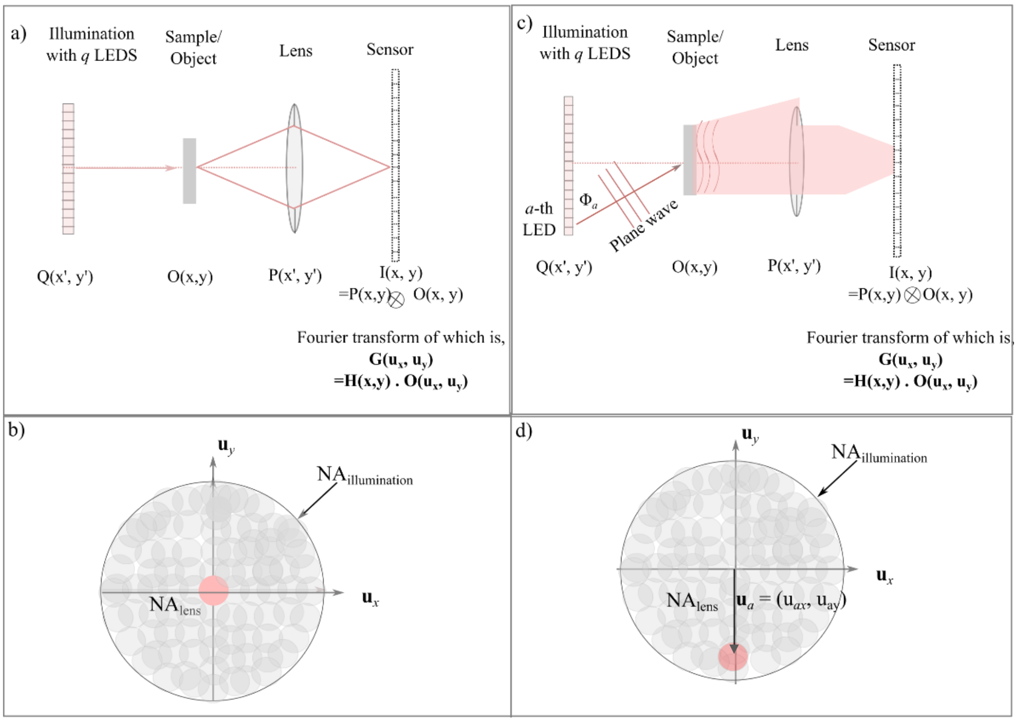

Figure 5:14: Shifting illumination using an LED matrix for Fourier Ptychographic Microscopic technique. a) A simple imaging setup shown different planes as discussed in section 5.1. Convolution of pupil wavefront and sample wavefront is acquired at the sensor. b) Shows the complete Fourier spectrum achievable through shifting illumination [167]. The $NA_{illumination}$ is achieved by calculating the maximum angle provided by the farthest LED. c) If another LED a is used to angularly illuminate the sample, the lens performs as a filter and blocks certain light. d) The angular illumination provided by the LED a provides different information on Fourier spectrum as shown by the vector, $u_a=(u_{ax}, u_{ay})$.

As different LEDs provide the sample image from different angles, each image contains varying information in the Fourier spectrum. Schematic of FP imaging system has been articulated in Figure 5.15. An LED matrix with q-LEDs is used to illuminate the sample. The orientation of the LEDs used on the matrix is a circular aperture as shown.

In Figure 5.14 we elaborated on the idea of using shifting illumination in FP. If the centre LED is turned on and the optical axis is incident on the centre LED, we will achieve the imaging system shown in Figure 5.14(a). Figure 5.14(b) shows corresponding Fourier spectrum where the centre LED is found at the centre. $\mathrm{NA}_{\mathrm{illumination}}$ is the incident angle from the farthest LED, such as, φ_a as shown in Figure 5.14(c). The circular aperture of the $\mathrm{NA}_{\mathrm{illumination}}$ is achieved by turning on a circular subset of LEDs as shown previously in Figure 5.13. If we shift the coordinates of the LED and an LED a is turned on as shown in Figure 5.16(c) then there will be a shift in the Fourier spectrum as defined by the vector, $\mathbf{u}_a = \left(\mathbf{u}_{ax}, \mathbf{u}_{ay}\right)$. By turning on all q LEDs, the entire Fourier spectrum thus gets filled with information acquired from varying angular illuminations.

This enables higher frequency information to be captured and that information supports in reconstructing images with more information. Moreover, a full sequential scan of the sample using a 2D matrix of LEDs, while each angular illumination generating a 2D image, provides us with a 4D dataset which is similar to phase space measurement [180] or light-sheet measurements [181].

5.4.2. Forward imaging model in Fourier Ptychography

The imaging model used by FP is a coherent imaging system where coherence is achieved by ensuring sufficient distance between illumination source and sample. We will use the simple imaging model shown in Figure 5.1. We will consider the sample is sufficiently thin and is given by, $o(r)$, where, $r = (x, y)$ denotes the 2D spatial coordinates on the sample plane.

As shown in Figure 5.14, each LED illuminates the sample from a different angle with a plane wave given by, $\exp(i2\pi u_a.r)$, where, $u_a = \left(u_{ax}, u_{ay}\right)$ is the spatial frequency corresponding to the a-th LED, a=1, 2, …, q. The light that passes through the sample, we will denote that wave as "exit wave", is a multiplication between the sample and the complex field given by the illumination, $o(r).\exp(i2\pi\mathbf{u}_a.r)$. Tilted plane wave implicates that the Fourier transform of this exit wave is shifted in the Fourier spectrum of the sample, $O(\mathbf{u}-\mathbf{u}_a)$, where $O(\mathbf{u})$ = FFT$\{o(r)\}$ and FFT is the 2D Fourier transform. Then this exit wave passes through the lens present in the system, where the lens aperture or the pupil function, $P(\mathbf{u})$ works as a low-pass filter. The function $P(\mathbf{u})$ is a circular matrix where the radius of the circle is defined by the $\mathrm{NA}_{\mathrm{lens}}$. The retrieval of this pupil function is also of interest as the wavefront at the pupil plane provides the idea of amount of aberrations/distortions exhibited by the lens. Lastly, if we take the inverse Fourier transform (IFFT) of the wave exiting the lens can give us the acquired intensity at the image plane (ignoring noise and magnification), where,

$$I_a(r) = \left| IFFT\{P(\mathbf{u})O(\mathbf{u}-\mathbf{u}_a)\} \right|^2 \tag{5-3}$$

This gives us the forward model of the FP imaging system, that how light is travelling through the sample and is acquired as intensity at the sensor.

5.4.3. Aperture synthesis

Aperture synthesis has been used in astronomy for over 30 years known as Synthetic Aperture Radar (SAR) [168]. Aperture synthesis means the use of mixed signals acquired from a collection of telescopes to create one image with higher angular resolution that would have been possible if there was a larger aperture telescope. So, the use of the combination of telescopes to synthetically increase the aperture of the system without using a larger aperture telescope. This idea has been used in FP with the introduction of the LED matrix. The idea is to synthetically increase the aperture of the system without having to change the lens of the system.

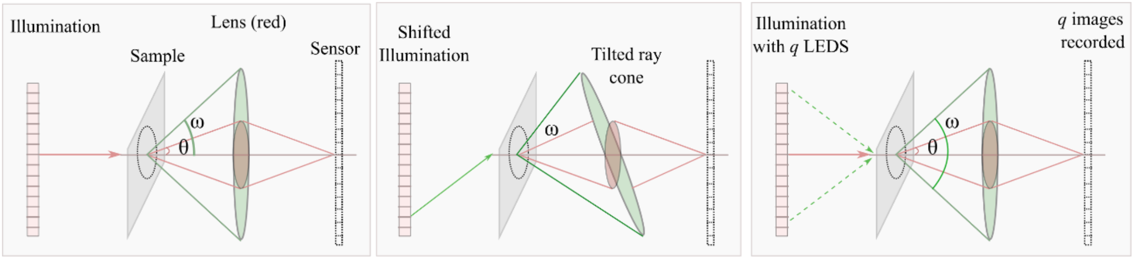

Figure 5:15: Shifted illumination capturing larger cone of light in the imaging system using the same lens. A typical microscope with an objective lens of aperture $NA = n\sin\theta$ provides can capture only the red cone of rays emerging at half of θ. If the illumination is shifted it is also possible to capture the green cone of rays. FP uses q different LEDs to capture q unique images of the sample. From the set of q images FP can computationally reconstruct an image with larger synthetic NA [167].

The aperture in the imaging system shown in Figure 5.15 and Figure 5.16 is fixed by the lens in the system which defines the achievable resolution. As FP uses LED matrix instead of a single light source, the shifted illumination on 2D array provides the system with larger cone accepted by the lens in the system. This has been demonstrated in Figure 5.16. The maximum angle acquired from the farthest LED is calculated from the set of raw images and then the sum of the illumination aperture and the objective aperture is used as the synthetic aperture, $NA_{illumination} + NA_{lens}$ = Synthetic NA. The increase in synthetic aperture can be directly related to the expected resolution improvement based on Abbe's resolution limit equation as discussed in Chapter 1 earlier. The difficulty of aperture synthesis in astronomy is that the use of multiple lenses or mechanical movement of the radiation source is necessary to acquire the interference pattern – which aids resolution improvement. But in FP there is no mechanical scanning or requirement for lens arrays. The simple use of an LED matrix and sequential programmed control of the LEDs is sufficient to ensure more Fourier information of the sample can be obtained (we will discuss the Fourier spectrum overlap concept later). This is one advantage of FP in resolution and consequently SBP improvement.

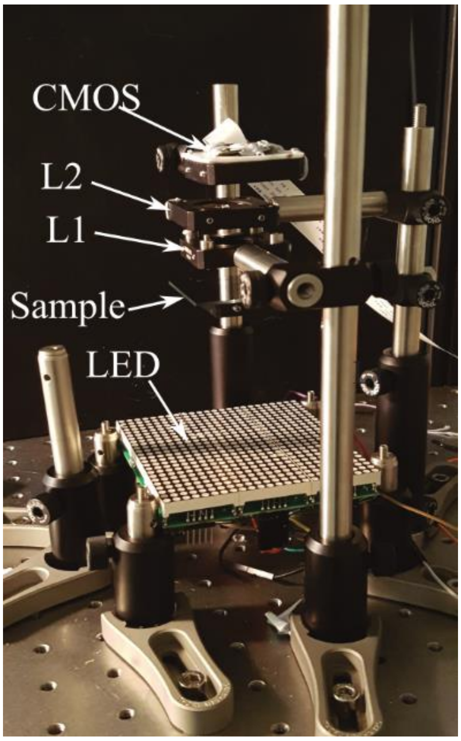

Figure 5:16: Proposed experimental setup for implementing Fourier Ptychography. This whole setup requires 10 cm × 10 cm × 15 cm, thus offers high quality imaging (post-reconstruction) in compact form.

5.5. Proposed experimental work using FP

Here, we discuss about the use of Fourier Ptychography in our research. The proposed experimental setup has been shown in Figure 5.18. The imaging system consists of i) a 24×24 LED matrix (ICstation MAX7219 LEDs), ii) a sample (typically we have used USAF target card 1951 with groups 0-7), iii) A singlet lens (L1) performing as an objective lens (we used various commercial and moldless lenses to test FP), iv) L2 performing as a tube lens, and v) Raspberry pi camera sensor (CMOS Omnivision OV 5647). Raspberry pi model 2B has been used throughout this work (not shown in the Figure).

Fourier Ptychography performs based on a number of raw low-resolution images acquired using the LED matrix, and through a computational processing of the images. The computational optimization used in this work has been adapted from the work by Tian *et al* [12]. The optimization process requires tuning and adjustment of several parameters associated with the proposed algorithm. In this section we shall introduce the parameters that have been relevant for optimization of moldless lens data using FP. For our proposed system using moldless lenses, the imaging system contains significant amount of variability due to the variability presented by the lenses. This introduces added level of difficulty in optimization which is already an ill-posed problem by definition.

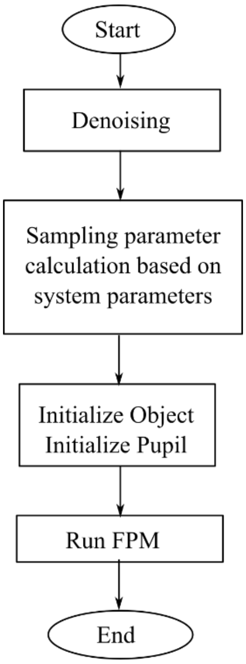

Figure 5:17: Simple process flow diagram of how FP reconstruction works. The process requires multiple sampling parameters to be set based on the imaging system. Optimization is achieved through iterative reconstructions on a selected region of interest, as FP works base on local optimization.

The variabilities in the system are given by, i) The high distortions and aberrations of the moldless lenses, ii) The use of these lenses in the imaging system, iii) The angular variation in the illumination extending the aberrations across the sample.

5.6. Proposed reconstruction process

In the earlier sections, we have introduced some algorithms found in literature that implement iterative optimization approaches for phase retrieval, where the imaging resolution, SBP also improve during the process. Here we introduce the proposed algorithm. A simplistic flowchart of the whole FP reconstruction process has been shown in Figure 5.17. The process requires different steps to setup the system parameters prior to the optimization routine.

The run FPM block in the flowchart is main reconstruction process which has been shown in Figure 5.18. The process starts by acquiring *q*=293 images using an LED matrix as shown in Figure 5.16. Then using program written in MATLAB the reconstruction process can acquire high quality full FOV image.

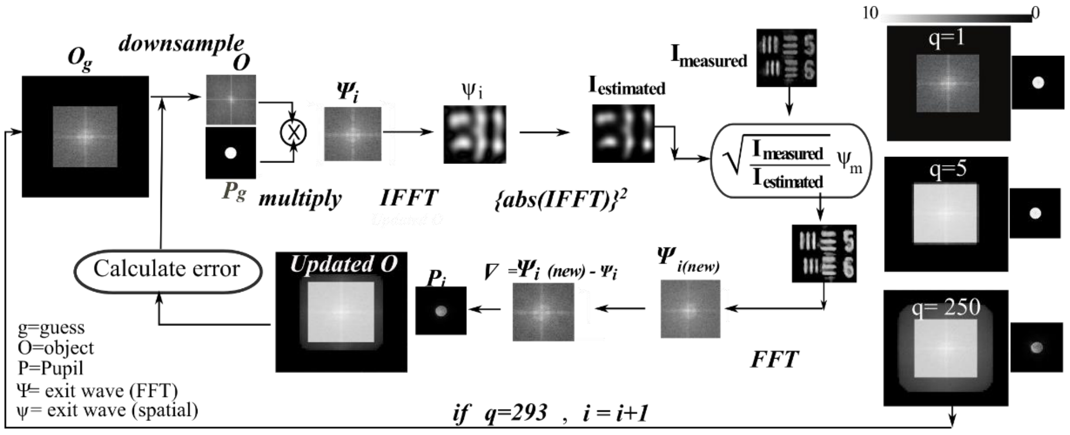

Figure 5:18: Proposed Fourier Ptychography reconstruction algorithm [182]. The FP process works by moving back and forth between spatial and Fourier domains. Here one iteration of the whole process has been demonstrated with the use of Fourier and spatial spectrum.

As FP works by local optimization, the whole process is run on a chosen ROI. The size of the ROI is determined by coherence illumination area of the LED; calculated based on the wavelength of the LED, λ, height between the LED matrix, z and the LED illumination area d [174]. The expected ROI is chosen to be around 280 µm by 280 µm, which translates to 200×200 pixels. For FP to give better results and converge to a solution, the program is run for *nIter* times. For the proposed work, we have used ~90 iterations as discussed in [179]. Here, we shall describe in detail each step within a single iteration *i*.

At each iteration *i*, for a given LED *q*, we calculate the transmitted wave exiting from the imaging lens to be $\boldsymbol{\Psi}^i_q\left(\mathbf{k}\right) = O^i(\mathbf{k} - \mathbf{k}_q)P^i(\mathbf{k})$. The resulting complex amplitude of

$\boldsymbol{\Psi}^{i}_{q}\left(\mathbf{k}\right)$ is inverse Fourier transformed (IFFT) and squared to retrieve an estimate of the intensity pattern of the image $i_q\left(\mathbf{r}\right)=\left|FFT\left[O\left(\mathbf{k}-\mathbf{k}_q\right)\bullet P\left(\mathbf{k}\right)\right]\left(\mathbf{r}\right)\right|^2$ where, $\mathbf{r}=\left(x,y\right)$ is the radial coordinate, and $\boldsymbol{O}\left(\mathbf{k}-\mathbf{k}_q\right)$ is the object for q-th LED shifted by the vector $\mathbf{k}_q$, $\boldsymbol{P}(\mathbf{k})$ is the pupil function and $FFT\left(\mathbf{r}\right)$ is the Fourier transform. For convergence, we imposed two constraints, one based on amplitude and the other based on Tikhonov regularization. An amplitude-based constraint here given by, $\varphi^i_q\left(\mathbf{r}\right)=\sqrt{\frac{I_{measured}\left(\mathbf{r}\right)}{I_{estimated}\left(\mathbf{r}\right)}}\cdot\psi^{i}_{q}\left(\mathbf{r}\right)$, where I_{measured} is corrected q-th raw image. The difference (∇) between the new and previous transmitted complex intensity for each q-th image is used to update the object and pupil functions. The Tikhonov regularization parameters constraints required for object and pupil recovery are the two independent parameters, α and β shown in equations (5-4) and equation (5-5) [183]. The ratio of α and β is important to ensure convergence and quality of reconstruction, which has been observed that for our imaging setup $\frac{\alpha}{\beta}\gg 10$ ensures convergence.

$$O^{i+1}\left(\mathbf{k}\right)=O^{i}\left(\mathbf{k}\right)+\frac{\frac{1}{\max\left(\left|P^{i}\left(\mathbf{k}\right)\right|\right)}\cdot\left|P^{i}\left(\mathbf{k}+\mathbf{k}_q\right)\right|\cdot\left|P^{i}\left(\mathbf{k}+\mathbf{k}_q\right)\right|^{*}\cdot\left(\varphi^{i}_{q}\left(\mathbf{k}+\mathbf{k}_q\right)-O^{i}\left(\mathbf{k}\right)\cdot P^{i}\left(\mathbf{k}+\mathbf{k}_q\right)\right)}{\left|P^{i}\left(\mathbf{k}\right)\right|^{2}+\alpha} \tag{5-4}$$

$$P^{i+1}\left(\mathbf{k}\right)=P^{i}\left(\mathbf{k}\right)+\frac{\frac{1}{\max\left(\left|O^{i}\left(\mathbf{k}-\mathbf{k}_q\right)\right|\right)\cdot\left|O^{i}\left(\mathbf{k}-\mathbf{k}_q\right)\right|^{*}}\cdot\left(\varphi^{i}_{q}\left(\mathbf{k}\right)-O^{i}\left(\mathbf{k}-\mathbf{k}_q\right)\cdot P^{i}\left(\mathbf{k}\right)\right)}{\left|O^{i}\left(\mathbf{k}-\mathbf{k}_q\right)\right|^{2}+\beta} \tag{5-5}$$

A large part of FP optimisation is based on iterative phase retrieval algorithms that is similar to established techniques *i.e.* Gerchberg-Saxton (GS) [184] and later improved by Fienup [178, 185]. Lately, a second order Newton's method was implemented in FP imaging which results in lower iterations and lesser image artifacts [179]. These methods are capable of retrieving phase information from intensity images only and utilized the first-order derivative of the cost function for convergence to a solution. In this work, we adopted Levenberg-Marquardt based second-order Newton’s method previously used in multiplexed illumination-based FP systems [12, 179].

5.7. Sampling criteria for FP reconstruction process

The resolution performance of an FP system is highly dependent on identifying optical and digital sampling parameters such as numerical aperture, optical magnification, pixel size and optical wavelength. As FP acquires multiple images and each image fills up a region in the Fourier spectrum (shown in Figure 5.18) it is essential to ensure the spectrums overlap so that the iterative algorithm converges to a solution. The amount of overlap between neighbouring spatial frequency spectrums generated by individual LEDs also affects the FP process. To ensure sufficient overlap, the relationship of the separation between each adjacent LEDs (*s*) and the height (*h*) between sample and LED is determined by equation (6-3) [186].

$$R_{overlap} = \frac{1}{\pi}\left[2\cos^{-1}\left(\frac{1}{2R_L}\right) - \frac{1}{R_L}\sqrt{1-\left(\frac{1}{2R_L}\right)^2}\right] \tag{5-6}$$

where $R_L = NA\frac{\sqrt{s^2+h^2}}{s}$. According to, [186], for Roverlap greater than 31.81%, there was noticeable improvement in the rate of convergence. This was also mentioned that a minimum of ~35% overlap is required for quality reconstruction [187]. Roverlap values for proposed system have been articulated in Appendix B.

5.8. Resolution improvement using FP

Since the first use of shifted illumination in microscopy to achieve Fourier Ptychography (FP) in 2013, it has been demonstrated that FP can turn megapixel images into gigapixels [11, 12, 188]. That means with the use of aperture synthesis and computational iterative phase retrieval algorithms, FP can improve the Space Bandwidth Product (SBP) of microscope systems. These works also reported the successful label-free phase retrieval from intensity images and there have been reports of pupil retrieval which gives the wavefront aberration information at the exit plane of the lens [12, 189].

5.9. Computational aberration correction

FP uses computational wavefront correction approach similar to ideas that have been used in adaptive optics. The idea is to introduce a guess phase map digitally into the object's spectrum and by two-step multiplication process. As the FP approach uses the measured data from multiple images to reconstruct the object spectrum and the pupil concurrently, the multiplication operations ensure convergence [11].

5.10. Relevant parameters for FP reconstruction

In order for the FP reconstruction program to work based on the experimental setup shown in Figure 5.16, it is necessary to setup the system parameters first. The system parameters that are important for FP reconstruction are discussed below.

5.10.1. Numerical aperture (NA)

The NA of the imaging lens is a parameter relevant for FP reconstruction. For our imaging system, we calculated the NA based on lens diameter and focal lengths of the individual lenses. For different moldless lenses the value of NA varied from 0.05 – 0.3.

5.10.2. System Magnification

The magnification acquired from the imaging setup is another important parameter for the reconstruction process. The system magnification has been calculated by, $\frac{h_i}{h_o}$, where h_i is the image height and h_o is the object height. With the use of a resolution chart, USAF target card 1951 which has a fixed known resolution, we could calculate the acquired magnification. The USAF target card we have used is a negative resolution card where groups 0 – 7 are present, each group with 6 elements. Group 0 element 1 has the largest bar width, whereas group 7 element 6 has the smallest width, that is maximum achievable resolution.

5.10.3. LED matrix details

The other parameters relevant from the imaging setup are given by the LED matrix that has been used. The distance between each LED on the matrix is important to ensure convergence. Also, the height between the LED matrix and the sample is important for ensuring spatial coherence.

5.10.4. Parameter setting to acquire reconstruction results

The requirement for sufficient sampling at the image plane and for the reconstruction process is significant to attain successful reconstruction. The illumination angle providing larger expected spatial frequency allows the FP process to assume higher number of pixels in the reconstructed image. The raw image size and the reconstructed, expected image size are related by an integer factor. The expected size of the reconstructed image is given by, $N\_recon = N\_img \times \frac{NA\_illumination + NA\_lens}{NA\_lens}$, where N_img and N_recon are the number of pixels in raw and reconstructed images respectively. Also, we need to enforce that at least Nyquist sampling requirement has been enforced, which suggests that in order to reconstruct a signal from some data we need at least double samples than the expected frequency of the signal.

5.11. Early results using FP on moldless lenses

To verify the performance of FP on various lenses, we used different imaging setups using a range of moldless lenses. Here, we introduce some of the early reconstruction results. As FP works on a selected region of interest (ROI), here we demonstrated the performance on certain regions. We will elaborate the performances further in Chapter 6.

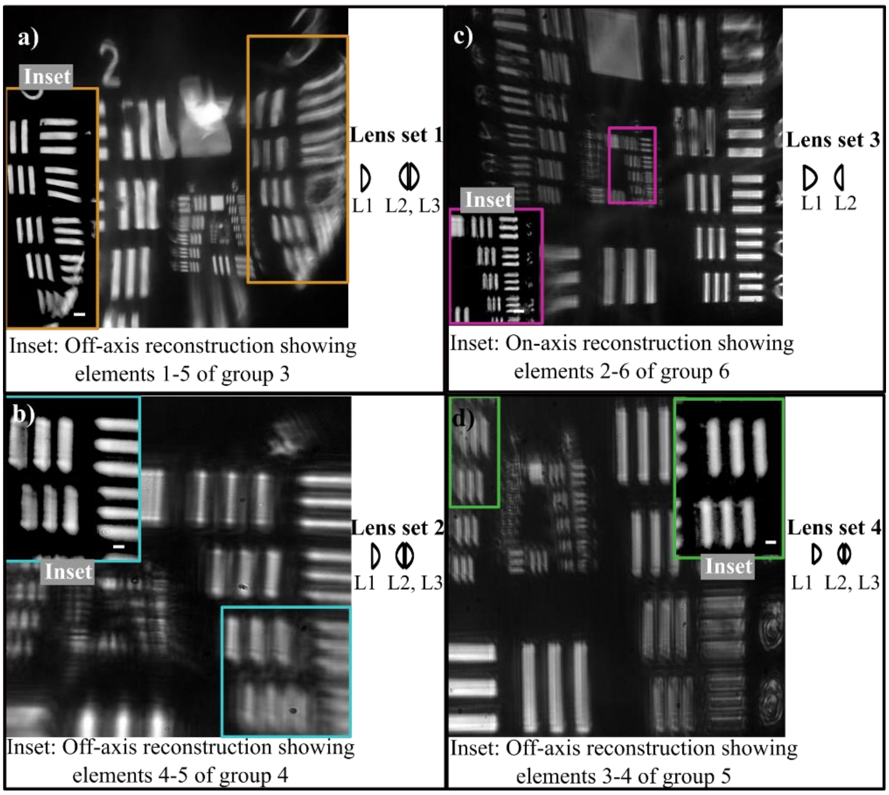

Figure 5:19: Performance of FP on different imaging systems using moldless lenses. We used one raw image taken using center LED and have demonstrated performance on a selected region.

In Figure 5.19(a) group 3 elements 1-5 can be seen (resolution of 40 µm) where FP could successfully optimize the object. Figure 5.19(b) shows reconstructed elements 4-5 of group 4 in inset (resolution of 20 µm). In Figure 5.19(c) we can see reconstructed elements 2-6 of group 6 in the inset (resolution of 4.38 µm). And, we can see elements 3-4 of group 5 in Figure 5.19(d), resolution of 9.84 µm.

5.12. Contributions

This work has been done under the supervision of Dr. Woei Ming Lee. Initially 4th year Honours student Lu Yang worked on the project to observe performance of FP with varying LED matrices on moldless lenses. The rest of the FP related works were done by me. That includes, literature review, adapting the program written by Dr. Lei

Tian, Assistant Professor, Boston University, for our imaging system, simulations, experimentation and analysis.

5.13. Chapter Summary

The purpose of this chapter was to introduce the fundamentals of Fourier optics which is the basis for computational optics. Based on the concepts of computational optics and other synthetic approaches, Fourier Ptychographic microscopy has emerged. So, we have also introduced the various theoretical concepts that formulate Fourier Ptychographic Microscopy. We have discussed about the fundamentals of Fourier Optics to elucidate how Fourier transform became a part of computational image processing. Computational image processing using various iterative optimization algorithms emerged as a tool to solve certain problems of optical imaging systems, such as, inverse problem. We have also introduced the concept that is known as digital aberration correction. We also introduced the proposed experimental setups that can be used to offer FP on moldless lens-based imaging. Preliminary results using FP on moldless lenses have been introduced here as well.

CHAPTER 6

FOURIER PTYCHOGRAPHY ON MOLDLESS LENSES

The use of computational techniques for improving microscopic imaging performance is not new. Since the use of holography, imaging systems have used computation as a tool to acquire more information or improve performance. Fourier Ptychography (FP) is an emerging microscopic technique that offers gigapixel-scale intensity and phase information with both wide FOV and high resolution that is with increased SBP across the FOV. By capturing multiple low resolution images using an LED matrix to provide varying angular information, and with the use of iterative phase-retrieval algorithm FP computationally retrieves the complex information at high resolution. But typically, FP has been used on high performing laboratory based microscopic systems which comes with certain level of optimized performance. The use of FP on a low-cost, portable system with moldless lenses has been demonstrated for the first time in this work. In this chapter, we have discussed the use of FP to recover full FOV, high SBP images on imaging systems based on moldless lenses. We will also include the different information FP is capable of retrieving through computational techniques.

6.1. FP imaging resolution improvement approach

We have already introduced the fundamental working theories of Fourier Ptychography in Chapter 5 and some early results of the performance of FP on moldless lenses. In this chapter we will elaborately demonstrate the performance of FP on moldless lenses.

Before that, we introduce what FP can offer based on literature. In Figure 6.1, reconstruction results from the work proposed by Ou *et al* has been shown where a blood smear sample has been imaged using a conventional microscope with an objective lens of

NA = 0.08 and magnification = 2x. The reconstruction results demonstrate the use of pupil aberration correction algorithms give better results.

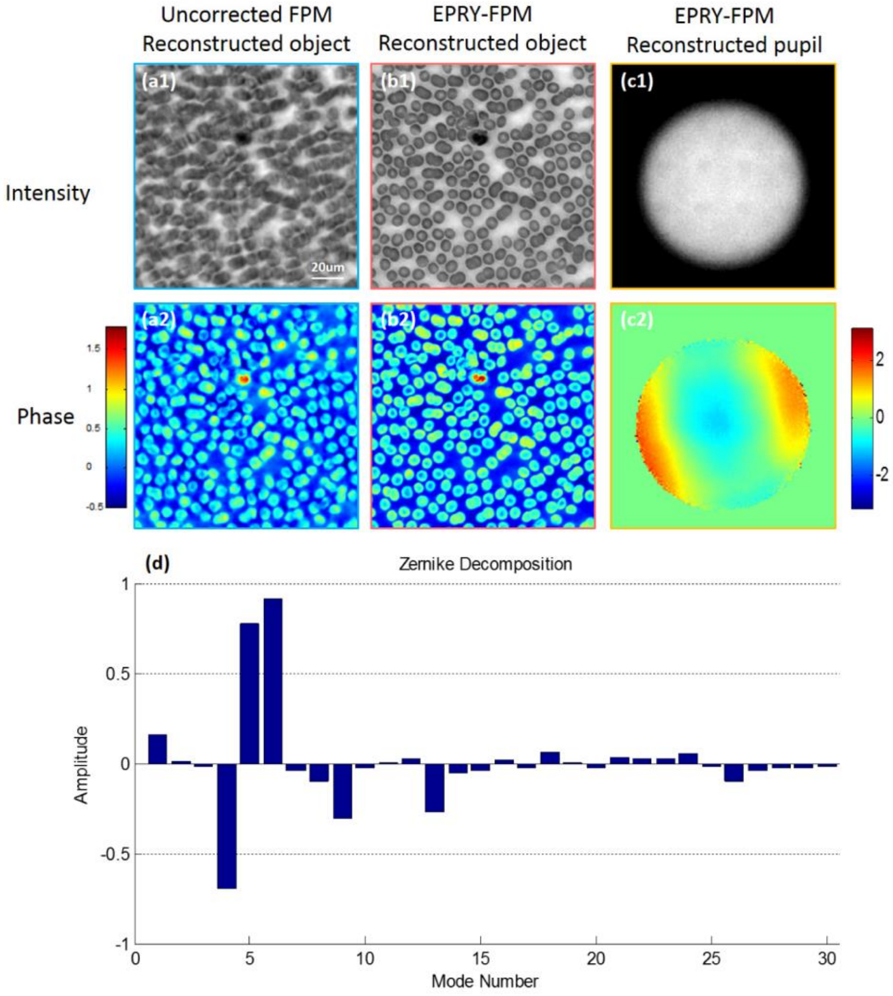

Figure 6:1: Demonstration of performance of FP on a robust laboratory based system on a blood smear dataset [189]. a1-c1) The amplitude of the recovered object and pupil after reconstruction. a2-c2) The phase of the recovered object and pupil. The pupil wavefront has been shown in c2 with the Zernike distribution of the retrieved aberrations can be seen in (d).

6.2. Limitations of proposed FP using the proposed imaging setup

While working on the Fourier ptychographic reconstruction process on the moldless elastomer lenses, we faced with certain amount of difficulties initially. The primary reason is the variability imposed by the moldless lenses in the imaging system, variability in performance, variability in exhibited aberrations/distortions across the curvature of the lens. In the following subsections we shall articulate the difficulties and also address the optimization approach we have taken to overcome the difficulties.

6.2.1. Using small aperture LED matrix

During the early stage of this work we started the experimental setup with an 8×8 LED matrix (1.2″ Adafruit LED matrix, 4 mm pitch). The smaller aperture of the LED matrix did not provide a larger $NA_{illumination}$ hence did not provide improvement in resolution or SBP after reconstruction. For example, if we consider a fixed imaging system with the LED to sample height = 90 mm, the $NA_{illumination}$ (1) = 0.16 using the 8×8 LED matrix whereas, using the proposed imaging setup shown in Figure 5.18, with a 24×24 LED matrix the $NA_{illumination}$ (2) = 0.39. Hence, we resorted to use the larger LED matrix for the proposed imaging setup.

6.2.2. Raspberry pi camera lens

The raspberry pi camera consists of a built-in lens. While using the raspberry pi camera as a sensor for the proposed microscope systems with moldless lenses as objective lenses, the pi camera lens provided us with demagnification and reduced full FOV. As shown in Figure 6.1 (left) an image captured using a commercial aspheric lens (Thorlabs 352280 – A, focal length = 18 mm and NA 0.15) cascaded with an objective 5x lens, where the pi camera lens is present in the setup. Whereas an image captured using the same imaging setup without the pi camera lens provides the image shown in Figure 6.1 (right), without the pi camera lens. The 293 raw images captured using the left imaging setup did not provide us with quality reconstruction as there are large areas of the full FOV image where there is no data present (only 0’s as they are black). To retrieve a full FOV image, it is important to fill up the Fourier space with information related to the sample, hence it is relevant to fill up the sensor area. So, after changing the LED matrix, it was our 2nd system optimization approach to take off the pi camera lens.

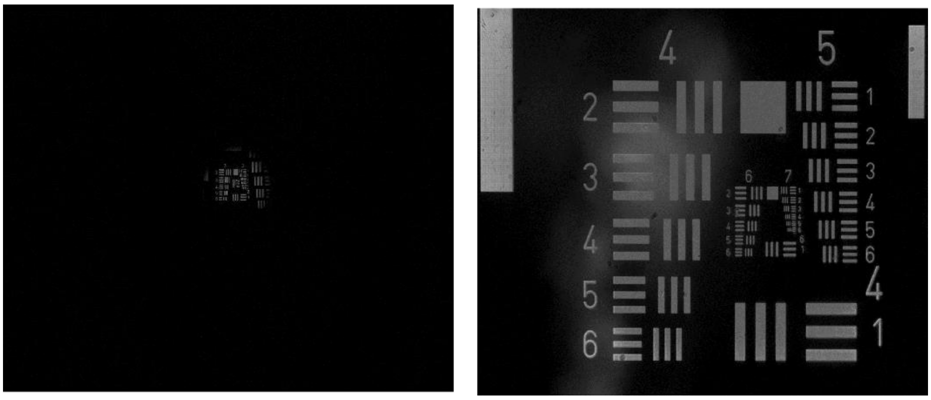

Figure 6:2: Images acquired using a commercial aspheric lens cascaded with an objective 5x. The left image was taken when the pi camera lens was present. The right image was captured removing the pi camera lens of the system.

6.2.3. Initial guess selection

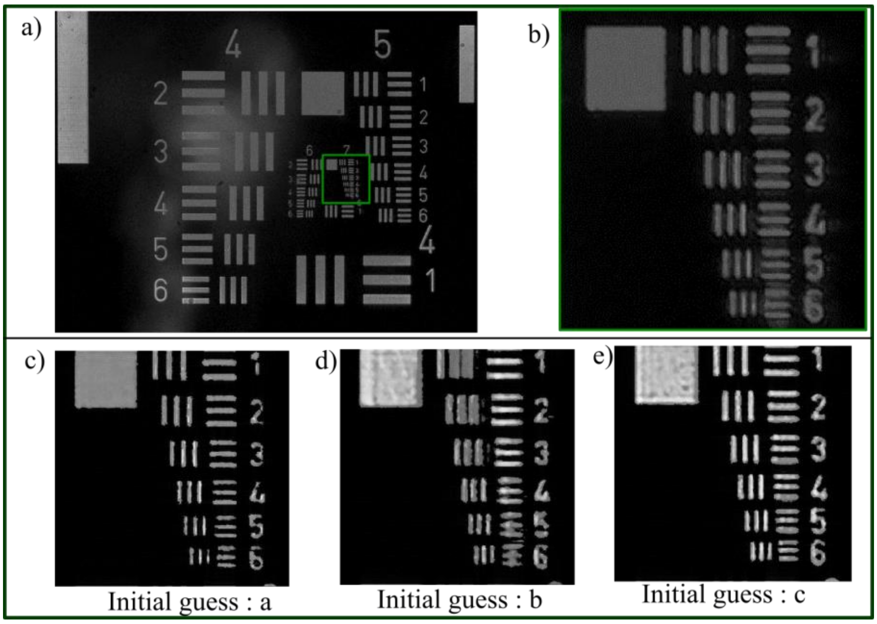

Initial guess : a
Initial guess : b
Initial guess : c

Figure 6:3: Impact of choosing different initial guesses on an ROI for reconstruction on data acquired using a commercial aspheric lens. a) Full FOV raw image using center LED. b) Cropped raw image from the ROI shown in green. c)-e) Reconstruction results for initial guesses *a-c* respectively. The variations in the reconstruction results provide us with the idea that FP works on local optimization and we need to tune the initial guess for each ROI.

In FP reconstruction process, just like any other iterative algorithms, we need to start with an initial guess considered as a high-resolution solution complex object. However, based on the work that we have adapted the choice of initial guess can be any of the brightfield images acquired using the experimental setup. FP works by local optimization, which is we choose a region of interest on the image and then run the reconstruction algorithm. While, considering the on-axis central raw image gives us the most-aligned image from the setup we preferred to use the raw image acquired using the centre LED as the initial guess during the early stage of the project. Hence, the reconstruction results did not provide high quality results across the FOV.

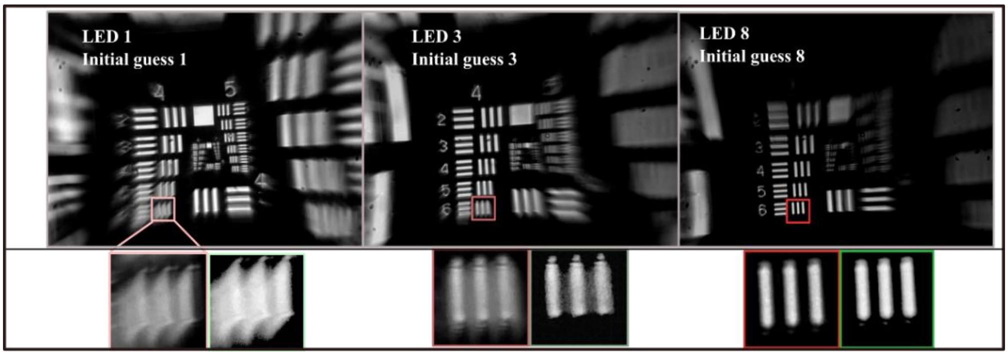

Figure 6:4: Variation in initial guess for a moldless lens based imaging setup. The different images have been acquired using different LEDs from varying angles. Raw image labelled as Initial guess =1 has been acquired using centre LED. For the region of interest shown the image labelled as initial guess = 8 provides the Fourier spectrum closest to the expected solution.

As shown in Figure 6.3, for a dataset acquired using a commercial aspheric lens and objective 5x. The region of interest shown for the demonstration of initial guess is group 7 elements 1-6. For the reconstructions, 3 different initial guesses (a, b, and c, among the different raw images) were selected which resulted into different reconstruction results. As can be seen from the reconstruction results shown in Figure 6.3, the reconstruction quality using the initial guess c gives the best outcome. So, it is important to adjust the initial guess according to the ROI. Especially for the images using the moldless lenses where the full FOV image quality varies significantly due to the higher amount of aberrations and distortions (this will be further demonstrated in Chapter 6). This has been even widely varying for the moldless lenses, which the initial guesses vary significantly for neighbouring regions. This can be seen in Figure 6.4.

6.2.4. Reduced spatial coherence

FP reconstruction process works well when the imaging system is a coherent imaging system, that is light reaching the sample is parallel. The illumination provided by the different LEDs in the LED matrix can be considered spatially coherent provided that, i) the illumination area of each LED is small (~200 µm) and, ii) the distance between the sample and the LED is sufficient [11] (70 – 100 mm). The LED matrices previously used in the other works have been Adafruit LED matrixes that did not have a cover for the LEDs. Whereas, in our system we have used ICstation LED matrix, which has a plastic covering the LEDs.

Here, the plastic acting as a diffuser is spreading the light causing a larger light emitting area. In consequence the spatial coherence that we achieved in the system is getting compromised. The LED matrices have been shown in Figure 6.5. The reduced spatial coherence in conjunction with larger aberration and distortions limited the achievable resolution improvement in our proposed work. This limitation in achieved resolution has been demonstrated in Figure 6.5.

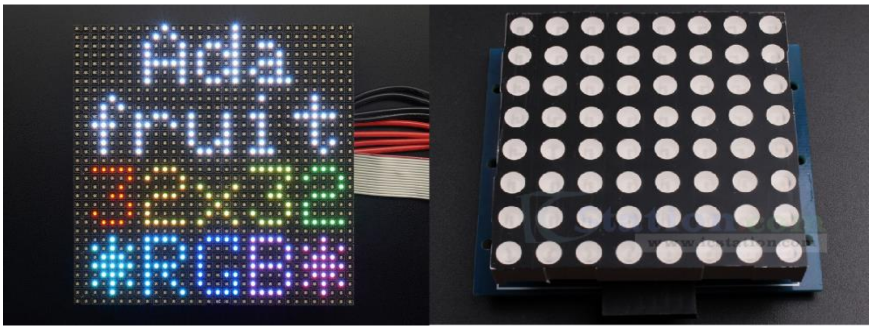

Figure 6:5: (Left) Adafruit RGB LED matrix without a cover. (Right) ICstation LED matrix within a package. We used 9 of these LED matrices to achieve a larger 24×24 LED matrix.

The expected post-processing resolution from this system can be found from the total synthetic NA. For an imaging setup where the LED is placed at 90 mm distance from the sample, the value of $NA_{illumination} = 0.39$. If the lens used in the system provides an $NA_{lens} = 0.12$, then the synthetic NA $= 0.39 + 0.12 = 0.51$ (based on $NA_{illumination}+NA_{lens}$), providing resolution of ~0.62 µm (Abbe’s resolution limit given by, $\frac{\lambda}{2NA}$, with λ=632 nm). However, the achieved resolution was 3.91 µm after FP reconstruction.

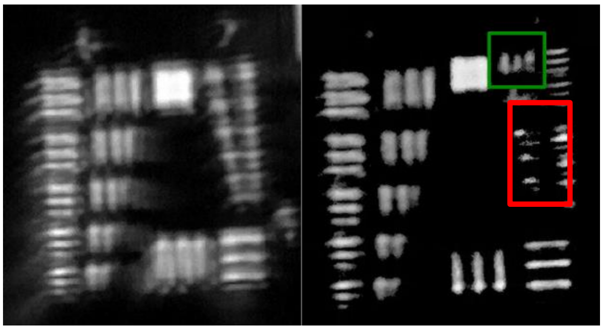

Figure 6:6: Resolution improvement limitation of the proposed high resolution imaging system using non-conventional optical techniques (Fourier Ptychography and moldless lenses). (Left)-raw image. (Right)-reconstructed image. The green square demonstrates the achieved resolution (smallest resolvable distance) after processing, which is, group 7 element 1, is 3.91 µm based on standard values. The red rectangle highlight resolutions that were not achieved. If the expected resolution of 0.61 µm has been achieved other elements of group 7 would be resolved too.

There was improvement in resolution but not as significant as previously mentioned in different articles. However, our work could remove off-axis aberrations and distortions significantly and provide an improved contrast, high SBP image which we will discuss in the next subsections.

6.3. FP on commercial lenses for proposed system:

For the proposed imaging system shown in Figure 5.18 we have initially used commercial lenses to setup the appropriate required parameters for FP reconstruction. Initially, we used a compound microscope system with two commercial lenses, L1 as objective lens, and L2 as a tube lens.

6.3.1. A compound compact system

For this imaging setup we used a commercial aspheric lens (Thorlabs 352280 – A, focal length = 18 mm and NA 0.15) as an objective lens and an objective 5x lens as tube lens. The schematic of the optical setup can be seen in Figure 6.7(a). In Figure 6.7(b) we can see the raw image that has been acquired using the centre LED.

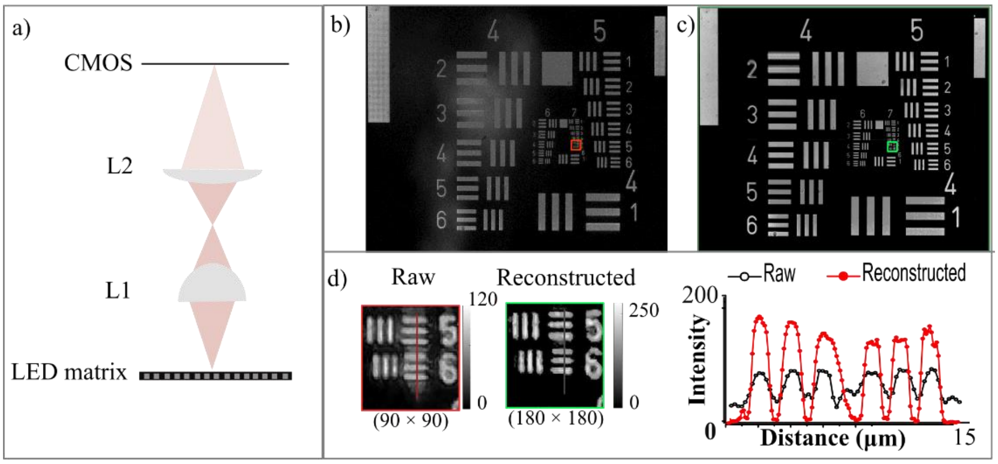

Figure 6:7: Performance of FP on a compact imaging system using commercial lenses. a) Schematic of the optical imaging setup. b) A raw image acquired using the centre LED, which is incident on the optical axis. c) The full FOV reconstructed image. d) Analysis of performance demonstrating pixel density improvement and contrast improvement.

For the full FOV reconstruction using Fourier Ptychography, as discussed in chapter 5, we chose ROI of 200×200 pixels and then iteratively recovered the high SBP images. After each ROIs are optimised, they are stitched together to generate the full FOV image. The full FOV reconstructed image for the commercial lens based setup can be seen in Figure 6.7(c). In Figure 6.7(d) we have shown a cropped raw image where elements 5-6 of group 7 can be seen. We can also see the reconstructed cropped image for that ROI. The improvement in the contrast and structural similarity is higher in reconstructed image. We have demonstrated the contrast improvement in Figure 6.7(d) through line plots. It is worth mentionable that the number of pixels in the raw image has been 90×90, whereas the pixels in the reconstructed image have doubled – improving the overall SBP the system can offer.

6.4. FP on moldless elastomer lenses

To test the performance of FP on moldless elastomer droplet lenses, we have used different moldless lenses as a simple imaging system and a compound microscope system. The compactness of the moldless lenses is better than the commercial lenses as the moldless lenses are around 3 - 4 mm in diameter and the thickness is about 1.5 - 2.3 mm.

As FP reconstruction offers improved NA based on the illumination NA provided by the LED matrix, we articulated the pre and post reconstruction NA values in Table 6-1.

Table 6-1: Numerical aperture values for moldless lens based imaging systems.

Moldless lens imaging setup	**Imaging NA (raw)**	**Imaging NA (post FP)**	**Synthetic NA (Illumination NA + Objective NA)**	**Objective NA (Calculated from lens diameter and focal length)**
Single lens system	0.04	0.08	0.47	0.08
Compound lens system	0.03	0.1	0.47	0.08

6.4.1. Single moldless lens system

For this imaging system we used a single moldless lens which was manufactured using passive dispenser. The image acquired using the centre LED has been shown in Figure 6.8(a). From the raw image we can see the presence of significant off-axis aberrations and distortions, compared to the image acquired using commercial lens.

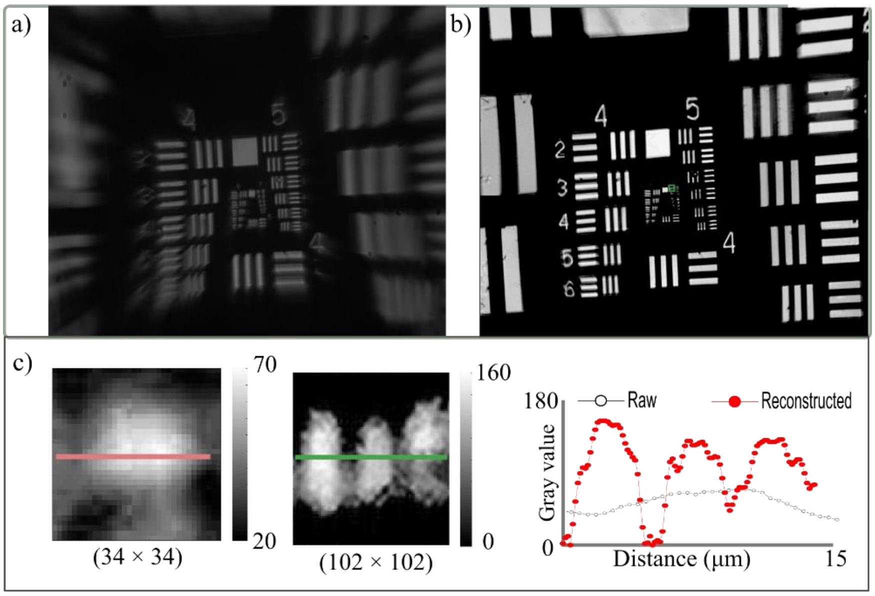

Figure 6:8: Performance of FP on moldless lens based simple imaging system. For this setup we used a moldless lens of focal length = 12 mm. a) Raw image using centre LED. b) Full FOV reconstructed image. c) Performance analysis of the reconstructed image. The cropped image is group 7 element 1 which in the raw image contains only 34×34 pixels whereas the reconstructed image contains 3 folds higher density. The pixel sizes can be apparently seen to have improved also. The contrast improvement has been demonstrated using line plots. The achieved resolution is 3.91 µm.

Alongside the contrast acquired by the moldless lenses is also poorer. Using similar reconstruction approaches discussed earlier, we have been able to reconstruct the full FOV, which has been shown in Figure 6.8(b). In Figure 6.8(c) we can see a cropped raw image corresponding to the element 1 of group 7, which is not resolvable. The number of pixels in the raw image is 34×34. In the reconstructed image we can see that there are resolvable features (offering a resolution of 3.91 µm), and also the number of pixels increased by 3-folds, offering SBP improvement of 3-folds. The overall image contrast has improved significantly which can be observed in the line plots.

6.4.2. Compound moldless lens system

The idea of this experiment was to demonstrate that the moldless lenses can be cascaded to setup compound microscope systems. The imaging setup of this experiment is similar to the one shown in Figure 6.7(a). The performance of the imaging setup (raw image shown in Figure 6.9(a)) is apparently deteriorated compared to simple imaging system (Figure 6.8(a)) as the aberrations offered by the cascaded set of moldless is cumulative and higher. But post-FP reconstructed image shown in Figure 6.9(b) demonstrates full FOV high quality image with improved SBP, resolution and contrast.

In the reconstructed image shown in Figure 6.9(b) there is still some distortion present, but mostly the image has improved and flattened. Figure 6.9 (c) shows cropped region corresponding to element 3 of group 7. In the raw image the features were not resolvable, whereas the in the reconstructed image the features are visible, yielding a resolution of 3.1 µm. We can also see the SBP improvement by 2-folds. The contrast improvement is also evident, which we have demonstrated using line-plots.

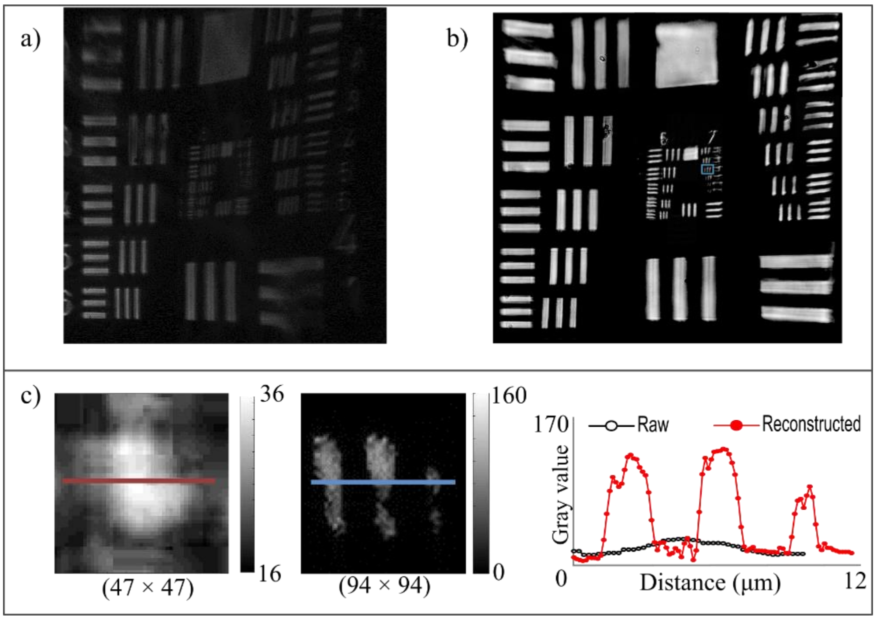

Figure 6:9: Performance of FP on moldless lens based compound imaging system. For this setup we used a pair of moldless lenses of focal length = 16 and 17 mm, respectively. a) Raw image using centre LED. b) Full FOV reconstructed image. c) Performance analysis of the reconstructed image. The cropped image is group 7 element 3 which in the raw image contains only 47×47 pixels whereas the reconstructed image contains 2 folds higher density. The pixel sizes can be apparently seen to have improved also. The contrast improvement has been demonstrated using line plots. The achieved resolution is 3.1 μm.

6.5. Proposed FP on biological samples

The idea of any imaging system is to offer capabilities to image various kinds of samples, especially there is high demand in imaging biological samples, because of the health imaging industry. To demonstrate use of proposed FP on biological samples, in the next part of this work, we have experimented with biological samples on a microscope glass slide. We have used infected red blood cells as a sample. Due to the limitations of the proposed system caused by the reduced spatial coherence, the resolution improvement has not been significant. This limitation has been discussed earlier for USAF target card results in Figure 6.6. As a result, the performance of proposed FP based compact imaging system on biological samples has not been crucial.

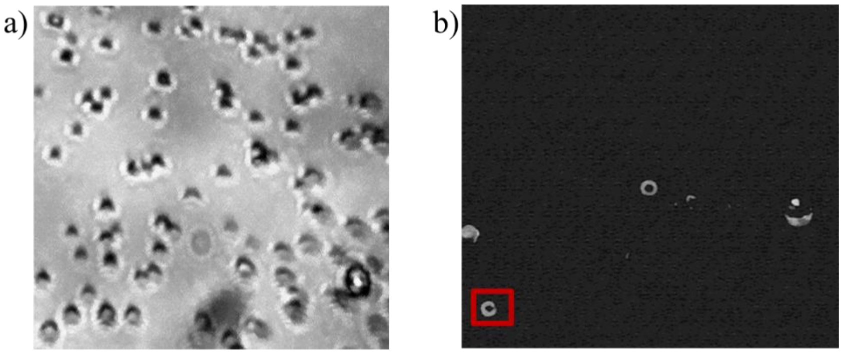

Figure 6:10: Infected red blood cells imaged using a single moldless lens-based imaging system as shown in Figure 6.5. a) Segment of raw image captured using center LED showing infected red blood cells. b) Reconstructed image using Fourier Ptychography in combination with pre-processing steps proposed in [190]. There is a higher amount of thresholding that caused loss of details in the reconstructed images. Also, the limitation in resolution improvement due to reduced spatial coherence restricted significant improvement in reconstruction.

Moreover, FP data acquisition process is a time-consuming process (it can take an hour for image acquisition), we assumed the sensor heats up as time progresses. This has been discussed in a recent work by Zhang *et al* where they have discussed how sensor dark current can impact performance of FP due to the accumulation of thermal noise.

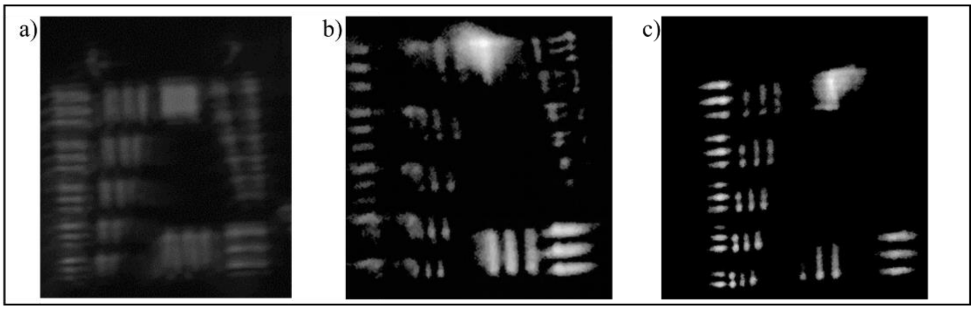

Figure 6:11: Demonstration of effectiveness of pre-processing as discussed in [190]. By acquiring multiple images of the sensor at different exposure over a certain period of time, and then subtracting the dark current data as a measure for background subtraction, the pre-processing has been achieved. a) Cropped raw image showing groups 6-7. b) FP reconstruction without using the dark current noise subtraction. c) FP reconstruction with the dark current based pre-processing steps. The performance of c) is better in terms of contrast and structural similarity.

They proposed pre-processing algorithm to be implemented prior to FP reconstruction [190]. Using their pre-processing algorithm in conjunction with proposed FP we have been able to acquire better reconstruction results for our data (both USAF and biological samples). The reconstruction results for biological samples have been shown in Figure 6.10, where red blood cell samples have been imaged using single moldless lens based imaging system. The reconstructed image demonstrates a circular donut shape that red blood cells typically have. The corresponding cell in the raw image is distorted, which has been successfully corrected by FP. We have used the pre-processing approach on dataset shown in Figure 6.9. The reconstruction results have shown improvement in contrast and structural similarity index.

6.6. Phase retrieval using proposed FP

Iterative phase retrieval algorithms are capable of retrieving phase information from intensity information only, where the iterative approaches work back and forth between spatial and Fourier domains.

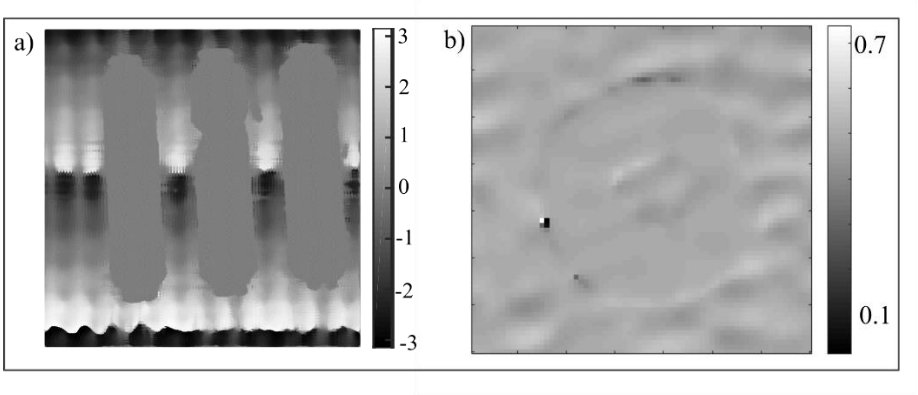

Figure 6:12: Phase retrieval using proposed compact imaging system and Fourier Ptychography. a) Wide FOV phase retrieved for the data acquired using an aspheric lens cascaded with objective 5x. There is noise in the phase due to the negative USAF target card generating black background (0 grey values in the matrix). b) Phase retrieved for a red blood cell. Data shown in Figure 6.10.

The proposed FP based optimization is also capable of retrieving phase information from the acquired intensity images. Intensity is typically the squared value of the amplitude of the wavefront. So, the phase information is not recorded by a simple imaging system.

After using the proposed FP optimization on different data, we were able to retrieve phase information as shown in Figure 6.12. Figure 6.12(a) shows retrieved phase for a ROI corresponding to element 3 of group 4, shown in Figure 6.9(a)-(b). The phase information contains noise due to the use of a negative USAF target card. Figure 6.12(b) shows the phase information retrieved from the infected red blood cell data shown in Figure 6.10.

6.7. Pupil retrieval using proposed FP

The use of computational aberration correction in the process of FP has improved the performance of the reconstruction results. In the proposed FP and previous works, the object spectrum and the pupil has been concurrently retrieved. Because FP works on a local area on the sample, the pupil wavefront can be retrieved across the sample. This has been demonstrated in Figure 6.13, for the dataset shown in Figure 6.8. Pupil retrieval for 5 different locations on the sample have been chosen and the retrieved wavefronts have been shown. The retrieved pupils vary significantly because of the varying aberrations offered by moldless lenses.

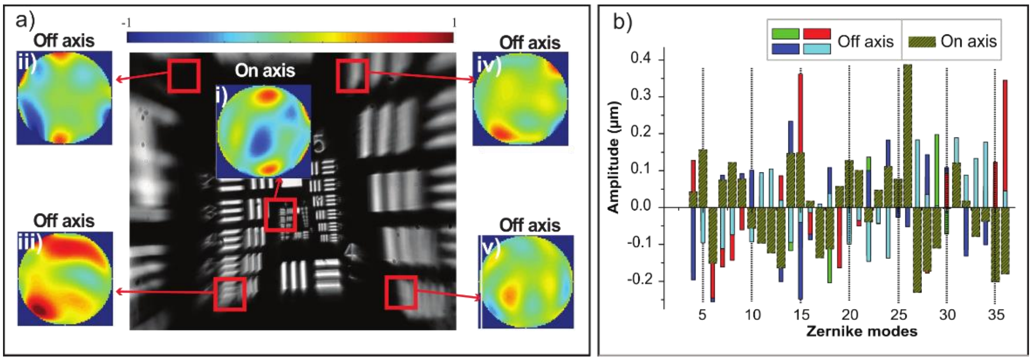

Figure 6:13: Pupil retrieval using FP on moldless lenses for dataset shown in Figure 6.8. a) Here, we have summarized the retrieved pupil on 5 different locations for the dataset shown in Figure 6.7. The off-axis aberrations appear to be higher than the on-axis aberration as expected. b) The Zernike decomposition of the pupil aberrations for modes up to 40.

We have observed pupil wavefronts for the moldless datasets as shown in Figure 6.9 and Figure 6.10, respectively. In Figure 6.13(a) we have demonstrated pupil aberrations retrieved from different regions across the sample, for the dataset acquired using single moldless lens. The aberrations have been decomposed into the Zernike polynomials for modes up to 40. We can observe the presence of higher-order aberrations in Figure 6.13(b).

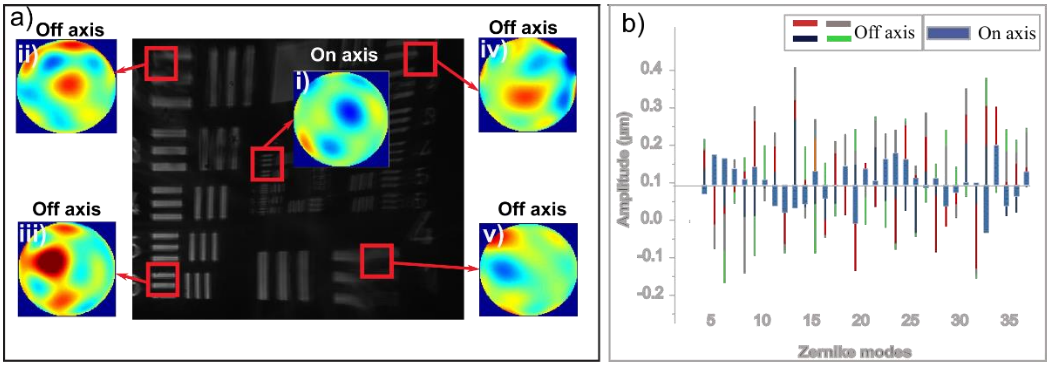

Figure 6:14: Retrieved pupil for dataset shown in Figure 6.9, compound imaging system. a) We have summarized the retrieved pupil on 5 different locations for the dataset shown in Figure 6.9. Like the Figure 6.11, the off-axis aberrations appear to be higher than the on-axis aberration as expected. b) The Zernike decomposition of the pupil aberrations for modes up to 40.

The aberrations observed across the sample for the compound moldless lens-based system can be seen in Figure 6.14. In this scenario also, we can observe the presence of higher-order aberrations in larger magnitude. This is expected due to the variability in the process of the moldless lens-making process.

The aberrations found for this system are higher compared to the single lens based system which we will further elaborate in Chapter 7.

6.8. Contributions

This work was done under the supervision of Dr. Woei Ming Lee throughout. All the data and analysis have been done by me.

6.9. Chapter Summary

In this chapter, we have demonstrated the performance of moldless lens-based imaging system in combination with Fourier Ptychography. FP has the capability to computationally optimize the object spectrum of the imaging systems through the use of iterative algorithms. While iteratively optimizing object spectrum in the Fourier domain, FP introduces a guess phase map, which computationally compensates for the aberrations. The limitations of FP on moldless lens-based imaging system have been discussed here. The demonstration of FP on an imaging system with large aberrations has been done first time during this work. Its observable that, even with the high amount of aberrations, FP is capable of offering, wide FOV, high resolution imaging for moldless lenses. This has been observed in more moldless lens-based imaging systems, which can be found in Appendix B.

CHAPTER 7
CONCLUSION

In the current world of rapid growth of engineering instruments, it is essential to look for alternative manufacturing and prototyping ideas. The needs for imaging device instrumentation are no exception in that regard. High resolution imaging needs have broad applications in research, health and education sectors. Our goal was to propose engineering ideas for developing high resolution imaging systems in low-resource environments. In the following subsections we will discuss the different shortcomings of the proposed processes and offer ideas how those shortcomings can be overcome.

7.1. Thesis summary

Decentralizing engineering of the complex scientific instruments at low-cost, is important to allow increase in accessibility of the devices. Combination of consumer mobile imaging systems and disposable lenses has steered in practical in-vivo imaging screening on mobile devices [5, 162, 191] for primary care and low resources settings. For optical imaging, the idea of compact imaging systems also started to incorporate computational techniques to offer high resolution imaging using simpler optical systems [31, 44, 54, 62, 63]. In this work, we successfully implemented the use of a passive droplet dispenser that provides a direct and low-cost alternative to fabricating moldless lenses at high throughput. Additionally, we have also demonstrated that there are more alternative approaches to generate moldless lenses. While there is certain amount of variability among the focal lengths of the lenses, the simplicity of the approach makes this a worthwhile approach for rapid production of high quality short focal length lenses for high resolution imaging. We have also showcased modular microscope designs based on Raspberry Pi system on a thimble imaging setup. It removes rigid design (fixed arrangement of camera and display) of existing consumer smartphone systems and offers much higher configurability and portability. The new design closely resembles a digital endoscope or inspection scopes albeit it uses the finger as an actuator to manipulate the camera.

The simplicity of fabrication of moldless lenses provides a low cost alternative to create high quality lenses [8], but this comes at the cost of variability over the optical performances. In the next part of the work, we demonstrated, for the first time, the power of FP imaging in retrieving and reversing aberrations in moldless lenses and thereby retrieving the full field of view (FOV) with imaging resolution, from 0.035 to 0.099, and SBP, from 5 megapixels to 15 megapixels [182]. Hence, this advantage provides a new avenue for moldless optics to increase the imaging space product bandwidth (SBP) which cannot be achieved through improvements in lens fabrication. This work shows that computational imaging can overcome large aberrations in moldless lenses without resorting to classical wavefront correction schemes. This work paves ways to development of numerous low cost high performance imaging systems using moldless lenses. From the results, we showed that FP imaging can be used on single or multi-lensed moldless lens-based systems with resolution improvement by approximately 3 folds, recovering almost all off-axis aberrations. A current drawback of the FP imaging is the lengthy time during acquisition but that could be solved by parallel processing *i.e.* increasing the number of microprocessors in the system. Due to high distortion and aberrations spanning across the curvature of the lenses the resolution improvement has been limited; this discrepancy could be addressed by employing phase diversity approaches and moldless lenses of larger apertures. Furthermore, we plan to use smaller LED areas to increase the spatial coherence of the system to improve the FP reconstruction performance on our imaging system.

Overall, this work encompasses manufacturing, optical instrumentation, and computational optimization in image processing to offer high resolution microscopes. This work offers ideas of various possibilities towards decentralized microscope systems which can be useful for various research areas.

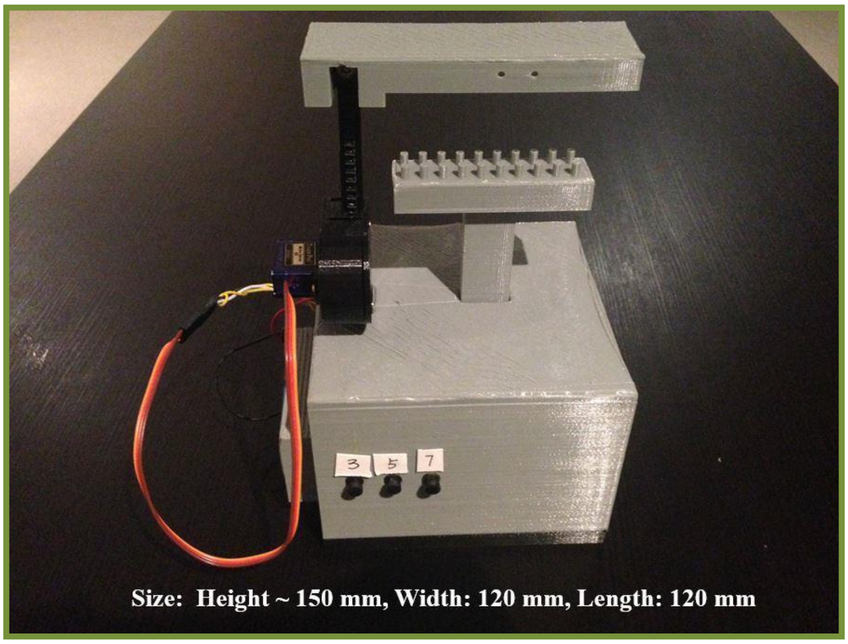

Figure 7:1: Portable lens-maker that can print a range of moldless lenses using *in-situ* heating element. This 3D printed prototype has been developed by Xu Tao, 4th year honours student.

7.2. Discussion on moldless lens manufacturing

The first building block of the research focused on ideas for manufacturing low-cost moldless optical lenses generated using liquid droplets where the convexity is achieved naturally. The benefit of this approach is that the lenses can be made abundantly and repeatedly without the need for complex laboratory/industry instruments. To achieve higher throughput, we proposed passive droplet dispenser. While the manufacturing process is efficient to provide a somewhat control over the range of focal lengths (~ 4 mm – 25 mm), along with magnifications, numerical aperture (~0.02 – 0.3), there is still significant amount of variability in the convexity achieved as the process of accumulation of the droplets is completely natural. Traditionally designers want more control over the process. This is one disadvantage of the proposed dispenser. The other lens-making process discussed in Chapter 3, is one of the quickest possible process to generate hundreds of moldless droplet lenses with varying magnifications and focal lengths. However, the process is crude and there is minimal control over the diameter and convexity. We have also developed a portable moldless lens-maker that can offer moldless lenses (variable base diameter of 2 mm – 6 mm) with different convexities by repeated deposition of PDMS. The portable lens-maker is 3D printed and can cure moldless lenses *in-situ*, by thermal curing with the use of a heating element (temperature up to 150 ºC). The portable lens-maker can be found in Figure 7.1 [152].

7.3. Discussion on decoupled imaging prototype

The moldless macro-lenses pave ways to engineer portable, compact imaging systems that can offer high resolution imaging. As an example of an on-field, decoupled imaging system, we proposed a thimble imaging system in the next step. The whole setup is wearable. However, it has been observed that the illumination is not sufficient as the working distance (from the lens to the sample) is typically small (5 mm -10 mm). This provides images with less brightness and contrast (Figure 4.13). This can be improved by offering a ring LED with multiplexing capabilities in place of the current neopixel LEDs. The other design we have proposed can be build using only open-source 3D printed parts. The prototype has been tested in a laboratory environment by far. We intend to move the prototype in education facilities like schools, to offer standalone upright microscopes at low-cost.

7.4. Discussion on moldless lens based Fourier Ptychographic Microscopy

However, the imaging performance of the moldless lenses exhibit high off-axis aberrations and distortions, where the area better contrast and less aberration is proportional to the focal length. That means lenses with longer focal lengths have less distortions and aberrations. There is still significant amount of distortions compared to commercial objective lenses (compound) or industry-polished singlet lenses. The origin of these aberrations can be credited to multiple variability factors in the manufacturing and imaging process, such as, i) the naturally occurring convexity of the shape, ii) the removal of the lens from the droplet-holder (breakage in the bottom of the lenses), iii) the optical alignment of the lenses and, iv) the presence of certain degree of aspheric profile in the curvature etc. So, to meet our end-goal to engineer high resolution imaging system, it was required to remove this distortions and aberrations from the moldless lens-based images. To achieve this, we resorted to computational approach that can be incorporated in the typical simple imaging system without, i) introducing high overhead cost, ii) the requirement of complex, laboratory-based optical equipment, and iii) altering the goal for compact high resolution imaging.

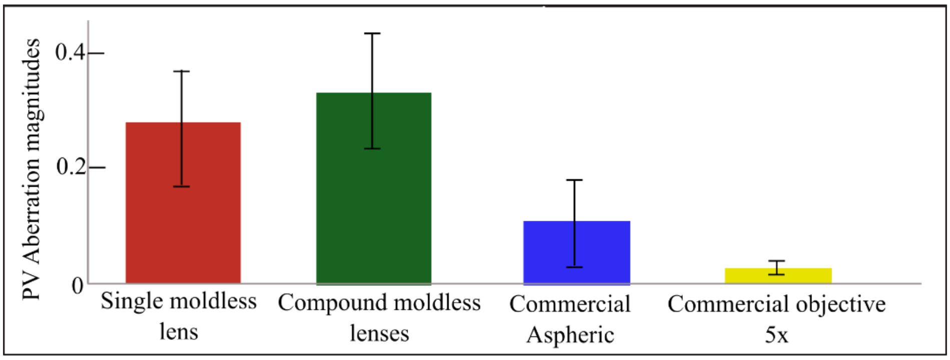

Figure 7:2: Peak-to-valley cumulative aberrations acquired from the proposed composed imaging system using various lenses. It is observable that the imaging system where a pair of moldless lenses was used for imaging (Figure 6.6) demonstrated higher magnitude of aberrations. Accordingly, the compound commercial objective 5x lens demonstrated the least aberrations.

Fourier Ptychography (FP), an emerging computational microscope technique, can offer digital wavefront correction that can remove aberrations and distortions as shown previously in different literature [11, 189]. However, the aberrations presented in their works were of low-order as it is expected that there was less variability in their commercial microscope systems. In our work, we observed performance of FP on various lenses to validate our judgment that moldless lenses demonstrate higher-order aberrations, in higher magnitude. This has been articulated in Figure 7.2.

As previously demonstrated that FP is capable of retrieving phase and offer images with improved SBP and resolution, the offered imaging prototype using FP can be a foundation for next-generation portable, compact (maximum 10 cm × 10 cm × 15 cm dimensions), low-cost imaging systems. This gives us idea for certain future works as discussed in the next section.

7.5. Future works

The idea of non-conventional optical techniques, which is a combination of moldless lenses and computational optimization, can offer various low-cost, high-resolution imaging prototypes. The change of the LED matrix in the current existing setup should be a very simple future work to observe the resolution improvement with improved spatial coherence.

The thimble imaging prototype can be improved to incorporate computational optimization on-field, so that the imaging quality of the system can be improved. In order to achieve that, we need to alter the computational algorithm, so that reflection-based imaging model can be optimized. Our current imaging model is suitable for transmission-based imaging system. FP has been reportedly used in reflection-based imaging setup, however the demonstration of the performance is yet to reach high quality performance and are still based on traditional microscopes [192]. We intend to develop reflection-based FP which can offer high resolution imaging for the thimble prototype.

This also brings us to our next imaging prototype that we can offer; a low-cost, rigid yet flexible, disposable endoscope. The idea emerged from the fact that typical endoscopes that can access any entering of the body, are designed to offer either rigidity or flexibility but not both. Alongside, endoscope reprocessing is important to ensure minimize pathogen transmission [193, 194]. So, our idea is to offer a high-resolution endoscope that can be built to offer both rigidity and flexibility in the same housing and is disposable. To achieve this, we propose to develop the optical system of the endoscope imaging using moldless lenses to offer low-cost prototype. We intend to use reflection-based FP on the endoscope imaging to improve imaging quality. Moreover, we intend to build the housing using PDMS which once cured is a soft plastic that can offer rigidity and flexibility at the same time.

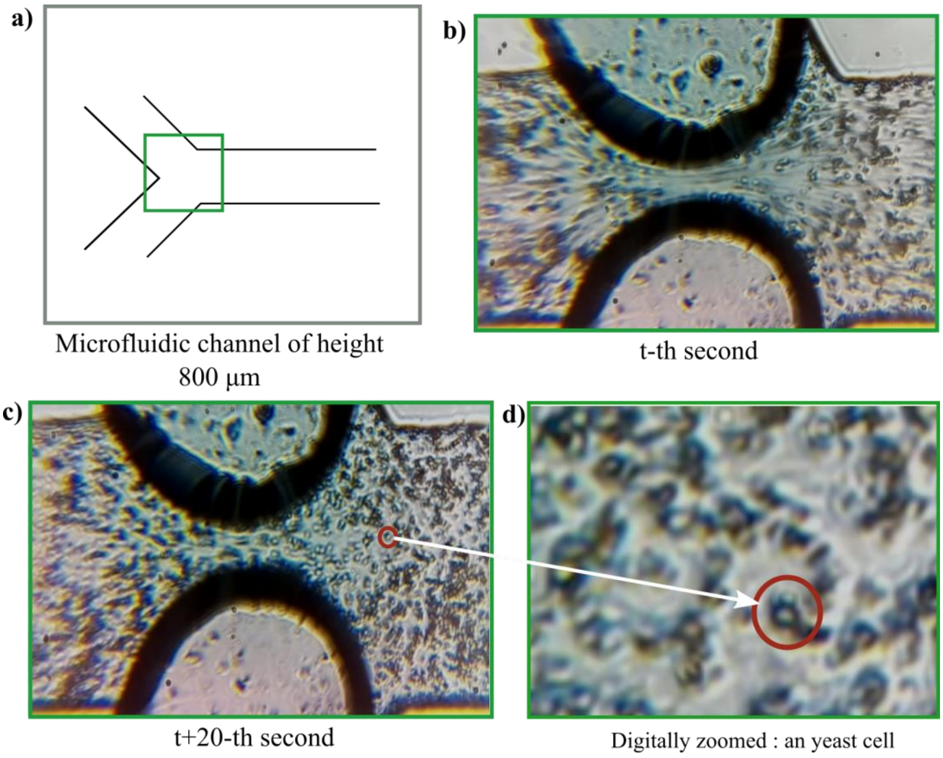

Microfluidic channel of height 800 μm

t-th second

t+20-th second

Digitally zoomed : an yeast cell

Figure 7:3: Microfluidic channel observation using a moldless lens and the proposed compact imaging system (preliminary data).Using raspberry pi camera video options, the observations were made. We present the data as screenshots here. a) Schematic of the channel that was observed under moldless lens. b) After some time the liquid was re-flown inside the channel. For this reason, the screenshot shows flow. c) After some time the flow settled, and we can see the yeast cells. d) Post-processing was done and digital zoom was applied to crop a region and observe yeast cells.

Another possible future project could be an extension of the current imaging system to a 2×2 matrix, that is, 4 compact imaging systems, to develop a single-sweep digital pathology scanner. The idea emerges from the capability of FP on the proposed compact imaging system, which can be extended to offer large FOV, high resolution imaging for pathological slides.

Deep learning algorithms based convolutional neural networks (CNN) have found application in image processing for image segmentation, resolution enhancement etc. [195]. We also propose to use CNN to offer high resolution compact imaging using moldless lenses for applications in disease detection.

Moldless lenses can also be used to develop microfluidic system based prototypes. This will offer microfluidic sample imaging at low-cost, portable manner. Some preliminary data using moldless lenses on microfluidic chip has been acquired during this research. Yeast cells of around 10 - 15 µm size were flown in fluid and observed using a single moldless lens-based imaging system. Figure 7.3 demonstrates the observations.

Overall this thesis provides ideas and demonstrates scientifically for low-cost high quality imaging systems that can be engineered at low-resource settings, with opportunities in medical imaging in future.

APPENDIX A

Optical and chemical properties of PDMS Sylgard 184 found from literature [86].

*This data has been observed in a recent literature by Zahid et al [196].

Property	Optical	Chemical
Optical transparency	Transparent in ultraviolet, visible and infrared wavelengths of electromagnetic spectrum (300 nm to 1200 nm).	
Optical transmittance*	Plain surface – 95% Rough surface – 92% Rough back surface – 80%	
Optical reflectance*	Plain surface – 7.5% - 6.5% Rough surface – 12% - 3% Back side of rough surface – 17% - 7%	
Refractive Index	At 589 nm: 1.4118 At 632.8 nm: 1.4225 At 1321 nm: 1.4028 At 1554 nm: 1.3997	
Viscosity		Base – 5.1 Pa-sec Mixed – 3.5 Pa-sec
Cure time at 25 ºC		48 hours
Heat Cure time at 100 ºC		35 minutes
Heat Cure time at 150 ºC		10 minutes
Specific gravity (cured)		1.03
Density		965 kg/m^3

APPENDIX B

The following table articulates the calculated values for RL and Roverlap. These parameters are indicators of the performance of FP on various imaging systems. The system requirements for FP to provide quality reconstruction result are guided by these parameters.

Lens NA (calculated)	**Magnification (System)**	**Wavelength (nm)**	**CMOS pixel size (µm)**	**Height between LED and sample (mm)**	**Spacing between LED (mm)**	**R_L**	**$R_{overlap}$**
0.12	1.76	632	1.4	80	4	2.4	0.73
0.1	3.47	632	1.4	80	4	2	0.68

REFERENCES

[1] S. A. Boppart and R. Richards-Kortum, "Point-of-care and point-of-procedure optical imaging technologies for primary care and global health," *Science Translational Medicine,* 10.1126/scitranslmed.3009725 vol. 6, no. 253, p. 253rv2, 2014.

[2] K. Veronese. (2011, 12 March). *Here's what it actually costs to run a university science lab*. Available: https://io9.gizmodo.com/5827381/heres-what-it-actually-costs-to-run-a-university-science-lab?IR=T

[3] J.-P. Gaudillière and I. Löwy, *The Invisible Industrialist Manufactures and the Production of Scientific Knowledge*. New York: Palgrave Macmillan 1998.

[4] A. Skandarajah, C. D. Reber, N. A. Switz, and D. A. Fletcher, "Quantitative Imaging with a Mobile Phone Microscope," *PLOS ONE,* vol. 9, no. 5, p. e96906, 2014.

[5] M. V. D'Ambrosio *et al.*, "Point-of-care quantification of blood-borne filarial parasites with a mobile phone microscope," *Science Translational Medicine,* 10.1126/scitranslmed.aaa3480 vol. 7, no. 286, p. 286re4, 2015.

[6] M. M. Tripathi, S. Egawa, A. G. Wirth, D. M. Tshikudi, E. M. Van Cott, and S. K. Nadkarni, "Clinical evaluation of whole blood prothrombin time (PT) and international normalized ratio (INR) using a Laser Speckle Rheology sensor," *Scientific Reports,* vol. 7, no. 1, p. 9169, 2017/08/23 2017.

[7] Q. Kong, R. M. Allen, and L. Schreier, "MyShake: Initial observations from a global smartphone seismic network," *Geophysical Research Letters,* vol. 43, no. 18, pp. 9588-9594, 2016.

[8] T. Kamal, R. Watkins, Z. Cen, J. Rubinstein, G. Kong, and W. M. Lee, "Design and fabrication of a passive droplet dispenser for portable high resolution imaging system," *Scientific Reports,* vol. 7, p. 41482, 2017.

[9] C. L. Ventola, "Medical Applications for 3D Printing: Current and Projected Uses," *Pharmacy and Therapeutics,* vol. 39, no. 10, pp. 704-711, 2014.

[10] C. Severance, "Eben Upton: Raspberry Pi," *Computer,* vol. 46, no. 10, pp. 14-16, 2013.

[11] G. Zheng, R. Horstmeyer, and C. Yang, "Wide-field, high-resolution Fourier ptychographic microscopy," *Nature Photonics,* Article vol. 7, p. 739, 07/28/online 2013.

[12] L. Tian, X. Li, K. Ramchandran, and L. Waller, "Multiplexed coded illumination for Fourier Ptychography with an LED array microscope," *Biomedical Optics Express,* vol. 5, no. 7, pp. 2376-2389, 2014/07/01 2014.

[13] J. A. Alberts B, Lewis J, et al. (2002, 23 November). *Looking at the Structure of Cells in the Microscope. (4th ed.)*. Available: https://www.ncbi.nlm.nih.gov/books/NBK26880/

[14] T. Wilson, "Confocal Microscopy," in *Microanalysis of Solids*, B. G. Yacobi, D. B. Holt, and L. L. Kazmerski, Eds. Boston, MA: Springer US, 1994, pp. 219-232.

[15] D. Huang *et al.*, "Optical coherence tomography," *Science,* 10.1126/science.1957169 vol. 254, no. 5035, p. 1178, 1991.

[16] J. Sharpe *et al.*, "Optical Projection Tomography as a Tool for 3D Microscopy and Gene Expression Studies," *Science,* 10.1126/science.1068206 vol. 296, no. 5567, p. 541, 2002.

[17] D. J. Stephens and V. J. Allan, "Light Microscopy Techniques for Live Cell Imaging," *Science,* 10.1126/science.1082160 vol. 300, no. 5616, p. 82, 2003.

[18] J. Huisken, J. Swoger, F. Del Bene, J. Wittbrodt, and E. H. K. Stelzer, "Optical Sectioning Deep Inside Live Embryos by Selective Plane Illumination Microscopy," *Science,* 10.1126/science.1100035 vol. 305, no. 5686, p. 1007, 2004.

[19] F. Helmchen and W. Denk, "Deep tissue two-photon microscopy," *Nature Methods,* Review Article vol. 2, p. 932, 11/18/online 2005.

[20] K. I. Willig, S. O. Rizzoli, V. Westphal, R. Jahn, and S. W. Hell, "STED microscopy reveals that synaptotagmin remains clustered after synaptic vesicle exocytosis," *Nature,* vol. 440, p. 935, 04/13/online 2006.

[21] M. Yamanaka, N. I. Smith, and K. Fujita, "Introduction to super-resolution microscopy," *Microscopy,* vol. 63, no. 3, pp. 177-192, 2014.

[22] R. Rottenfusser and E. E. W. a. M. W. Davidson. *Zeiss Microscopy Online Campus | Microscopy Basics | Illumination and the Optical Train (17 November ed.)*. Available: http://zeiss-campus.magnet.fsu.edu/print/basics/opticaltrain-print.html

[23] J. Strong, *Concepts of Classical Optics*. United States of America: W. H. Freeman Company, Inc. , 1958.

[24] W. Bishara *et al.*, "Holographic pixel super-resolution in portable lensless on-chip microscopy using a fiber-optic array," *Lab on a Chip,* 10.1039/C0LC00684J vol. 11, no. 7, pp. 1276-1279, 2011.

[25] (2018). *Motif Advanced Upright Microscope for Life Science and Laboratories, BA310E | LabFriend Australia | Laboratory Equipment and Lab Supplies*. Available: http://www.labfriend.com.au/advanced-upright-microscope-for-life-science-and-laboratories-ba310e

[26] (2018, 12 February). *500x HD Colour Digital Microscope with USB*. Available: https://www.dshop.com.au/buy/500x-hd-colour-digital-microscope-with-usb/U500X

[27] D. N. Breslauer, R. N. Maamari, N. A. Switz, W. A. Lam, and D. A. Fletcher, "Mobile Phone Based Clinical Microscopy for Global Health Applications," *PLOS ONE,* vol. 4, no. 7, p. e6320, 2009.

[28] (2018, 12 February). *World Microscopy Devices Market is Expected to Reach USD 2.58 Bi - Crossroads Today*. Available: http://www.crossroadstoday.com/story/37449473/world-microscopy-devices-market-is-expected-to-reach-usd-258-billion-from-usd-105-billion-from-2015-to-2022

[29] V. Subramanian and K. Ragunath, "Advanced Endoscopic Imaging: A Review of Commercially Available Technologies," *Clinical Gastroenterology and Hepatology,* vol. 12, no. 3, pp. 368-376.e1.

[30] C. Frantz, K. M. Stewart, and V. M. Weaver, "The extracellular matrix at a glance," *Journal of Cell Science,* vol. 123, no. 24, pp. 4195-4200, 12/01 2010.

[31] M. Sanz, J. Á. Picazo-Bueno, L. Granero, J. García, and V. Micó, "Compact, cost-effective and field-portable microscope prototype based on MISHELF microscopy," *Scientific Reports,* Article vol. 7, p. 43291, 02/24/online 2017.

[32] D. Jin *et al.*, "Compact Wireless Microscope for In-Situ Time Course Study of Large Scale Cell Dynamics within an Incubator," *Scientific Reports,* Article vol. 5, p. 18483, 12/18/online 2015.

[33] A. R. Miller *et al.*, "Portable, Battery-Operated, Low-Cost, Bright Field and Fluorescence Microscope," *PLOS ONE,* vol. 5, no. 8, p. e11890, 2010.

[34] H. M. Ozaktas, H. Urey, and A. W. Lohmann, "Scaling of diffractive and refractive lenses for optical computing and interconnections," *Applied Optics,* vol. 33, no. 17, pp. 3782-3789, 1994/06/10 1994.

[35] A. Greenbaum *et al.*, "Wide-field computational imaging of pathology slides using lens-free on-chip microscopy," *Science Translational Medicine,* 10.1126/scitranslmed.3009850 vol. 6, no. 267, p. 267ra175, 2014.

[36] H. Zhu, S. O. Isikman, O. Mudanyali, A. Greenbaum, and A. Ozcan, "Optical Imaging Techniques for Point-of-care Diagnostics," *Lab on a chip,* vol. 13, no. 1, pp. 51-67, 10/09 2013.

[37] M. Euan and O. Aydogan, "Unconventional methods of imaging: computational microscopy and compact implementations," *Reports on Progress in Physics,* vol. 79, no. 7, p. 076001, 2016.

[38] E. A. Graham, S. Henderson, and A. Schloss, "Using mobile phones to engage citizen scientists in research," *Eos, Transactions American Geophysical Union,* vol. 92, no. 38, pp. 313-315, 2011.

[39] A. Overeem, J. C. R. Robinson, H. Leijnse, G. J. Steeneveld, B. K. P. Horn, and R. Uijlenhoet, "Crowdsourcing urban air temperatures from smartphone battery temperatures," *Geophysical Research Letters,* vol. 40, no. 15, pp. 4081-4085, 2013.

[40] S. Price, P. Davies, W. Farr, C. Jewitt, G. Roussos, and G. Sin, "Fostering geospatial thinking in science education through a customisable smartphone application," *British Journal of Educational Technology,* vol. 45, no. 1, pp. 160-170, 2014.

[41] F. Kleber and R. Sablatnig, "A Portable High Resolution Imaging System for Digitizing Large-Surface Paintings," in *2008 Congress on Image and Signal Processing,* 2008, vol. 3, pp. 746-750.

[42] D. Jung *et al.*, "Smartphone-based multi-contrast microscope using color-multiplexed illumination," *Scientific Reports,* vol. 7, no. 1, p. 7564, 2017/08/08 2017.

[43] S. Kim *et al.*, "Smartphone-based multispectral imaging: system development and potential for mobile skin diagnosis," *Biomedical Optics Express,* vol. 7, no. 12, pp. 5294-5307, 11/28 09/01/received 10/27/revised 11/20/accepted 2016.

[44] A. C. Akcay, K. S. Lee, L. R. Furenlid, M. A. Costa, and J. P. Rolland, "Compact low-cost detection electronics for optical coherence imaging," *Optical engineering (Redondo Beach, Calif.),* vol. 45, no. 7, p. 070504, 07/05 2006.

[45] L. Tian, Z. Liu, L.-H. Yeh, M. Chen, J. Zhong, and L. Waller, "Computational illumination for high-speed in vitro Fourier ptychographic microscopy," *Optica,* vol. 2, no. 10, pp. 904-911, 2015/10/20 2015.

[46] A. Greenbaum, U. Sikora, and A. Ozcan, "Field-portable wide-field microscopy of dense samples using multi-height pixel super-resolution based lensfree imaging," *Lab on a Chip,* 10.1039/C2LC21072J vol. 12, no. 7, pp. 1242-1245, 2012.

[47] T. Kamal, J. Rubinstein, R. Watkins, Z. Cen, G. Kong, and W. M. Lee, "Thimble microscope system," in *SPIE BioPhotonics Australasia*, 2016, vol. 10013, p. 5: SPIE.

[48] A. Maia Chagas, L. L. Prieto-Godino, A. B. Arrenberg, and T. Baden, "The €100 lab: A 3D-printable open-source platform for fluorescence microscopy, optogenetics, and accurate temperature control during behaviour of zebrafish, Drosophila, and Caenorhabditis elegans," *PLOS Biology,* vol. 15, no. 7, p. e2002702, 2017.

[49] T. Suzuki, "Challenges of image-sensor development," in *2010 IEEE International Solid-State Circuits Conference - (ISSCC),* 2010, pp. 27-30.

[50] M. K. Kim, "Principles and techniques of digital holographic microscopy," 2010, vol. 1, p. 51: SPIE.

[51] (2017, 18 November 2017). *Miniature Optical Sensor Technology | Compact Imaging*. Available: https://compactimaging.com/

[52] E. Ozdalga, A. Ozdalga, and N. Ahuja, "The Smartphone in Medicine: A Review of Current and Potential Use Among Physicians and Students," *Journal of Medical Internet Research,* vol. 14, no. 5, p. e128, Sep-Oct 09/27 11/11/received 01/15/rev-request 02/06/revised 08/01/accepted 2012.

[53] M. Roy *et al.*, "Lens-free automated cell detection system for telemedicine application," in *2015 IEEE SENSORS*, 2015, pp. 1-3.

[54] A. Ozcan and E. McLeod, "Lensless Imaging and Sensing," *Annual Review of Biomedical Engineering,* vol. 18, no. 1, pp. 77-102, 2016/07/11 2016.

[55] L. M. Lee, X. Cui, and C. Yang, "The application of on-chip optofluidic microscopy for imaging Giardia lamblia trophozoites and cysts," *Biomedical microdevices,* vol. 11, no. 5, pp. 951-958, 04/14 2009.

[56] S. Seo, T.-W. Su, D. K. Tseng, A. Erlinger, and A. Ozcan, "Lensfree holographic imaging for on-chip cytometry and diagnostics," *Lab on a Chip,* 10.1039/B813943A vol. 9, no. 6, pp. 777-787, 2009.

[57] A. F. Coskun, T.-W. Su, and A. Ozcan, "Wide field-of-view lens-free fluorescent imaging on a chip," *Lab on a Chip,* 10.1039/B926561A vol. 10, no. 7, pp. 824-827, 2010.

[58] Z. F. Phillips *et al.*, "Multi-Contrast Imaging and Digital Refocusing on a Mobile Microscope with a Domed LED Array," *PLOS ONE,* vol. 10, no. 5, p. e0124938, 2015.

[59] Y. Sung, F. Campa, and W.-C. Shih, "Open-source do-it-yourself multi-color fluorescence smartphone microscopy," *Biomedical Optics Express,* vol. 8, no. 11, pp. 5075-5086, 2017/11/01 2017.

[60] B. Kim, Y. J. Lee, J. G. Park, D. Yoo, Y. K. Hahn, and S. Choi, "A portable somatic cell counter based on a multi-functional counting chamber and a miniaturized fluorescence microscope," *Talanta*, vol. 170, no. Supplement C, pp. 238-243, 2017/08/01/ 2017.

[61] X. Heng *et al.*, "Optofluidic microscopy-a method for implementing a high resolution optical microscope on a chip," *Lab on a Chip,* 10.1039/B604676B vol. 6, no. 10, pp. 1274-1276, 2006.

[62] S. Rawat, S. Komatsu, A. Markman, A. Anand, and B. Javidi, "Compact and field-portable 3D printed shearing digital holographic microscope for automated cell identification," *Applied Optics,* vol. 56, no. 9, pp. D127-D133, 2017/03/20 2017.

[63] A. Greenbaum *et al.*, "Imaging without lenses: achievements and remaining challenges of wide-field on-chip microscopy," *Nature methods,* vol. 9, no. 9, pp. 889-895, 08/30 2012.

[64] A. K. Mudraboyina, L. Blockstein, C. C. Luk, N. I. Syed, and O. Yadid-Pecht, "A Novel Lensless Miniature Contact Imaging System for Monitoring Calcium Changes in Live Neurons," *IEEE Photonics Journal,* vol. 6, no. 1, pp. 1-15, 2014.

[65] P. Basu, "Microscopes made from bamboo bring biology into focus," *Nature Medicine,* vol. 13, p. 1128, 10/01/online 2007.

[66] F. Zernike, "Phase contrast, a new method for the microscopic observation of transparent objects," *Physica,* vol. 9, no. 7, pp. 686-698, 1942/07/01/ 1942.

[67] J. Marrison, L. Räty, P. Marriott, and P. O'Toole, "Ptychography – a label free, high-contrast imaging technique for live cells using quantitative phase information," *Scientific Reports,* Article vol. 3, p. 2369, 08/06/online 2013.

[68] W. J. Glantschnig and S.-H. Chen, "Light scattering from water droplets in the geometrical optics approximation," *Applied Optics,* vol. 20, no. 14, pp. 2499-2509, 1981/07/15 1981.

[69] "Antony van leeuwenhoek and his "little animals."," *Annals of Internal Medicine,* vol. 56, no. 1, pp. 169-169, 1962.

[70] H. G. Pfaender, "The history of glass," in *Schott Guide to Glass*, H. G. Pfaender, Ed. Dordrecht: Springer Netherlands, 1996, pp. 1-15.

[71] M. J. Weber, "Optical Properties of Glasses," in *Materials Science and Technology*: Wiley-VCH Verlag GmbH & Co. KGaA, 2006.

[72] M. Khorasaninejad *et al.*, "Visible Wavelength Planar Metalenses Based on Titanium Dioxide," *IEEE Journal of Selected Topics in Quantum Electronics,* vol. 23, no. 3, pp. 43-58, 2017.

[73] R. Frerichs, "New Optical Glasses with Good Transparency in the Infrared*," *Journal of the Optical Society of America,* vol. 43, no. 12, pp. 1153-1157, 1953/12/01 1953.

[74] R. M. Waxler and G. W. Cleek, "The Effect of Temperature and Pressure on the Refractive Index of Some Oxide Glasses " *JOURNAL OF RESEARCH of the National Bureau of Standards - A. Physics and Chemistry* vol. 77A, no. 6, pp. 755-763, November - December 1973.

[75] M. Pfeffer, "Optomechanics of Plastic Optical Components," in *Handbook of Plastic Optics*: Wiley-VCH Verlag GmbH & Co. KGaA, 2010, pp. 7-34.

[76] R. Kingslake and R. Barry Johnson, "Chapter 1 - The Work of the Lens Designer," in *Lens Design Fundamentals (Second Edition)*Boston: Academic Press, 2010, pp. 1-23.

[77] H. G. Pfaender, "Glass, the material," in *Schott Guide to Glass*, H. G. Pfaender, Ed. Dordrecht: Springer Netherlands, 1996, pp. 16-34.

[78] J. M. Bennett and P. Z. Takacs, "Surface roughness and scattering: papers from the first topical meeting," *Applied Optics,* vol. 32, no. 19, pp. 3333-3334, 1993/07/01 1993.

[79] J. E. Harvey and A. K. Thompson, "Scattering effects from residual optical fabrication errors," in *International Conferences on Optical Fabrication and Testing and Applications of Optical Holography*, 1995, vol. 2576, p. 20: SPIE.

[80] H. K. Raut, V. A. Ganesh, A. S. Nair, and S. Ramakrishna, "Anti-reflective coatings: A critical, in-depth review," *Energy & Environmental Science,* 10.1039/C1EE01297E vol. 4, no. 10, pp. 3779-3804, 2011.

[81] (2002-2018, 17 November 2017). *TAMRON | Home*. Available: https://www.tamron.co.jp/en/monozukuri/blog01/page06.html

[82] M. Polyanskiy. (2018, 30 September). *RefractiveIndex.INFO-Refractive index database*. Available: https://refractiveindex.info/

[83] (2017, 12 November 2017). *Injection-molded Polymer Optics | Diverse Optics Inc. | Photonics Showcase | Jul 2017 | Photonics Showcase*. Available: https://www.photonics.com/Product.aspx?PRID=61663&PID=15&VID=147&IID=964

[84] P. Tolley. (2003, 11 November). *Polymer Optics Gain Respect*. Available: https://www.photonics.com/a17127/Polymer_Optics_Gain_Respect

[85] J. L. Wilbur, R. J. Jackman, G. M. Whitesides, E. L. Cheung, L. K. Lee, and M. G. Prentiss, "Elastomeric Optics," *Chemistry of Materials,* vol. 8, no. 7, pp. 1380-1385, 1996/01/01 1996.

[86] G. Lorenz and A. Kandelbauer, "14 - Silicones," in *Handbook of Thermoset Plastics (Third Edition)*Boston: William Andrew Publishing, 2014, pp. 555-575.

[87] I. D. Johnston, D. K. McCluskey, C. K. L. Tan, and M. C. Tracey, "Mechanical characterization of bulk Sylgard 184 for microfluidics and microengineering," *Journal of Micromechanics and Microengineering,* vol. 24, no. 3, p. 035017, 2014.

[88] R. Amarit *et al.*, "High-Quality Large-Magnification Polymer Lens from Needle Moving Technique and Thermal Assisted Moldless Fabrication Process," *PLoS ONE,* vol. 11, no. 1, p. e0146414, 2016.

[89] S. Damodara, D. George, and A. K. Sen, "Single step fabrication and characterization of PDMS micro lens and its use in optocapillary flow manipulation," *Sensors and Actuators B: Chemical,* vol. 227, no. Supplement C, pp. 383-392, 2016/05/01/ 2016.

[90] S. Ekgasit, N. Kaewmanee, P. Jangtawee, C. Thammacharoen, and M. Donphoongpri, "Elastomeric PDMS Planoconvex Lenses Fabricated by a Confined Sessile Drop Technique," *ACS Applied Materials & Interfaces,* vol. 8, no. 31, pp. 20474-20482, 2016/08/10 2016.

[91] W. M. Lee, A. Upadhya, P. J. Reece, and T. G. Phan, "Fabricating low cost and high performance elastomer lenses using hanging droplets," *Biomedical Optics Express,* vol. 5, no. 5, pp. 1626-1635, 2014.

[92] J. C. Lötters, W. Olthuis, P. H. Veltink, and P. Bergveld, "The mechanical properties of the rubber elastic polymer polydimethylsiloxane for sensor applications," *Journal of Micromechanics and Microengineering,* vol. 7, no. 3, p. 145, 1997.

[93] N. Bowden, W. T. S. Huck, K. E. Paul, and G. M. Whitesides, "The controlled formation of ordered, sinusoidal structures by plasma oxidation of an elastomeric polymer," *Applied Physics Letters,* vol. 75, no. 17, pp. 2557-2559, 1999/10/25 1999.

[94] M. J. Owen and P. J. Smith, "Plasma treatment of polydimethylsiloxane," *Journal of Adhesion Science and Technology,* vol. 8, no. 10, pp. 1063-1075, 1994/01/01 1994.

[95] D. Beysens, "The formation of dew," *Atmospheric Research,* vol. 39, no. 1, pp. 215-237, 1995/10/01/ 1995.

[96] L. Rayleigh, "On The Instability Of Jets," *Proceedings of the London Mathematical Society,* vol. s1-10, no. 1, pp. 4-13, 1878.

[97] D. Bonn, J. Eggers, J. Indekeu, J. Meunier, and E. Rolley, "Wetting and spreading," *Reviews of Modern Physics,* vol. 81, no. 2, pp. 739-805, 05/27/ 2009.

[98] "Weber Number," in *Encyclopedia of Microfluidics and Nanofluidics*, D. Li, Ed. Boston, MA: Springer US, 2008, pp. 2185-2185.

[99] N.-T. Nguyen, "Chapter 6 - Micromixers based on chaotic advection," in *Micromixers (Second Edition)*Oxford: William Andrew Publishing, 2012, pp. 195-238.

[100] Leonardo and E. McCurdy, *The notebooks of Leonardo da Vinci*. New York: Reynal & Hitchcock, 1938.

[101] E. Jens and V. Emmanuel, "Physics of liquid jets," *Reports on Progress in Physics,* vol. 71, no. 3, p. 036601, 2008.

[102] Z. Cai, W. Qiu, G. Shao, and W. Wang, "A new fabrication method for all-PDMS waveguides," *Sensors and Actuators A: Physical,* vol. 204, no. Supplement C, pp. 44-47, 2013/12/15/ 2013.

[103] H. Kazuo, H. Kotaro, and M. Ryutaro, "A polydimethylsiloxane (PDMS) deformable diffraction grating for monitoring of local pressure in microfluidic devices," *Journal of Micromechanics and Microengineering,* vol. 12, no. 1, p. 1, 2002.

[104] I. D. W. Samuel and G. A. Turnbull, "Polymer lasers: recent advances," *Materials Today,* vol. 7, no. 9, pp. 28-35, 2004/09/01/ 2004.

[105] L. Wang, X. Wang, W. Jiang, J. Choi, H. Bi, and R. Chen, "45° polymer-based total internal reflection coupling mirrors for fully embedded intraboard guided wave optical interconnects," *Applied Physics Letters,* vol. 87, no. 14, p. 141110, 2005/10/03 2005.

[106] T.-K. Shih, C.-F. Chen, J.-R. Ho, and F.-T. Chuang, "Fabrication of PDMS (polydimethylsiloxane) microlens and diffuser using replica molding," *Microelectronic Engineering,* vol. 83, no. 11, pp. 2499-2503, 2006/11/01/ 2006.

[107] A. Ashkin and J. M. Dziedzic, "Observation of Resonances in the Radiation Pressure on Dielectric Spheres," *Physical Review Letters,* vol. 38, no. 23, pp. 1351-1354, 06/06/ 1977.

[108] H. M. Tzeng, K. F. Wall, M. B. Long, and R. K. Chang, "Laser emission from individual droplets at wavelengths corresponding to morphology-dependent resonances," *Optics Letters,* vol. 9, no. 11, pp. 499-501, 1984/11/01 1984.

[109] M. Saito, H. Shimatani, and H. Naruhashi, "Tunable whispering gallery mode emission from a microdroplet in elastomer," *Optics Express,* vol. 16, no. 16, pp. 11915-11919, 2008/08/04 2008.

[110] M. Tanyeri, D. Dosev, and I. M. Kennedy, "Chemical and biological sensing through optical resonances in pendant droplets," in *Proceedings of SPIE - The International Society for Optical Engineering*, 2005, vol. 6008.

[111] S. Soria *et al.*, "Optical Microspherical Resonators for Biomedical Sensing," *Sensors (Basel, Switzerland),* vol. 11, no. 1, pp. 785-805, 01/12 12/08/received 12/28/revised 01/06/accepted 2011.

[112] W. Song, A. E. Vasdekis, and D. Psaltis, "Elastomer based tunable optofluidic devices," *Lab on a Chip,* 10.1039/C2LC40481H vol. 12, no. 19, pp. 3590-3597, 2012.

[113] G. Beadie *et al.*, "Tunable polymer lens," *Optics Express,* vol. 16, no. 16, pp. 11847-11857, 2008/08/04 2008.

[114] P. Liebetraut, S. Petsch, J. Liebeskind, and H. Zappe, "Elastomeric lenses with tunable astigmatism," *Light Sci Appl,* Original Article vol. 2, p. e98, 09/13/online 2013.

[115] P. Liebetraut, S. Petsch, W. Mönch, and H. Zappe, "Tunable solid-body elastomer lenses with electromagnetic actuation," *Applied Optics,* vol. 50, no. 19, pp. 3268-3274, 2011/07/01 2011.

[116] A. M. Juergens, "Intraocular lens," ed: Google Patents, 1986.

[117] Y. Xia, E. Kim, X.-M. Zhao, J. A. Rogers, M. Prentiss, and G. M. Whitesides, "Complex Optical Surfaces Formed by Replica Molding Against Elastomeric Masters," *Science,* vol. 273, no. 5273, pp. 347-349, 1996.

[118] J.-T. Mäkinen, "Cost Modeling of Injection-Molded Plastic Optics," in *Handbook of Plastic Optics*: Wiley-VCH Verlag GmbH & Co. KGaA, 2010, pp. 219-249.

[119] R. Wimberger-Friedl, "The assessment of orientation, stress and density distributions in injection-molded amorphous polymers by optical techniques," *Progress in Polymer Science,* vol. 20, no. 3, pp. 369-401, 1995/01/01/ 1995.

[120] D. K. Bandyopadhyay, "An Experimental Approach for Mould Preparation and Moulding Technique of Fresnel Lenses," *Journal of Scientific & Industrial Research* vol. 61, no. 10, pp. 786-791, 2002.

[121] D. P. Spector and J. M. Kingsbury, "Fabrication of thermoplastic optical components by injection/compression molding," ed: Google Patents, 1989.

[122] C.-Y. Chang, "Rapid fabrication of various molds for replication of polymer lens arrays," *Polymer Engineering & Science,* pp. n/a-n/a, 2017.

[123] L. Li and A. Y. Yi, "An affordable injection-molded precision hybrid glass–polymer achromatic lens," *The International Journal of Advanced Manufacturing Technology,* vol. 69, no. 5, pp. 1461-1467, 2013/11/01 2013.

[124] V. Kalima *et al.*, "Transparent thermoplastics: Replication of diffractive optical elements using micro-injection molding," *Optical Materials,* vol. 30, no. 2, pp. 285-291, 2007/10/01/ 2007.

[125] B. C. Gross, J. L. Erkal, S. Y. Lockwood, C. Chen, and D. M. Spence, "Evaluation of 3D Printing and Its Potential Impact on Biotechnology and the Chemical Sciences," *Analytical Chemistry,* vol. 86, no. 7, pp. 3240-3253, 2014/04/01 2014.

[126] Y. S. Zhang *et al.*, "3D Bioprinting for Tissue and Organ Fabrication," *Annals of Biomedical Engineering,* vol. 45, no. 1, pp. 148-163, 2017/01/01 2017.

[127] B. A. E. Lehner, D. T. Schmieden, and A. S. Meyer, "A Straightforward Approach for 3D Bacterial Printing," *ACS Synthetic Biology,* vol. 6, no. 7, pp. 1124-1130, 2017/07/21 2017.

[128] B. Berman, "3-D printing: The new industrial revolution," *Business Horizons,* vol. 55, no. 2, pp. 155-162, 2012/03/01/ 2012.

[129] S. F. Busch, M. Weidenbach, M. Fey, F. Schäfer, T. Probst, and M. Koch, "Optical Properties of 3D Printable Plastics in the THz Regime and their Application for 3D Printed THz Optics," *Journal of Infrared, Millimeter, and Terahertz Waves,* vol. 35, no. 12, pp. 993-997, 2014/12/01 2014.

[130] K. Willis, E. Brockmeyer, S. Hudson, and I. Poupyrev, "Printed optics: 3D printing of embedded optical elements for interactive devices," presented at the Proceedings of the 25th annual ACM symposium on User interface software and technology, Cambridge, Massachusetts, USA, 2012.

[131] E. Tekin, P. J. Smith, and U. S. Schubert, "Inkjet printing as a deposition and patterning tool for polymers and inorganic particles," *Soft Matter,* 10.1039/B711984D vol. 4, no. 4, pp. 703-713, 2008.

[132] X. Zhu, H. Chen, L. Zhu, H. Wang, and W. Zhang, "Fabrication of curved microlens array using a drop-on-demand droplet generator and polydimethylsiloxane replica mold," 2014, vol. 53, p. 9: SPIE.

[133] T. Xu, J. Jin, C. Gregory, J. J. Hickman, and T. Boland, "Inkjet printing of viable mammalian cells," *Biomaterials,* vol. 26, no. 1, pp. 93-99, 2005/01/01/ 2005.

[134] R. E. Saunders, J. E. Gough, and B. Derby, "Delivery of human fibroblast cells by piezoelectric drop-on-demand inkjet printing," *Biomaterials,* vol. 29, no. 2, pp. 193-203, 2008/01/01/ 2008.

[135] G. Perçin and B. T. Khuri-Yakub, "Piezoelectric droplet ejector for ink-jet printing of fluids and solid particles," *Review of Scientific Instruments,* vol. 74, no. 2, pp. 1120-1127, 2003/02/01 2003.

[136] X. Zhu, L. Zhu, H. Chen, M. Yang, and W. Zhang, "Fabrication of multi-scale micro-lens arrays on hydrophobic surfaces using a drop-on-demand droplet generator," *Optics & Laser Technology,* vol. 66, no. Supplement C, pp. 156-165, 2015/03/01/ 2015.

[137] D. T. James *et al.*, "Thin-Film Morphology of Inkjet-Printed Single-Droplet Organic Transistors Using Polarized Raman Spectroscopy: Effect of Blending TIPS-Pentacene with Insulating Polymer," *ACS Nano,* vol. 5, no. 12, pp. 9824-9835, 2011/12/27 2011.

[138] J. X. Zhou *et al.*, "Characterization of drop-on-demand microdroplet printing," *The International Journal of Advanced Manufacturing Technology,* vol. 48, no. 1, pp. 243-250, 2010/04/01 2010.

[139] A. Huebner, S. Sharma, M. Srisa-Art, F. Hollfelder, J. B. Edel, and A. J. deMello, "Microdroplets: A sea of applications?," *Lab on a Chip,* 10.1039/B806405A vol. 8, no. 8, pp. 1244-1254, 2008.

[140] K. Bernath, M. Hai, E. Mastrobattista, A. D. Griffiths, S. Magdassi, and D. S. Tawfik, "In vitro compartmentalization by double emulsions: sorting and gene enrichment by

fluorescence activated cell sorting," *Analytical Biochemistry,* vol. 325, no. 1, pp. 151-157, 2004/02/01/ 2004.

[141] P. Walstra, "Principles of emulsion formation," *Chemical Engineering Science,* vol. 48, no. 2, pp. 333-349, 1993/01/01/ 1993.

[142] C. N. Baroud, F. Gallaire, and R. Dangla, "Dynamics of microfluidic droplets," *Lab on a Chip,* 10.1039/C001191F vol. 10, no. 16, pp. 2032-2045, 2010.

[143] N. Lorber *et al.*, "Some recent advances in the design and the use of miniaturized droplet-based continuous process: Applications in chemistry and high-pressure microflows," *Lab on a Chip,* 10.1039/C0LC00058B vol. 11, no. 5, pp. 779-787, 2011.

[144] P. Zhu and L. Wang, "Passive and active droplet generation with microfluidics: a review," *Lab on a Chip,* 10.1039/C6LC01018K vol. 17, no. 1, pp. 34-75, 2017.

[145] R. E. Russo, R. Withnell, and G. M. Hieftje, "Simple and Inexpensive Design for an Isolated Droplet Generator Useful in Studies of Atomization in Flames," *Applied Spectroscopy,* vol. 35, no. 6, pp. 531-536, 1981/11/01 1981.

[146] J. Heinzl and W. Schullerus, "Droplet generator for generating micro-drops, specifically for an ink-jet printer," ed: Google Patents, 1998.

[147] J.-H. Choi, S.-K. Lee, J.-M. Lim, S.-M. Yang, and G.-R. Yi, "Designed pneumatic valve actuators for controlled droplet breakup and generation," *Lab on a Chip,* 10.1039/B915596A vol. 10, no. 4, pp. 456-461, 2010.

[148] Y. Zeng, M. Shin, and T. Wang, "Programmable active droplet generation enabled by integrated pneumatic micropumps," *Lab on a Chip,* 10.1039/C2LC40906B vol. 13, no. 2, pp. 267-273, 2013.

[149] B. Davis, *Agile Practices for Waterfall Projects: Shifting Processes for Competitive Advantage*. J. Ross Pub., 2012.

[150] W. van Hoeve, S. Gekle, J. H. Snoeijer, M. Versluis, M. P. Brenner, and D. Lohse, "Breakup of diminutive Rayleigh jets," *Physics of Fluids,* vol. 22, no. 12, p. 122003, 2010/12/01 2010.

[151] J. A. Lock, J. D. Walker, and J. H. Andrews, "Using refraction caustics to monitor evaporation of liquid drop lenses," *Applied Optics,* vol. 29, no. 31, pp. 4599-4607, 1990/11/01 1990.

[152] Z. Cen and W. M. Lee, "A method for fabricating lenses," Australia Patent AU2016903569, 2016.

[153] "The evolution of microscope design from its invention to the present days," *The American Journal of Surgical Pathology,* vol. 7, no. 1, 1983.

[154] L. Goldman, "A simple portable skin microscope for surface microscopy," *A.M.A. Archives of Dermatology,* vol. 78, no. 2, pp. 246-247, 1958.

[155] G. M. Fishbine and R. J. Withoff, "Handheld finger print scanner for imaging and capturing a photographic image," ed: Google Patents, 1994.

[156] S. Al-Janabi, A. Huisman, and P. J. Van Diest, "Digital pathology: current status and future perspectives," *Histopathology,* vol. 61, no. 1, pp. 1-9, 2012.

[157] F. R. Dee, "Virtual microscopy in pathology education," *Human Pathology,* vol. 40, no. 8, pp. 1112-1121, 2009/08/01/ 2009.

[158] V. Singh and A. K. Misra, "Detection of plant leaf diseases using image segmentation and soft computing techniques," *Information Processing in Agriculture,* vol. 4, no. 1, pp. 41-49, 2017/03/01/ 2017.

[159] K. R. Gavhale, U. Gawande, and K. O. Hajari, "Unhealthy region of citrus leaf detection using image processing techniques," in *International Conference for Convergence for Technology-2014*, 2014, pp. 1-6.

[160] J. L. Araus and J. E. Cairns, "Field high-throughput phenotyping: the new crop breeding frontier," *Trends in Plant Science,* vol. 19, no. 1, pp. 52-61, 2014/01/01/ 2014.

[161] I. Culjak, D. Abram, T. Pribanic, H. Dzapo, and M. Cifrek, "A brief introduction to OpenCV," in *2012 Proceedings of the 35th International Convention MIPRO*, 2012, pp. 1725-1730.

[162] J. S. Cybulski, J. Clements, and M. Prakash, "Foldscope: Origami-Based Paper Microscope," *PLOS ONE,* vol. 9, no. 6, p. e98781, 2014.

[163] J. W. Goodman, *Introduction to Fourier Optics*, Third ed. Roberts & Company Publishers, 2005.

[164] R. W. Gerchberg and W. O. Saxton, "A practical algorithm for the determination of the phase from image and diffraction plane pictures," *Optik,* vol. 35, no. 2, pp. 237-246, 1972.

[165] R. P. Porter and A. J. Devaney, "Holography and the inverse source problem," *Journal of the Optical Society of America,* vol. 72, no. 3, pp. 327-330, 1982/03/01 1982.

[166] T. Colomb *et al.*, "Automatic procedure for aberration compensation in digital holographic microscopy and applications to specimen shape compensation," *Applied Optics,* vol. 45, no. 5, pp. 851-863, 2006/02/10 2006.

[167] R. Horstmeyer, "Computational Microscopy: turning megapxels into gigapixels," Doctorate of Philosophy, Californina Institute of Technology, Pasadena, Californina, 2016.

[168] A. Moreira, P. Prats-Iraola, M. Younis, G. Krieger, I. Hajnsek, and K. P. Papathanassiou, "A tutorial on synthetic aperture radar," *IEEE Geoscience and Remote Sensing Magazine,* vol. 1, no. 1, pp. 6-43, 2013.

[169] K. von Bieren, "Lens Design for Optical Fourier Transform Systems," *Applied Optics,* vol. 10, no. 12, pp. 2739-2742, 1971/12/01 1971.

[170] (2014, April 24, 2015). *Grasycale*. Available: http://www.aforgenet.com/framework/docs/html/img/imaging/grayscale.jpg

[171] W. Luo, A. Greenbaum, Y. Zhang, and A. Ozcan, "Synthetic aperture-based on-chip microscopy (accepted article preview)," *Light: Science & Applications,* p. 26, 2014.

[172] G. Zheng, R. Horstmeyer, and C. Yang, "Wide-field, high-resolution Fourier ptychographic microscopy," *Nature Photonics,* vol. 7, p. 7, September 2013 2013.

[173] G. Zheng, X. Ou, and C. Yang, "Gigapixel microscopy using a flatbed scanner," *Biomed. Opt. Express,* vol. 5, no. 1, p. 8, 2014.

[174] L. Tian and L. Waller, "3D intensity and phase imaging from light field measurements in an LED array microscope," *Optica,* vol. 2, no. 2, pp. 104-111, 2015/02/20 2015.

[175] B. M. Hennelly and J. T. Sheridan, "Image encryption and the fractional Fourier transform," *Optik - International Journal for Light and Electron Optics,* vol. 114, no. 6, pp. 251-265, 2003/01/01/ 2003.

[176] F. Zernike, "How I Discovered Phase Contrast," *Science,* 10.1126/science.121.3141.345 vol. 121, no. 3141, p. 345, 1955.

[177] D. Gabor, "The Principle of Wavefront Reconstruction, 1948," in *Optical and Acoustical Holography,* Boston, MA, 1972, pp. 9-14: Springer US.

[178] J. R. Fienup, "Phase retrieval algorithms: a comparison," *Applied Optics,* vol. 21, no. 15, pp. 2758-2769, 1982/08/01 1982.

[179] L.-H. Yeh *et al.,* "Experimental robustness of Fourier ptychography phase retrieval algorithms," *Optics Express,* vol. 23, no. 26, pp. 33214-33240, 2015/12/28 2015.

[180] L. Waller, G. Situ, and J. W. Fleischer, "Phase-space measurement and coherence synthesis of optical beams," *Nature Photonics,* Article vol. 6, p. 474, 06/24/online 2012.

[181] M. Levoy, Z. Zhang, and I. McDowall, "Recording and controlling the 4D light field in a microscope using microlens arrays," *Journal of Microscopy,* vol. 235, no. 2, pp. 144-162, 2009.

[182] T. Kamal, L. Yang, and W. M. Lee, "In situ retrieval and correction of aberrations in moldless lenses using Fourier ptychography," *Optics Express,* vol. 26, no. 3, pp. 2708-2719, 2018/02/05 2018.

[183] G. Chavent and K. Kunisch, "Convergence of Tikhonov regularization for constrained ill-posed inverse problems," *Inverse Problems,* vol. 10, no. 1, p. 63, 1994.

[184] R. W. Gerchberg and W. O. Saxton, "Phase determination from image, and diffraction plane pictures," *Optik,* vol. 34, pp. 237-246, 1972.

[185] J. R. Fienup, "Reconstruction of an object from the modulus of its Fourier transform," *Optics Letters,* vol. 3, no. 1, pp. 27-29, 1978/07/01 1978.

[186] J. Sun, Q. Chen, Y. Zhang, and C. Zuo, "Sampling criteria for Fourier ptychographic microscopy in object space and frequency space," *Optics Express,* vol. 24, no. 14, pp. 15765-15781, 2016/07/11 2016.

[187] S. Dong, Z. Bian, R. Shiradkar, and G. Zheng, "Sparsely sampled Fourier ptychography," *Optics Express,* vol. 22, no. 5, pp. 5455-5464, 2014/03/10 2014.

[188] J. Sun, C. Zuo, L. Zhang, and Q. Chen, "Resolution-enhanced Fourier ptychographic microscopy based on high-numerical-aperture illuminations," *Scientific Reports,* vol. 7, no. 1, p. 1187, 2017/04/26 2017.

[189] X. Ou, G. Zheng, and C. Yang, "Embedded pupil function recovery for Fourier ptychographic microscopy," *Optics Express,* vol. 22, no. 5, pp. 4960-4972, 2014/03/10 2014.

[190] Y. Zhang, A. Pan, M. Lei, and B. Yao, "Data preprocessing methods for robust Fourier ptychographic microscopy," 2017, vol. 56, p. 9: SPIE.

[191] Y.-L. Sung, J. Jeang, C.-H. Lee, and W.-C. Shih, "Fabricating optical lenses by inkjet printing and heat-assisted in situ curing of polydimethylsiloxane for smartphone microscopy," *Journal of Biomedical Optics*, vol. 20, no. 4, pp. 047005-047005, 2015.

[192] S. Pacheco, B. Salahieh, T. Milster, J. J. Rodriguez, and R. Liang, "Transfer function analysis in epi-illumination Fourier ptychography," *Optics Letters*, vol. 40, no. 22, pp. 5343-5346, 2015/11/15 2015.

[193] K. H. Hong and Y. J. Lim, "Recent Update of Gastrointestinal Endoscope Reprocessing," *Clinical Endoscopy*, vol. 46, no. 3, pp. 267-273, 05/31 03/24/received 03/26/revised 03/26/accepted 2013.

[194] W. A. Rutala and D. J. Weber, "Disinfection of Endoscopes: Review of New Chemical Sterilants Used for High-Level Disinfection," *Infection Control & Hospital Epidemiology*, vol. 20, no. 1, pp. 69-76, 2015.

[195] O. Z. Kraus, J. L. Ba, and B. J. Frey, "Classifying and segmenting microscopy images with deep multiple instance learning," *Bioinformatics*, vol. 32, no. 12, pp. i52-i59, 2016.

[196] A. Zahid, B. Dai, R. Hong, and D. Zhang, "Optical properties study of silicone polymer PDMS substrate surfaces modified by plasma treatment," *Materials Research Express*, vol. 4, no. 10, p. 105301, 2017.

Vita

1982 - Born in Dhaka, Bangladesh.

1987 - 1990 - Attended Primary School in Dhaka, Bangladesh.

1991 - 1997 - Attended Shaheed Anwar Girls' College, Dhaka, Bangladesh

1998 - 1999 - Attended Holy Cross College, Dhaka Bangladesh.

2000 - 2004 - Undergraduate education in East West University, Dhaka, Bangladesh.

2005 - 2006 - Postgraduate education (Masters) in East West University, Dhaka, Bangladesh.

2006 - 2009 - Worked as a Lecturer in East West University, Dhaka, Bangladesh.

2009 - 2013 - Worked as a Senior Lecturer in East West University, Dhaka, Bangladesh.

2013 - - Migrated in Australia as a skilled permanent resident.

2014 - 2018 - Postgraduate (PhD) studies in Australian National University.

Updated profile can be found in

https://www.linkedin.com/in/tahseenkamal/